Implementation of the Ring of Fire system for on-site car aerodynamics

Guus Bloem

Delft University of Technology

Implementation of the Ring of Fire system for on-site car aerodynamics

by

Guus Bloem

in partial fulfillment of the requirements for the degree of

Master of science
in Aerospace engineering
Aerodynamics profile

at the Delft University of Technology,
to be defended publicly on Friday March 18, 2022 at 13:00.

Student number:	4554124	
Project Duration:	May, 2021 - March, 2022	
Supervisor:	Dr. A. Sciacchitano	
Supervisor:	Ir. A.M.C.M.G. Spoelstra	
Thesis committee:	Dr. ir. B.W. van Oudheusden	TU Delft, chairman
	Ir. Daniele Ragni	TU Delft, external member
	Dr. T. Gericke	Volkswagen, external supervisor

TU Delft

Preface

This thesis project is the penultimate step in the completion of the Aerodynamics master program at the faculty of aerospace engineering of the Delft University of Technology. Unfortunately, due to the widespread Covid pandemic, the internship will shortly follow after the completion of this thesis work, and thereby conclude the Master program.

In May 2021, Andrea Sciacchitano offered me the opportunity to continue the research towards the Ring of Fire and implement the system for the automotive industry, in collaboration with Volkswagen. I am very grateful for his continuous guidance and sharing his knowledge with me whenever I was in doubt or needed feedback. Also, I am very grateful to Alexander Spoelstra, who has provided me with his knowledge and expertise on the Ring of Fire during the first months of my thesis work.

Furthermore, I would like to thank Volkswagen for allowing me to participate in this project, inviting me to attend and help during the measurements at the proving ground in Wolfsburg, Germany. Specifically, I would like to thank Timo, Steffen and Malte, for their hospitality and making me feel at home. Also, I am thankful for all the help and feedback that was provided during the weekly meetings.

I would like to thank Ming and Yuga for giving me the opportunity to help them during their stereoscopic particle image velocimetry campaign in the open jet facility. They have shared their knowledge with me which shaped the foundation of my work.

Lastly, I am deeply grateful for the continuous support of my parents and brothers, who have always supported me through my studies here in Delft. Most of all, I am deeply thankful to my girlfriend, Julia, who always stood by my side during the past years.

Guus Bloem
Delft, March 2022

Abstract

Aerodynamic research in the automotive industry is an essential part of the reduction in resistance during driving, as it leads to an increased fuel efficiency and higher top speed. State-of-the-art aerodynamic research is conducted in wind tunnels, through numerical simulations (Computational Fluid Dynamics) and on-site coast down techniques. In recent year, a novel quantitative flow measurement technique for full-scale, on-site transiting objects has emerged: the Ring of Fire. This system is a non-intrusive, large-scale, stereoscopic particle image velocimetry measurement technique, which provides insight in the on-site flow topology around transiting objects and simultaneously determine their drag.

In this project, the Ring of Fire measurement system is implemented for the automotive industry in collaboration with Volkswagen. The Volkswagen Tiguan and Up are tested, where for the Tiguan a configuration with the radiator front open and with the radiator front closed are tested at a speed of 120 km/h. The objective of this research is to assess the applicability and feasibility of the Ring of Fire system for full-scale cars, comparing the flow visualisation in the wake of a car between different models and configurations, and additionally determining the drag and its uncertainty through the control volume approach.

A 3x3 meter field of view is used to obtained flow fields up to 5 meters in the wake. Up to 1 meter in the near wake the flow shows a clear upwash due to a vortex pair for both cars. After 1 meter, the wake of the Up transitions into a downwash, lowering the overall wake contour and causing a lateral expansion. In contrast, the wake of the Tiguan shows four vortices, of which the upper pair consists of two strong vortices maintaining upwash up to the far wake. A 'mushroom' kind of shape is the consequence, which is in accordance with the typical wake structures found in literature for estate cars. The Up however, shows a wake structure comparable to a notchback type car.

The control volume approach shows that the drag up to 2 meter is highly underestimated, which can be attributed to the incorrect reconstruction of the near wake pressure using the 2D Poisson equation. After 3 meter, the wake starts to diffuse in small scale structures which cannot be resolved by the window sizes. Therefore, the drag followed from the measurements between 2 and 3 meter, resulting in a mean value comparable to those found in wind tunnel tests and with an uncertainty of the mean at a 95% confidence level below 3%.

The Ring of Fire system setup in this project is capable of showing the differences between the Up and Tiguan, in terms of flow topology as well as drag values. However, a statistical distinction between the two Tiguan configurations was not established, likely due to the limited number of runs that were of sufficient quality for the Tiguan open configuration. Nonetheless, this first research towards the implementation of the Ring of Fire system for the automotive industry showed that its a promising technique, capable of defining on-site aerodynamic characteristics of cars and potentially serve as a validation tool for numerical simulations. Moreover, future research could investigate its applicability to accelerating, drafting or cornering cars, which cannot be investigated using the state-of-the-art techniques.

Contents

Nomenclature

Abbreviations

Abbreviation	Definition
2D2C	Two-dimensional two-components
2D3C	Two-dimensional three-components
BFS	Bubble Fluid Solution
CFD	Computational Fluid Dynamics
CI	Confidence Interval
CMOS	Complementary Metal-Oxide Semiconductor
CV	Control volume
CS	Control surface
DES	Detached Eddy Simulation
DSR	Dynamic Spatial Range
DVR	Dynamic Velocity Range
FOV	Field Of View
FSU	Fluid Supply Unit
HFSB	Helium Filled Soap Bubbles
LES	Large Eddy Simulation
Nd:Yag	Neodymiumdoped Yttrium Aluminium Garnet
PIV	Particle Image Velocimetry
PTU	Programmable timing unit
PPE	Pressure Poisson equation
RANS	Reynolds Averaged Navier Stokes
Re	Reynolds number
RMS	Root mean square
RoF	Ring of Fire
SAS	Scale Adaptive Simulation
SST	Shear Stress Transport
SNR	Signal to Noise Ratio

Symbols

Symbol	Definition
A	Frontal area
Cd	Drag coefficient
CdA	Drag area coefficient
C_p	Pressure coefficient
d_p	Tracer particle diameter
d_τ	Image particle diameter
d_diff	Diffraction diameter
d_geom	Geometrical diameter

Symbol	Definition
d_i	Distance sensor to lens
d_o	Distance object to lens
$D(t)$	Aerodynamic drag force
f	Frequency
f	F-stop
k	Coverage factor
L	Filter length
M	Magnification factor
n	Normal vector
V	Velocity
p_∞	Environmental pressure
S_{inlet}	Upstream surface plane
S_{outlet}	Downstream surface plane
S_{ij}	Q-criterion symmetric part
u_{inlet}	Streamwise velocity at inlet plane
u_{outlet}	Streamwise velocity at outlet plane
u_{car}	Velocity of the car
u	Lateral velocity component
v	Vertical velocity component
w	Stream wise velocity component
x	Lateral coordinate
y	Vertical coordinate
z	Stream wise coordinate
α	Angle between cameras and z-axis in XZ-plane
β	Angle between cameras and z-axis in YZ-plane
δz	Depth of focus
Δt	Pulse separation
∂	Partial derivative
θ	Angle between object and lens plane
λ	Laser light wavelength
λ_2	Vorticity criterion
Λ	Cut-off velocity
μ	Dynamic viscosity
ν	Kinematic viscosity of air
∇	Vector differential operator
ρ	Air density
ρ_p	Tracer particle density
ω	Vorticity
ω_x^*	Streamwise non-dimensional vorticity
Ω_{ij}	Q-criterion asymmetric part
σ	Standard deviation
σ_w^*	Streamwise non-dimensional turbulence
τ_p	Particle response time
τ_f	Characteristic time of the flow
$\bar{\tau}$	Stress tensor
ϕ	Angle between lens and image plane

List of Figures

List of Tables

Chapter 1

Introduction

Since the invention of cars back in 1885 by Benz, cars have become an increasingly popular way of transport for people all over the world. Cars make it easy to travel from one place to the other and have allowed people to work further away from their home. However, especially over the past decades, the rising environmental pollution due to green house gasses that these cars emit ask for a more sustainable and efficient energy consumption. This can be done by either reducing the energy consumption directly with increased power efficiency or by improving the drag of cars, indirectly leading to a lower energy consumption per driven kilometre. Above a speed of approximately 40 km/h the aerodynamic drag becomes the dominant drag force, even increasing up to 90% of the total drag force for speeds around 100 km/h. Therefore, the optimisation of the aerodynamic design of cars is of utmost importance for the reduction of the overall energy consumption of cars.

Nowadays, aerodynamic research is divided over several fields, where wind tunnel tests and CFD (Computational Fluid Dynamics) simulations are the most common. Also, on-road drag measurements such as coast-down technique are conducted. These measurement techniques all have there downsides. Wind tunnel tests are usually performed under ”perfect” conditions (very low turbulence, constant temperature and humidity, etc) and use scaled models, which leads to different flow behaviour due to the different Reynolds number compared to the real situation. Besides, wind tunnels are expensive to build and run. Nonetheless, using different techniques such as force balances, pressure sensors and particle image velocimetry, aerodynamic forces and flow fields can be represented rather accurately. CFD simulations on the other hand are capable of giving an accurate representation of the flow and can be used almost immediately, it is much easier to set-up and the costs are very low compared to wind tunnel testing. However, it remains an approximation of reality, where numerical calculations are involved and there are always assumptions that have to be taken into account. Lastly, coast-down measurements are performed outdoor on real sized cars or trucks, where the drag force can be accurately computed. However, no information is given where this drag force originates from, since this technique does not provide any insight in the flow field around the test object. Therefore, a need for a measurement system capable of measuring the flow field and aerodynamic forces of a car in their operating environment is sought for, and this is where the Ring of Fire can become the next large measurement system to be used for passenger cars, as a complementary tool to the previously described systems.

The Ring of Fire is a large-scale, quantitative flow measurement technique which is essentially large-scale stereoscopic particle image velocimetry (PIV) brought outside the wind tunnel and implemented on-site. This recently developed technique has been implemented thrice for research in the aerodynamics of individual and drafting cyclists, leading to promising results. Also, ice-skaters have been aerodynamically researched using this technique. The novelty of this measurement system lies in the on-site visualisation of the flow around the test object, which can be correlated to the aerodynamic forces (mainly the aerodynamic drag), aiding in providing information for the optimisation of the aerodynamic design of these test objects. This technique is of interest for unsteady movements, such as pedalling cyclists or moving ice-skaters, since these movements cannot (yet) be investigated and analysed in wind tunnels and numerical simulations. For cars, if the system is deemed feasible, the aerodynamics of cornering and drafting cars can be of large interest, since this is also yet to be implemented in wind tunnels and where especially the cornering aerodynamics will most likely not be feasible to test.

In this Thesis project, the Ring of Fire has been implemented for the Volkswagen Up and Tiguan on the Volkswagen site in Wolfsburg, Germany. The aim of the study is to assess the feasibility of this measurement system for passenger cars, by analysing the flow field, aerodynamic drag and correlation between the two for the Up and Tiguan. The differences between these cars are underlined and an attempt is made to correlate the flow topology to the respective drag coefficient.

This report is outlined as follows. In Chapter 2, the background literature in state-of-the-art car aerodynamics is provided and discussed as a foundation for this report. In Chapter 3, the theory behind large-scale, stereoscopic particle image velocimetry and the conservation of momentum in a control volume approach are discussed. Previous Ring of Fire experiments are summarised as well in this Chapter. Next, the experimental set-up and methodology are presented in Chapter 4 and Chapter 5 describes the analysis of the acquired data and the reduction techniques that have been used. In Chapter 6, the results are provided and a discussion follows regarding the different flow topology and drag values of the cars. A final conclusion is drawn in Chapter 7, as well as recommendations and limitations for future research with the Ring of Fire for passenger cars.

Chapter 2

Literature background on passenger car aerodynamics

The literature background on passenger car aerodynamics is laid out in this Chapter. Three commonly used techniques are discussed: wind tunnel studies, numerical studies and on-road measurements. Firstly, wind tunnel studies are discussed for scaled models in Section 2.1. Next, numerical studies are reviewed in Section 2.2. In Section 2.3, studies consisting of both wind tunnel measurements and numerical simulations are discussed. Lastly, on-road measurements are considered in Section 2.4. The thesis objective and relevance are provided in Section 2.5.

Contents

2.1 Wind tunnel studies

The first studies in the aerodynamics of cars were done through wind tunnel measurements. Especially in the early stages, pressure probes were used which measure the flow velocity and thereby determine the pressure. Also, laser doppler anemometry is a common measurement technique employed in wind tunnels to determine the flow topology around objects. More recently, particle image velocimetry (PIV) has become a frequently used measurement technique, correlating the flow topology with the aerodynamic forces.

2.1.1 The Ahmed body

One of the first attempts in the correlation of visualisation of the flow behind automobile shapes and its aerodynamic drag was done by Ahmed, 1981. In this research, the aim was to conduct a near wake analysis of a car's rear end at several locations behind the car. Pressure, velocity and force measurements were conducted and compared to the visualisation of the flow. The time averaged wake structure of 3 characteristic vehicle shapes was established: estate, fastback and notchback. These typical automobile shapes are presented in Figure 2.1a.

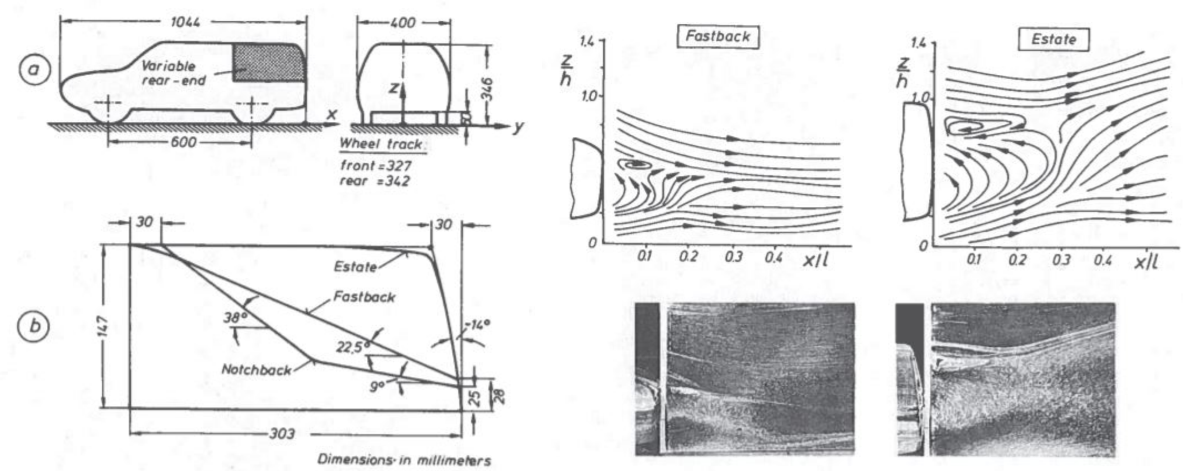

(a) Typical automobile shapes

(b) Streamline pattern

Figure 2.1: Typical automobile shapes and the streamline pattern of the fastback and estate configuration

The model itself was a quarter scale model, being 1044 mm long and having a length:width:height ratio of 3.02:1.16:1. The rear end was interchangeable, such that all three configurations could be set up with the same model. For the pressure measurements, a nine-hole conical-tip yaw meter probe was used whereas six component force measurements were conducted through strain gauges. To visualize the flow, a plate was placed vertically behind the model in freestream direction in the XZ-plane, and an emulsion of aluminum oxide and kerosene was sprayed uniformly over the plate surface. Pictures were taken at several time instances, which are shown in Figure 2.1b. Also, the streamline patterns are sketched, to give a clearer representation of the flow.

By combining flow visualisation with a quantification of the drag, the cause in drag variation could be lead back to specific areas in the flow. From the upper and lower edge at the rear end of the car the flow separates and reattaches again towards the centre of the rear. Therefore, at the base of the wake behind the car, a recirculation bubble formed. This recirculation bubble causes a deviation of the streamlines from their original path, which close around the bubble. The flow in this separation bubble is split up in an upper and a lower regime, where the flow goes down from the trailing upper edge in the upper regime, and flow goes up from the trailing lower edge in the lower regime. For the fastback and estate configuration, the lower regime is rather large compared to a smaller upper regime, whereas both regimes are of comparable size for the notchback configuration.
Following the separation bubble, two longitudinal, contra-rotating vortices are formed over the sides

of the car, interacting with the wake as well. The vortex cores of these contra-rotating vortices were measured as being the center of the lowest velocity region inside the vortex. The vortex cores for each configuration were located at approximately 0.2 times the model width (0.2 x/W) away from the center plane. The spatial location of these vortices is provided in Figure 2.2a.

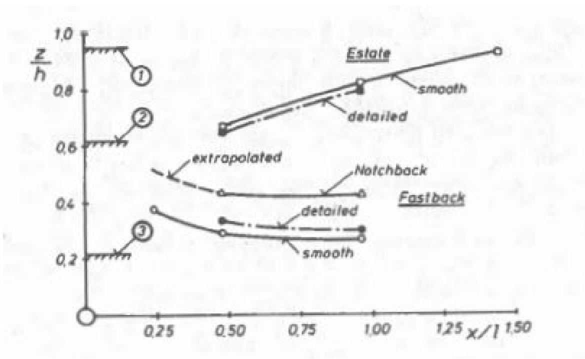

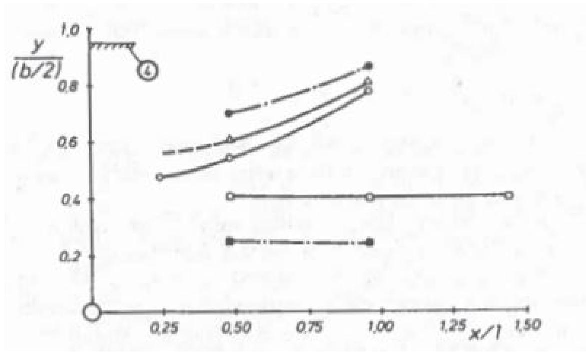

(a) Left: locations of the vortex cores above the ground. Right: locations of the vortex cores away from the central plane

The location of these vortices is essential for safety during poor weather conditions, when it is raining or when there is a lot of dust on the road. Also, due to the wake structures, large side forces can start to occur when overtaking another car, especially in strong side wind conditions. These vortices emanate up and move towards one another for the estate configuration, whereas they move down and depart from one another for the notchback and fastback configuration. Moreover, the vortices dissipate faster for the estate configuration as these move up and interact with the freestream flow.

Ahmed et al., 1984 continued his work with his coworkers in the flow topology of the Ahmed car model. In this study, the aim of the researchers is to establish the typical time-average flow structures in the wake of standard automobile shapes and to describe how the geometry of such a body effects the structure of the wake, the drag and the pressure distribution, because most drag results from the flow behaviour behind a bodies rear end.
For this research, the same model from Ahmed, 1981 was used with pressure taps. A ten hole directional probe was used to investigate the wake. This probe was installed on a rigid carriage, which could be moved to any location inside the wind tunnel. The force measurements were conducted using a strain gauge balance arranged below the ground plane. A drag wake coefficient of 0.415 for 5° base slant angle was measured. The analysis showed that the wake drag is by far the largest contributor to the total drag of the body, with a minimum of 91%. The remaining drag consists mainly of friction drag.
The unsteady wake flow, when averaged over time, shows a macro-structure which regulates the rear end pressure drag. The shear layer from the slant side edge forms a vortex in the longitudinal direction. At the edges located at the top and bottom of the model, two circulation regions are identified, which form a circulation bubble, referred to as region D. The upper is referred to as region A, whereas the lower is referred to as region B. These circulation regions diminish towards the sides of the car. Therefore, they can be visualised as two horseshoe vortices, with the legs of these vortices in parallel direction to the cars base surface. The strength of these vortices can be mainly attributed to the base slant angle, that is, the larger the angle the stronger the vortices. For slant angles below 12.5° the flow remains attached to the slant surface. Between 12.5° and 30° a recirculation bubble occurs due to separation and reattachment over the slant surface. The typical time-averaged macro-structures in the wake of the model are shown in Figure 2.3.

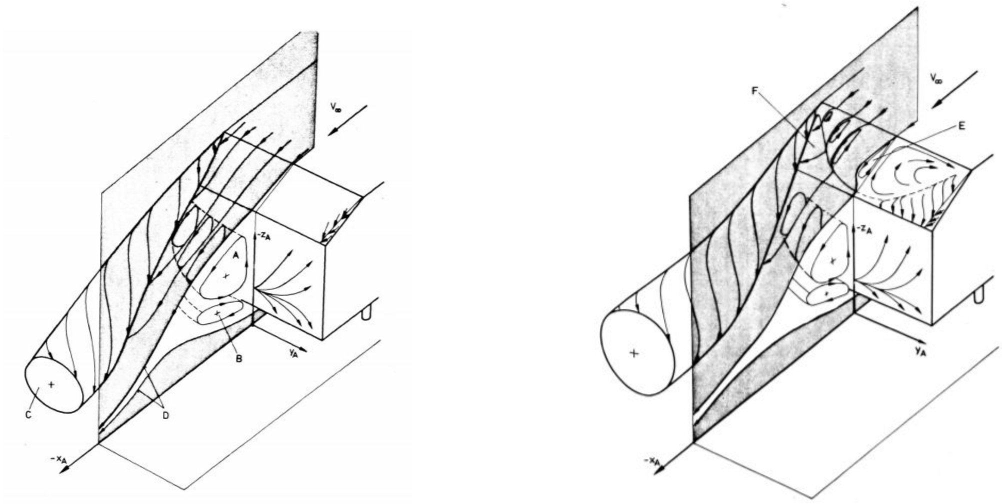

Figure 2.3: Time-averaged wake structures at different angles. Left: below $12.5°$, hence without separation. Right: between $12.5°$ and $30°$, hence with a recirculation bubble over the slant

In another research towards the flow and turbulence structures in the wake of a simplified car by S.Becker et al., 2002, laser doppler anemometry and hot wire anemometry are employed for the research of the wake of the Ahmed body (1044 mm length and 318 mm width). Up to a slant angle of 30°, the two side slant vortices are responsible for keeping the flow attached to the surface. The flow becomes separated for slant angles larger than 30°. The vortical structures for a slant angle of $25°$ are shown in Figure 2.4:

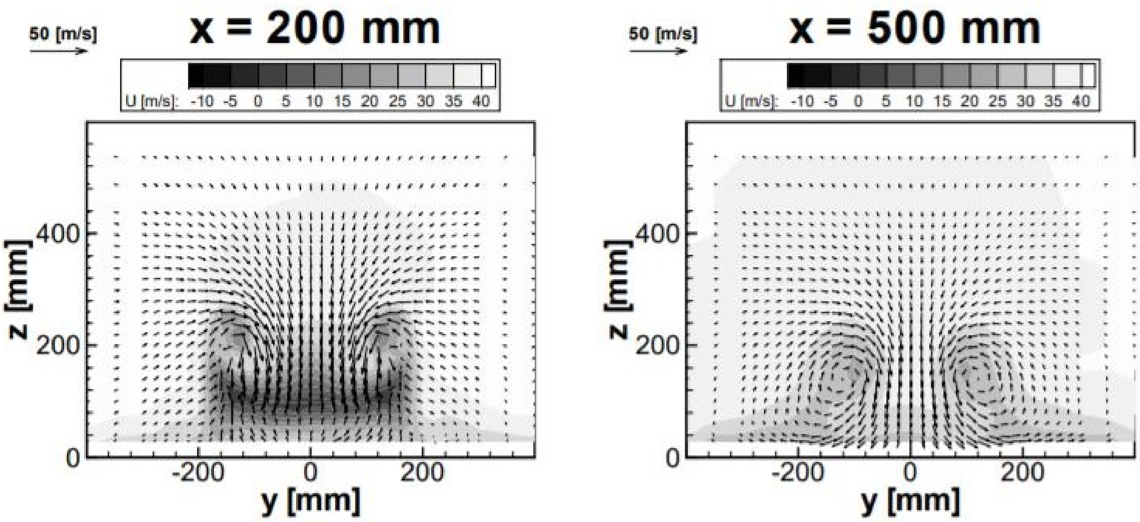

Figure 2.4: Near wake vortical structures behind the 25° Ahmed body

The different slant angles generate different flow patterns behind the body. The side vortices are generated and clearly shown, where close to the body the recirculation is also still apparent (shown on the left in Figure 2.4). These vortices are a result of the C-pillar vortices already (partly) merging with the A-pillar vortices, generating these two distinct counter-rotating vortices.

M. A. Passmore et al., 2010 assessed the suitability of particle image velocimetry when applied to the automotive industry. The accuracy of particle image velocimetry is related to the mean velocity calculation. For an automotive plane diffuser, the 99% confidence interval using 1000 image pairs for the mean velocities are estimated to be +/- 2%. For the RMS velocity field, also from 1000 image pairs, several mechanisms of flow reattachment around a leading edge radius are demonstrated. The instantaneous and time averaged velocity fields around an A pillar vortex do not match the values found in literature.

X. W. Wang et al., 2013 investigated the turbulent near wake of an Ahmed vehicle body. Based on the model height, a Reynolds number of $5.24 \cdot 10^4$ was established for this research. In an earlier work (LES of Krajnovic and Davidson, 2005a) additional lower longitudinal vortices were found together with the C-pillar vortices, which were in that time assumed to be of negligible aerodynamic influence. The study by Strachan et al., 2007 also found these vortices, and concluded that the use of cylindrical strut supports prevents these from occurring.
The ground clearance effect was investigated, by analysing the flow topology around the Ahmed body with and without this clearance. The averaged streamwise component of the vorticity is shown in Figure 2.5 for a slant angle of $25°$, in the YZ-plane.

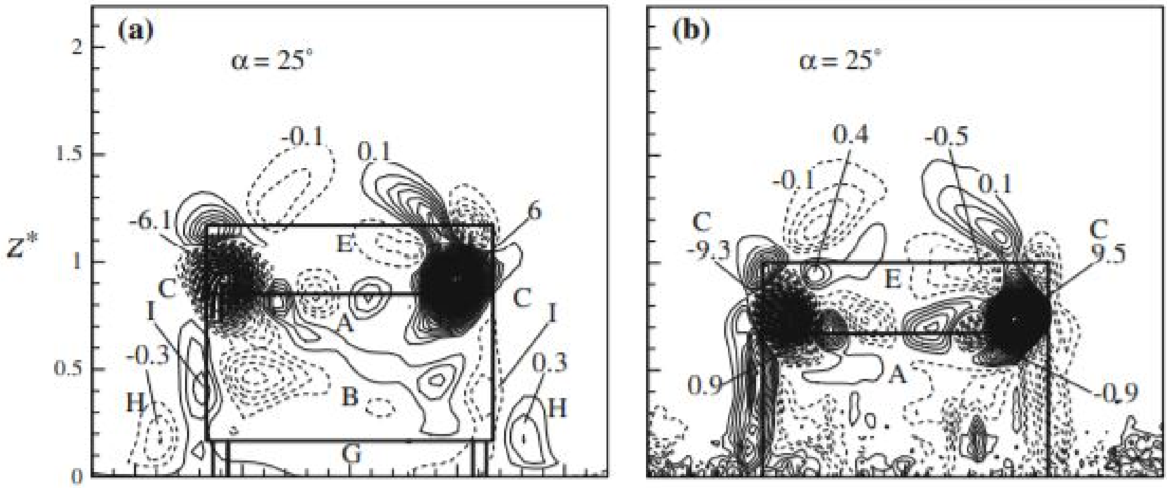

Figure 2.5: Lower vortices H found by X. W. Wang et al., 2013 for the model with a ground clearance on the left versus a model without ground clearance on the right, at distance x/H = 0.23 in the wake

In these images, the strong C-pillar vortices are clearly displayed. The cores of these C-pillar vortices for the 25° case are located at y/H,z/H = -0.56, 0.9 and 0.52, 0.9, at location x/H = 0.23, where H is the height. Moreover, two more longitudinal vortices occurred for the model with a gap, near the lower corners of the model, one at y/H = -0.88 and z/H = 0.16 and the other at y/H = 0.80 and z/H = 0.16. These vortices are indicated with the letter H. Their maximum vorticity concentration is about 5% of the C-pillar vortex. The authors suggest that due to the higher pressure region underneath the car and the presence of the boundary layer, the flow is "squeezed" from underneath the car to the sides. Due to the pressure difference and shear layer, the flow rolls up in a similar manner as the C-pillar vortices, but for this case close to the ground. Further down in the wake, the authors note that these vortices are no longer visible based on measurements conducted at the XZ-plane: at y/H = -0.57 and -0.77. For the measurements without a gap under the model (hence without the struts representing the wheels, on the right of Figure 2.5) these vortices are not visible, underlining the argumentation of the authors.

Venning et al., 2017 conducted a study to aim for high spatially resolved, time-averaged PIV simulations to provide additional information about the nature of the complex flow phenomena in the near wake of the Ahmed body. Specifically, the two vortices that are formed inside the separation bubble in the near vicinity of the model. This research helps to answer the question whether these two vortices can be best described by a pair of horizontally aligned horseshoe vortices or by toroidal vortices. In this paper, strong arguments are provided by Venning et al., 2017 that these vortices are actually best described as two horseshoe vortices, in contrast to the toroidal shape that some previous researches suggested. The three dimensional velocity fields show that the A and B vortices decrease in size towards the sides of the car and due to the shear with the free stream flow, the vortices are tilted in the direction parallel to the free stream. This is emphasized by the vorticity at 0.1L (where L is the car length) in the cross-sectional plane and the isosurface plot, which are shown in Figure 2.6. This study also provides support for the hypothesis that the A-pillar vortex feeds into the C-pillar vortex over the side edges of the model, strengthening this vortex, as shown in Figure 2.6.

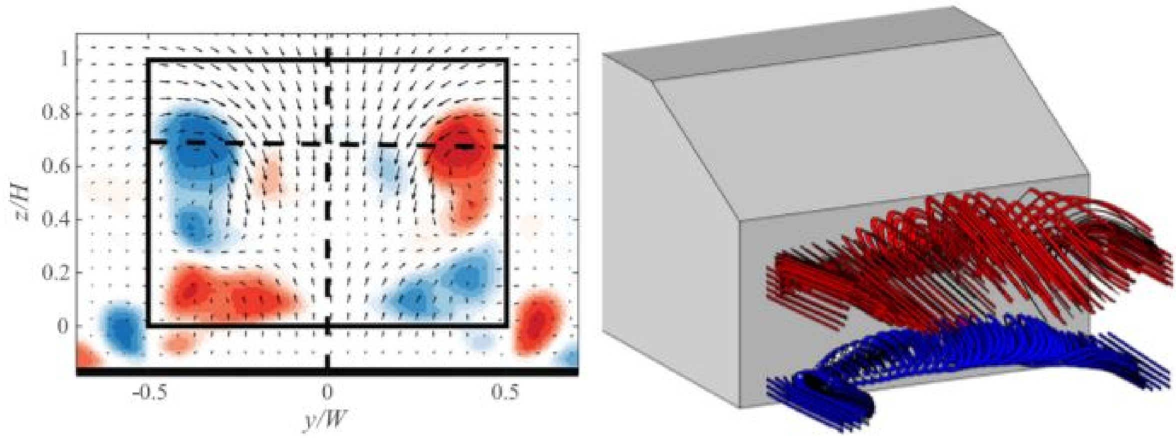

Figure 2.6: Evidence for the horseshoe shape of the B and AC vortices behind the Ahmed body. Left: streamwise vorticity component, Right: isosurfaces of the vorticity Venning et al., 2017

Nonetheless, in contrast to the notchback and fastback, the square-back configuration of the Ahmed body does create toroidal vortex structures in the wake. This is concluded from PIV measurements taken at mid-height for both the square-back as well as the notchback configuration, shown in Figure 2.7:

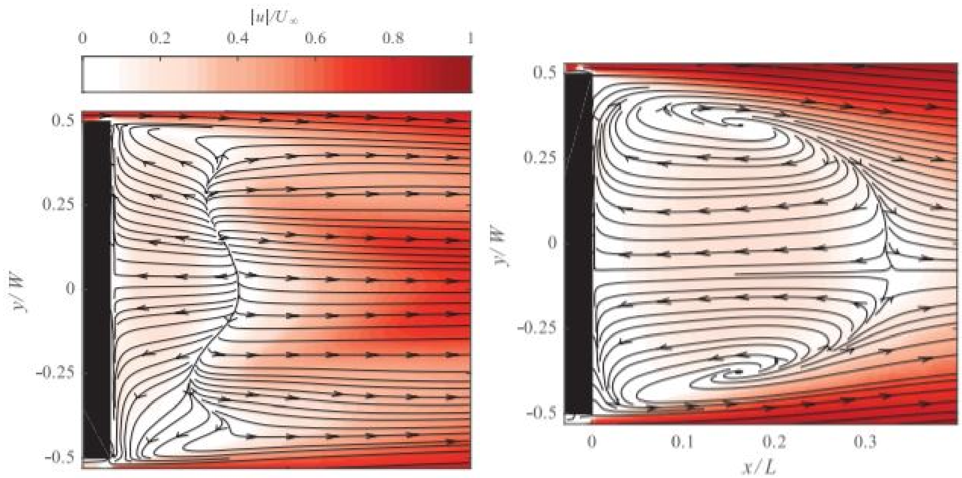

Figure 2.7: Left: horseshoe vortex for $25°$. Right: toroidal vortex for square-back Venning et al., 2017

Rodriguez et al., 2017 conducted experiments on an Ahmed body for slant angle 0°, 25° and 35° with a velocity of 14.3 m/s leading to a Reynolds number of $4.95 \cdot 10^5$, based on the height. The velocity field is recorded using Laser Doppler Velocimetry. These recordings are made in streamwise direction to analyse and determine the length of the recirculation regime behind the car models. For the squareback configuration (slant angle $0°$), this resulted in 1.38 x/H, (with H the height of the model), for the $25°$ this resulted in 0.57 x/H and for the $35°$ this resulted in 1.05 x/H.

Sellappan et al., 2018 used a 25° slant Ahmed model to investigate the near wake flow topology of a ground vehicle. A 0.4 scale Ahmed model was used with 115 mm height and 418 mm length, resulting in a Reynolds number of $1.1 \cdot 10^6$. Planar particle image velocimetry, as well as stereoscopic and tomographic particle image velocimetry measurements were conducted to generate velocity fields and provide insight in the flow topology close behind the model. The resulting streamwise velocity fields (in the XY-plane) from the tomographic PIV measurements are shown in Figure 2.8 for several lateral positions behind the car. From this, the A-vortex and B-vortex are easily identifiable and it can be seen that at a distance of z/H = 0.6 from the central lateral plane, these vortices have completely vanished, and merged in to a much smaller single vortex. Moreover, at the center plane the vortex core of the A-vortex is located near y/H = 0.65 and x/H 0.15 and of the B-vortex is located near y/H = 0.3 and x/H = 0.2. It can be seen that these cores tend to move a bit downstream when moving away from the central plane in lateral direction towards the side of the model.

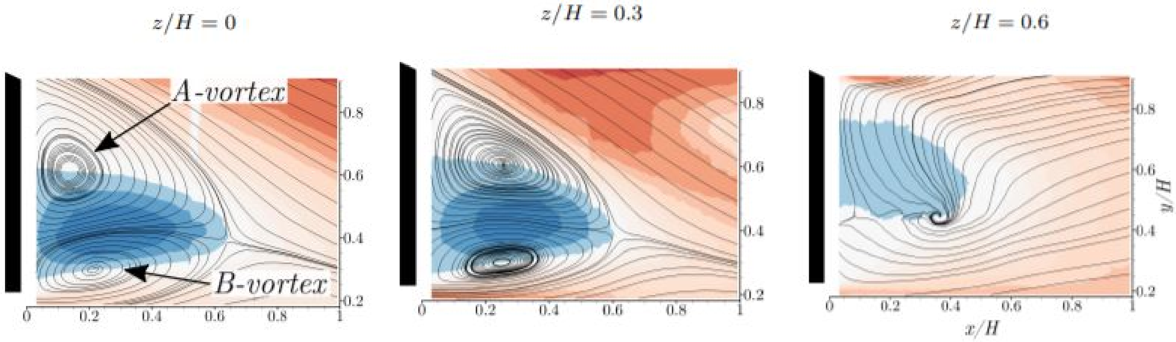

Figure 2.8: Tomo-PIV results for different lateral positions z/H Sellappan et al., 2018

From the stereoscopic PIV measurements the results in the YZ-plane could be visualised, which is the plane perpendicular to the freestream flow. These flow fields are shown in Figure 2.9 for several planes located at different longitudinal x/H locations in the wake.

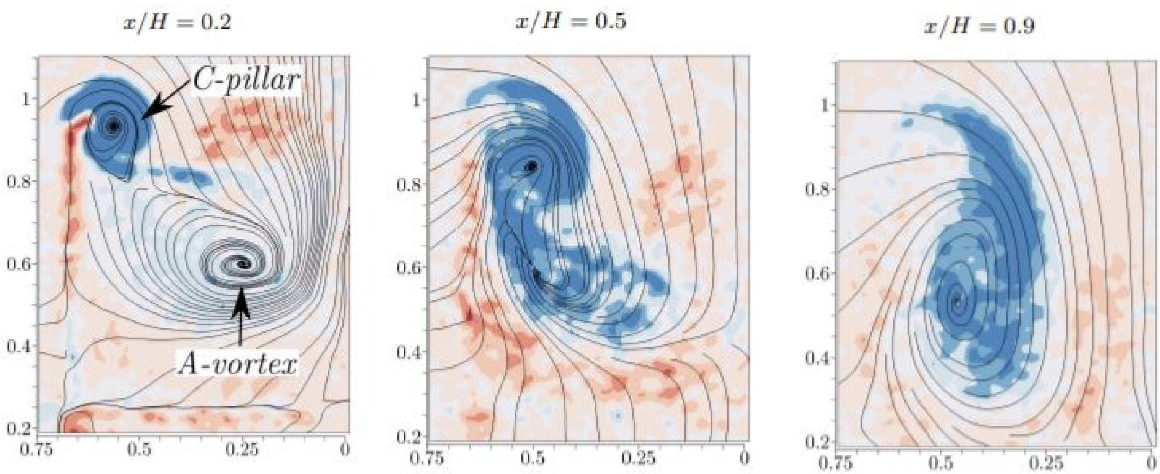

Figure 2.9: SSPIV results for different lateral positions z/H Sellappan et al., 2018

The authors state that these images are created from looking behind the model towards the model, and only the left side of the symmetry plane is visualised. From these images, the creation of the C-pillar vortex is clearly visualised, which starts at x/H = 0.2 from the upper left part of the car. Moreover, the A-vortex is also visualised, implying that this vortex bends from a lateral vortex to a longitudinal vortex, displaying a horseshoe vortex like structure. In contrast, the B-vortex only moves in lateral position and does not bend in freestream direction before it reaches the edge and then curves more upwards, creating an obliquely aligned vortex in a horseshoe shape. When moving downstream, the images at x/H = 0.5 and x/H = 0.9 show a clear merging process between the C-pillar and A-pillar vortex, creating one large vortex. The core of this large vortex is located around z/H = 0.45 and y/H = 0.55 on both sides of the central plane.
It should be noted that these vortices are comparable to those found by S.Becker et al., 2002 as shown

in Figure 2.4 for z/H = 0.2 and z/H = 0.5.

2.1.2 The DrivAer model

Since strongly simplified models such as the Ahmed body are very abstractly shaped, they do not accurately represent the flow around detailed and complex real cars. Therefore, in a paper by A. I. Heft, 2011, a new reference model car is developed and analysed. A combination of the Audi A4 and BMW 3 series is used to generate the DrivAer model, which provides a much more accurate representation of real cars. The three different DrivAer model configurations (fastback, notchback and estate) are shown in 2.10. For both these models, a numerical and experimental analysis is performed and these are compared.

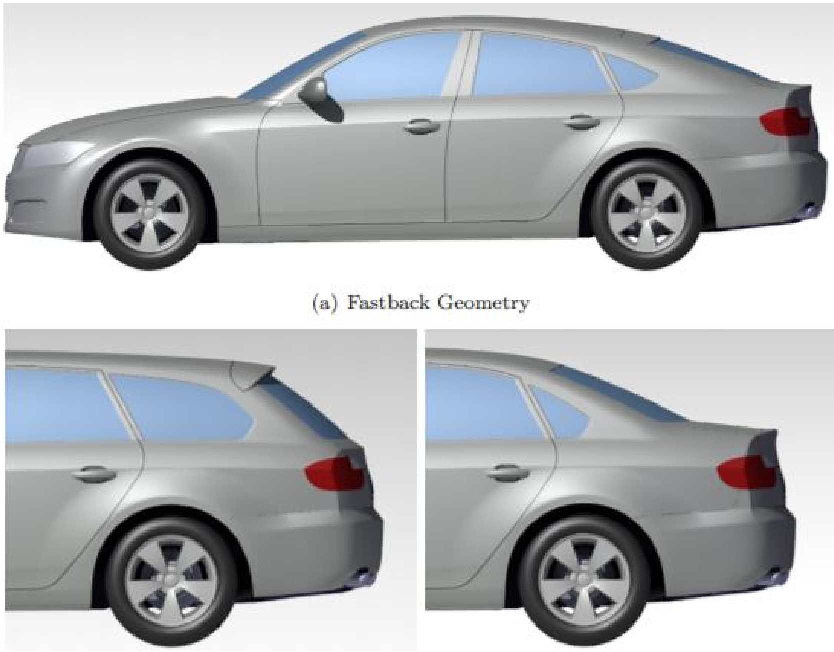

(a) Fastback Geometry

(b) Station Wagon Geometry (c) Sedan Geometry

Figure 2.10: DrivAer model configurations as designed by A. I. Heft, 2011

The authors point out that the flow behind a vehicle is highly turbulent and therefore unsteady. These unsteady wake structures and periodic vortex shedding cause fluctuations in the pressure, resulting in varying forces and moments, affecting the safety and driving comfort. Since the production cars cannot be simulated due to the enormous computational costs, a more representative model than the more generic and abstract Ahmed or SAE body is needed. The experimental and numerical results are discussed in Subsection 2.3.2.

In this paper, Strangfeld et al., 2013 perform an experiment with the DrivAer model car in a closed-loop wind tunnel. The main focus of the research is to analyse the flow structures occurring in the near wake of a fastback model configuration. To measure the forces and surface pressures, an internal balance in accordance with pressure sensors is used. A qualitative flow visualisation is conducted through a PIV analysis at the plane of symmetry of the car, shown in Figure 2.11.

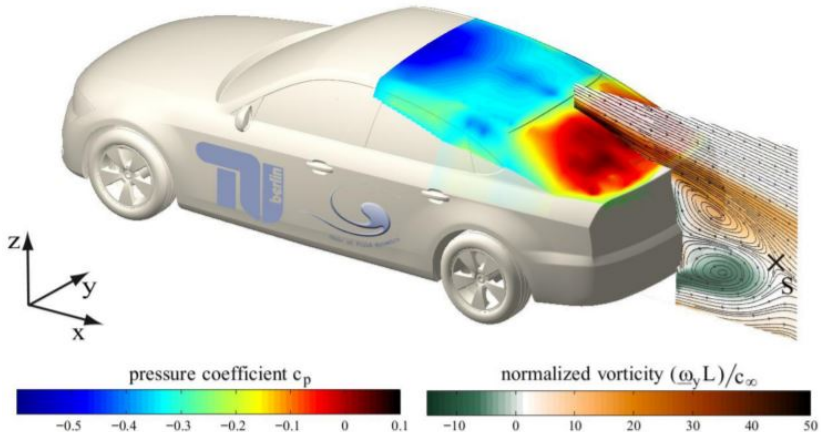

Figure 2.11: The pressure over the back of the car and the vorticity in the wake with the streamlines Strangfeld et al., 2013

Authors note that although the recirculation zone behind the car creates additional drag in terms of a low pressure peak, it could be that this zone allows for flow attachment over the rear window and could have a positive overall effect. The results are in accordance with those found in other literature and numerical simulations, where the found drag coefficient was 0.249 for this research.

In a later study conducted by Liu et al., 2021, the research towards the DrivAer model continued. An automated PIV technique for measurements on a 1/16 scale DrivAer standard model was implemented to analyse the three-dimensional wake structure. The PIV measurement planes were located in the spanwise and vertical direction. The authors emphasize the need to compare Ahmed body flow structures to the different DrivAer flow structures, since the DrivAer model may create regions in the wake flow topology that deviate from the Ahmed body wake flow topology.
Measurements of DrivAer model were performed in the spanwise and the vertical direction, with the cross-sectional velocity fields shown in Figure 2.12. Regions with high velocity fluctuations mainly locate at the shear layer of the upper and lower edge of the recirculation bubble. C-pillar vortex inhibits the formation of the back recirculation bubble at the rear window and reduces the size of the recirculation bubble behind the baggage compartment. The flow stays attached to the surface above the rear window and therefore there is no large separation bubble appearing. This aids in the development of the trailing vortices which form the C-pillar over the sides of the car. At the top and bottom shear layer of the circulation bubble high intensity Reynolds stress regions occur. Here, the largest fluctuations are present. The authors concluded that the wake structures are comparable to the von Kármán vortex sheet downstream of a bluff body. The consequently high unsteady region shows potential large fluctuations in the force balance. However, a time-resolved force balance shows that the deviation does not become higher than 5%.
From the analysis it also resulted that a newly found secondary vortex pair was present. This vortex is located besides the C-pillar vortex over the side of the car and seems to feed into it, which increases the vortex strength of the C-pillar. As a result, the grip of the car and the driving stability are enhanced. This secondary streamwise vortex was not found in previous experiments of the DrivAer, nor in the studies related to the Ahmed body. This could be ascribed to a different analysis and measurement approach, but it could also be a unique to the DrivAer model, showing the importance of creating models as close to full scale as possible. The C-pillar vortices together with this secondary vortex are shown in Figure 2.12.

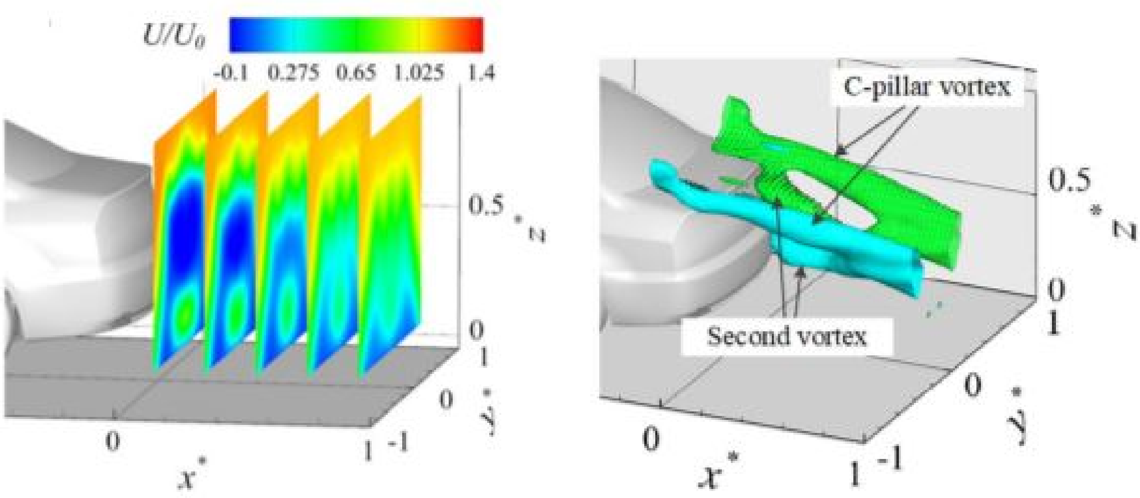

Figure 2.12: Left: near wake velocity fields. Right: C-pillar and secondary vortices Liu et al., 2021

2.2 Numerical studies

Another technique to visualise the flow around a passenger car and compute the aerodynamic forces is by means of numerical simulations. In car aerodynamics, this is typically done by Computational Fluid Dynamics (CFD) simulations. Over the years, this technique has become more advanced, due to the increased knowledge in the flow topology around cars as well as the general improvement of computational speed and cost for computers. Wind tunnels have the downside that Reynolds number effects come into play. Moreover, the costs of building and then running a wind tunnel are very high, meaning that minor changes to a design is most of the time not feasible due to the high cost for a potential small reward. CFD has the advantage that all settings, including wind speed, pressure, density and temperature can all be easily changed and small modifications to a car can be easily implemented without much cost.

2.2.1 Ahmed body

Up to 2005, simulations were capable of accurately predicting the flow structure for the Ahmed body with a slant angle of $35°$, but failed to accurately capture the flow structure for a slant angle of $25°$. Therefore, Krajnovic and Davidson, 2005a aimed to provide an accurate LES analysis to the flow around the Ahmed body with a slant angle of $25°$. The geometry is assumed to be the dominating factor for the separation towards the back of the car: that is, the sharp edges. The assumption is made that therefore the flow at lower Reynolds numbers is representative of those at higher Reynolds numbers, thus lower Reynolds number analysis can be performed. Based on a previous experiment, Reynolds number of $2 \cdot 10^5$ is chosen. For the grid size, a coarse, medium and fine grid were investigated, with 3.5 million, 9.6 million and 16 million nodes, respectively.

In this research, the flow over the slant angle and the near wake flow was the focused area of interest. The LES simulations for the coarse, medium and fine grid are shown in Figure 2.13 from left to right, respectively. The authors found that the length XSL, which is the length of the separation bubble on top of the slant, was approximately equal to 0.28H, 0.3H and 0.35H for the coarse, medium and fine LES grid, respectively, where H is the height of the model.

Next to the bubble on top of the slant, a recirculation region is found attached to the vertical back of the Ahmed body. The extension of this near-wake region was found for the coarse, medium and fine grid simulations to be 0.6H, 0.65H and 0.65H, respectively.

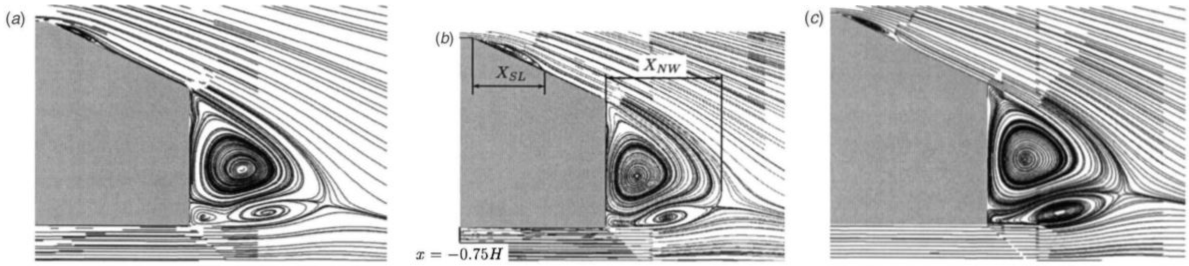

Figure 2.13: LES results in streamwise direction directly behind the Ahmed body Krajnovic and Davidson, 2005a

Even though the vortices that were found are accurately represented and comparable to the studies of Ahmed, 1981 and Ahmed et al., 1984, the different boundary conditions and different geometry (Ahmed only measured for 5°, 12.5° and 30° and interpolated the values in between) lead to unreliable comparable experimental results. For the coarse, medium and fine grid, the drag coefficient values were 0.288, 0.305 and 0.292, respectively. All of these values are higher than 0.24, which is extracted from the study by Ahmed et al., 1984 through interpolation. The root-mean-square (RMS) was found to be about 2% of mean value. Inconsistency in the measurements (i.e. the results do not go only up or down with refinement of the grid) is attributed to the fact that the coarse grid is too coarse to give reliable results.
The success of such simulations using LES is dependent on the near-wall resolution. For this, an LES-RANS hybrid simulation is in development, which will be discussed later in this section with the work of Ashton and Revell, 2015. For the analysis and simulation of the flow with separation and reattachment, the authors assumed that the geometry, with its sharp edges, constraints the flow. The result shown in the paper that this assumption is feasible. Apparently, the Reynolds number does not influence the result, since comparable results are achieved for the LES results with a Reynolds number four times less than in the experiment by S.Becker et al., 2002.

In a following study, conducted by Krajnovic and Davidson, 2005b, the research with the LES simulation was extended. For this paper, only the fine grid was considered, which contained 16.5 million nodes. The Ahmed body had a $25°$ slant angle and a Reynolds number of $2 \cdot 10^5$.
From the analysis of the results, vortices were found next to the edge between the body lower and side surfaces. The authors hypothesised that these were most likely formed due to the deceleration of the flow by the boundary layers formed underneath the body and on top of the floor. The flow is therefore pushed to the lateral sides to satisfy continuity, which results in vortices on both sides of the body. The development of these vortices is shown in Figure 2.14, where only one side of the body is visualised, looking at the body from the front. The displayed images are for x = -2.08H, x = -1.39H, x = -0.69H, x = 0, x = 0.21H and x = 0.38H, where the origin of the x-axis is located at the rear surface of the body, with the positive axis in downstream direction.

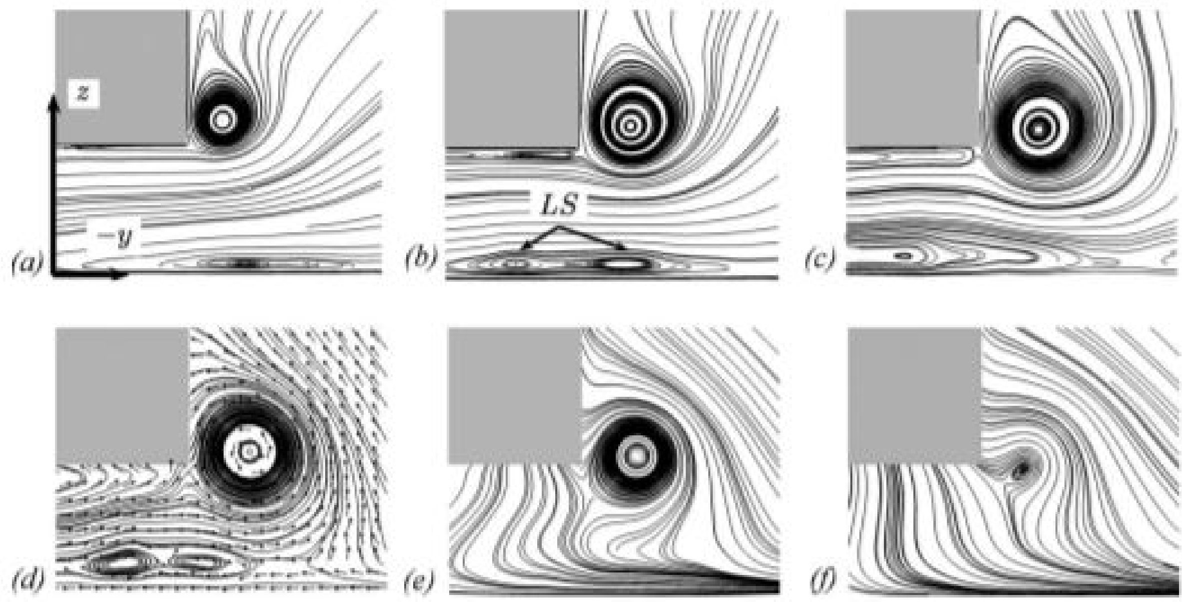

Figure 2.14: Vortices from underneath the body Krajnovic and Davidson, 2005b

The near-wake flow behind the body is analysed in depth. To properly do this, the authors provide an overview with streamlines and vortex cores on planes in all three directions across the wake. Moreover, the development of the wake is visualised with pressure isosurfaces (for p = -0.16 and p = -0.19) and a schematic overview of the time-averaged flow development is provided. These figures are provided below, in Figure 2.15.

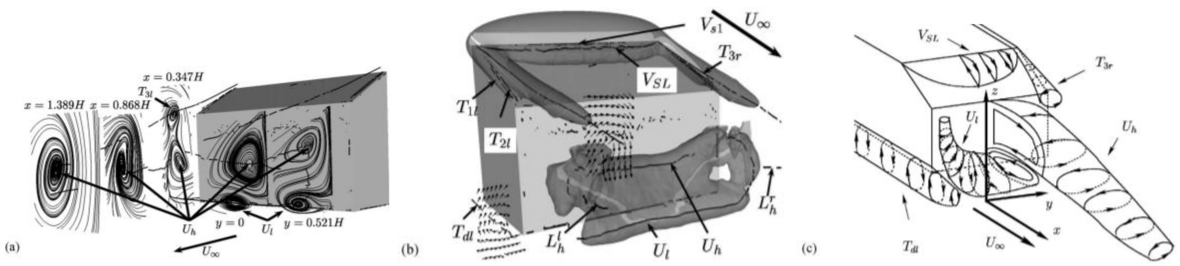

Figure 2.15: a) The streamlines in multiple planes, b) pressure isosurfaces and c) schematic overview of near-wake flow structure Krajnovic and Davidson, 2005b

When compared to the wake structures provided by Ahmed et al., 1984, the authors reshape the U_l (or A vortex) to go upwards in the positive z-direction, "sticking" to the vertical rear surface instead of being an extension flow in downstream direction. It is suggested that this was a erroneous interpretation of the vortex by Ahmed et al., 1984. The side vortices caused by the flow being pushed out in lateral direction from underneath the body are weak and can safely be assumed to have a negligible effect on the much stronger U_l vortex.
The rear slanted surface thus contains 3 vortex like structures instead of the previously reported 2 vortex like structures. The authors point out the lack of instantaneous flow field and research around car structures. Even though the pressure forces and other aerodynamic forces and moments can be retrieved from the time-averaged flow, the change in these follow from the instantaneous flow fields. These instantaneous fields are often very different from the averaged flow field.

2.2.2 DrivAer model

In a later study, conducted by Ashton and Revell, 2015, RANS simulations of the DrivAer automotive body are compared to hybrid RANS-LES methods. The aim of the study is to analyse the applicability of DES for complex flows in the automotive research. Authors found that a RANS simulation is not capable of capturing the unsteady flow field accurately, whereas DES shows more promising results, as the drag and pressure coefficients are simulated quite accurately. The trends of the DES simulations compared to experimental results are comparable. The study showed that DES has a clear advantage over RANS to accurately capture the pressure coefficient and force values in unsteady areas. Nonetheless, even the finest grid was unable to correctly capture the flow, thus either a different method should be used or the DES method should be improved.

2.2.3 Realistic estate-type car

Huang and Sheu, 2015 investigated the vortical flow structure in the wake of Mitsubishi Freeca, an estate-type car. A differential turbulence stress model is employed, where through a finite volume method the three-dimensional Reynolds-averaged Navier-Stokes equations together with Reynolds turbulence transport equations are solved. The Reynolds number used for this simulation is $8.05 \cdot 10^6$. The results show the following lines for the vortex core locations on the left, and the streamlines on the right, displayed in Figure 2.16:

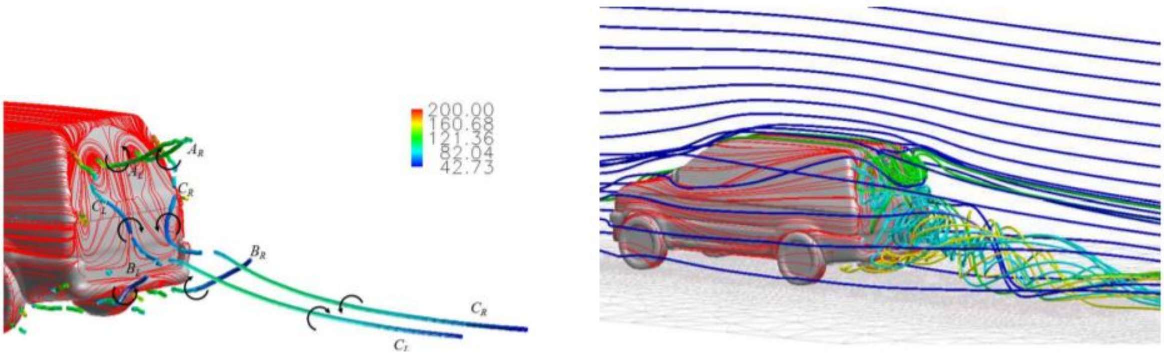

Figure 2.16: Left: lines indicating the core of each vortex. Right: streamlines on and around the car Huang and Sheu, 2015

From these figures it can be clearly seen that the CFD results are comparable to previously conducted experimental studies for estate-type cars (e.g. Ahmed, 1981, Ahmed et al., 1984). The upper vortex A in Figure 2.16 moves upwards due to the induced upwash and later merges with vortex C. Vortex B merges with vortex C close downstream of the vehicle. On the right, the streamlines are nicely visualised, showing the turbulent time-averaged structure of the wake behind the car. In red, the streamlines on top of the surface are shown, in green vortex A is shown, in light blue vortex C is shown and lastly in yellow vortex B is shown.

2.3 Studies comparing experimental and numerical measurements

In the previous sections, studies only focusing on the experimental measurements or numerical measurements have been laid out. However, there is also an extensive number of researches where the experimental and numerical measurements are conducted for the same research. A focus on the analysis of the wake topology and drag is set out in this section.

2.3.1 Ahmed body

Duncan et al., 2002 investigated a 25° slant angle Ahmed body computationally. Even though this section includes papers with both experimental as well as numerical measurements, this is a predecessor of a following study which did include both experimental and numerical measurements. A Lattice-Boltzmann combined with a Very Large Eddie Simulation was used to analyse the flow. The development of the wake flow is quite accurately captured and visualised in Figure 2.17.

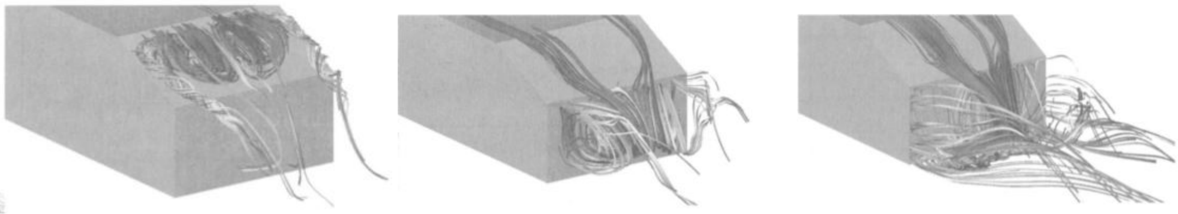

Figure 2.17: a) The development over the slant, b) near-wake development c) wake development further downstream Duncan et al., 2002

Moreover, the velocity fields were visualised using vectors. In these velocity fields, shown in Figure 2.18, the C-pillar vortices are clearly visible and are even already merged with the typical A-pillar vortex coming from behind the body.

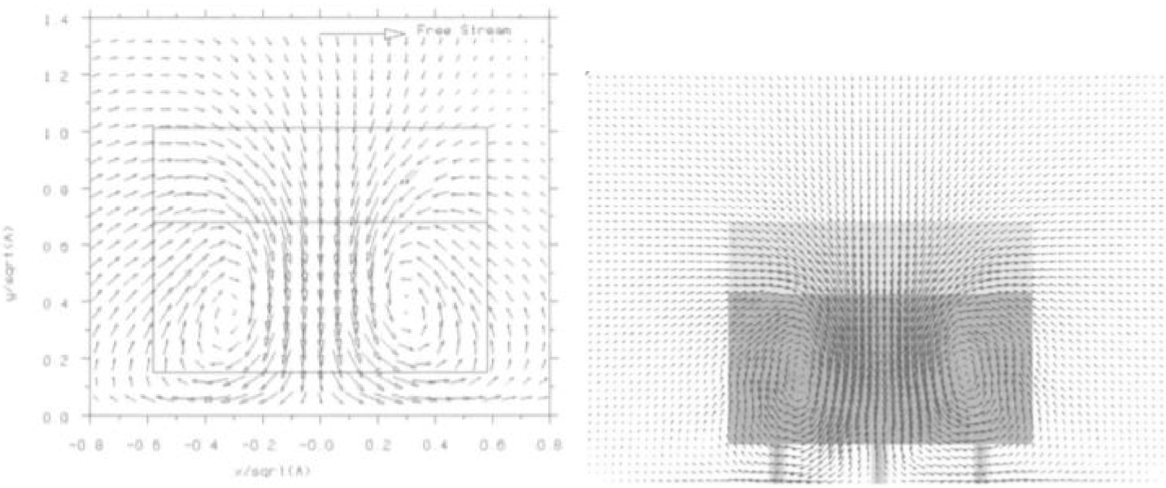

Figure 2.18: Left: the experimental velocity field. Right: the CFD velocity field Duncan et al., 2002

Due to only short simulation capabilities in the first research, a next research was conducted by Duncan and Sims-Williams, 2002. For this research, a 5-hole pressure and hot wire probes are used for the experiment and ExaPowerFLOW for the CFD analysis. The previous study, with half the size of this model showed that the simulation required a slant angle well below the critical angle of 30° (so 25°) in order to simulate the stable separation and reattachment at the slant. Quasi-two-dimensional instability and vortex shedding occur due to the shear layer over the rear slant. Also, due to the interaction of the flow coming from underneath the car with the shear layer, vertical vortex shedding occurs in the wake. In this study, a longer simulation showed periodic unsteadiness for these regimes.
The time-averaged results for the experimental study are shown in Figure 2.19, whereas the results for the numerical study are shown in Figure 2.20. These show the typical vortex structures with the core located approximately y/sqrt(A) = 0.45 at a distance x/sqrt(A) = 1.0 behind the model. More separation occurs in the CFD than in the real experiment, leading to a higher wake regime. The cores of the vortices are closer to the centerline, at around y/sqrt(A) = 0.35. Higher unsteadiness in the CFD simulation are closer to those found for bodies with a slant angle close to the 30° critical angle than for the 25° slant angle.

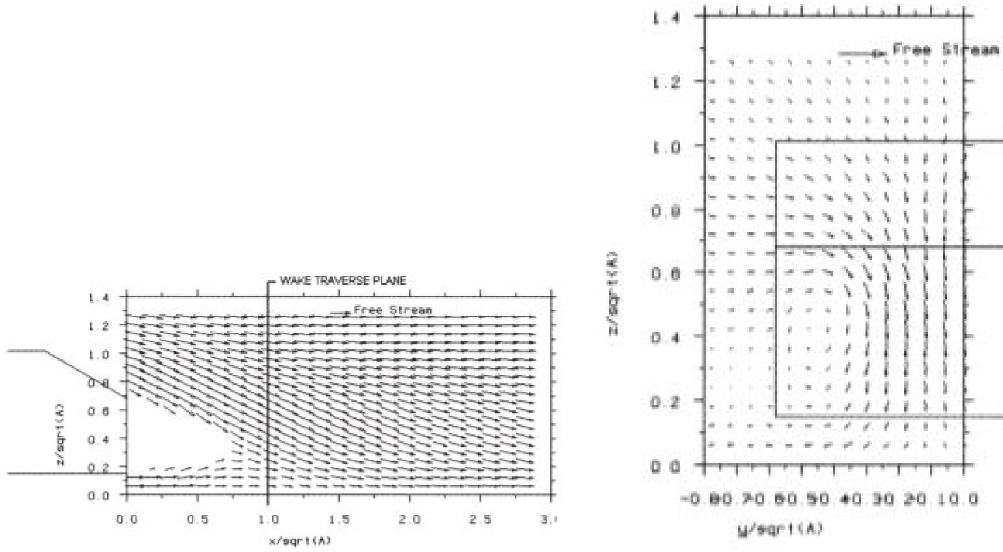

Figure 2.19: The experimental velocity field in a) the streamwise central plane, b) the lateral plane at x/sqrt(A) = 1.0 Duncan and Sims-Williams, 2002

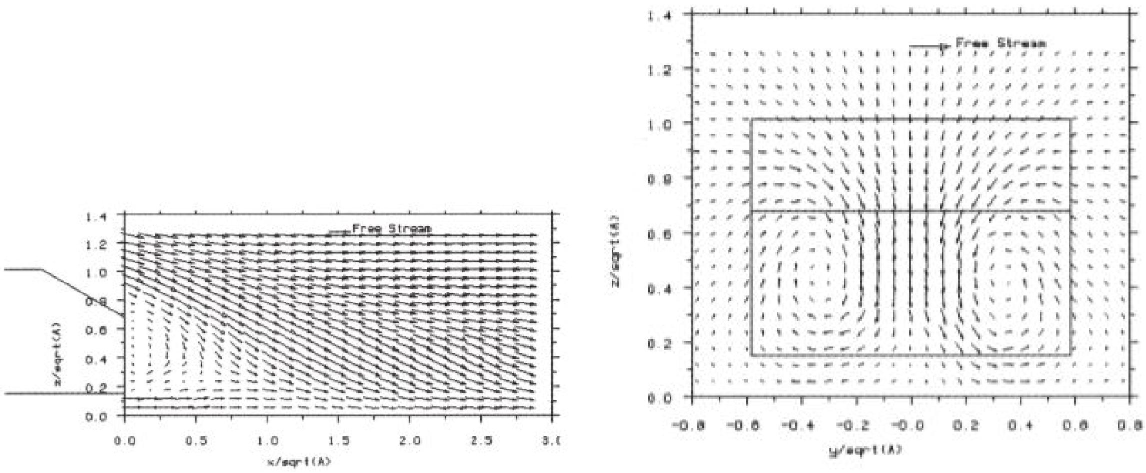

Figure 2.20: The numerical velocity field in a) the streamwise central plane, b) the lateral plane at x/sqrt(A) = 1.0 Duncan and Sims-Williams, 2002

Strachan et al., 2004 investigated the velocity field in the near-wake of the Ahmed body through CFD and experimental measurements. Laser Doppler Anemometry (LDA) is used to visualise the flow around the 25° slant angle Ahmed model and a 3D fluent CFD analysis is performed as well.
At x/L = 1.0, the U/U_∞ flow field is provided in Figure 2.21, where two counter rotating vortices are present in the wake. For the CFD, these are located at z/L = 0.12 and y/L = 0.15. For the LDA, these are located at z/L = 0.1 and y/L = 0.12. The vortices are not completely symmetrical for the LDA case, which is expected. This fact attribute the authors to be most likely a slight misalignment of the model. Comparison between CFD and experiment concludes that the vortex centers vary with about 0.03 x/L between the results.

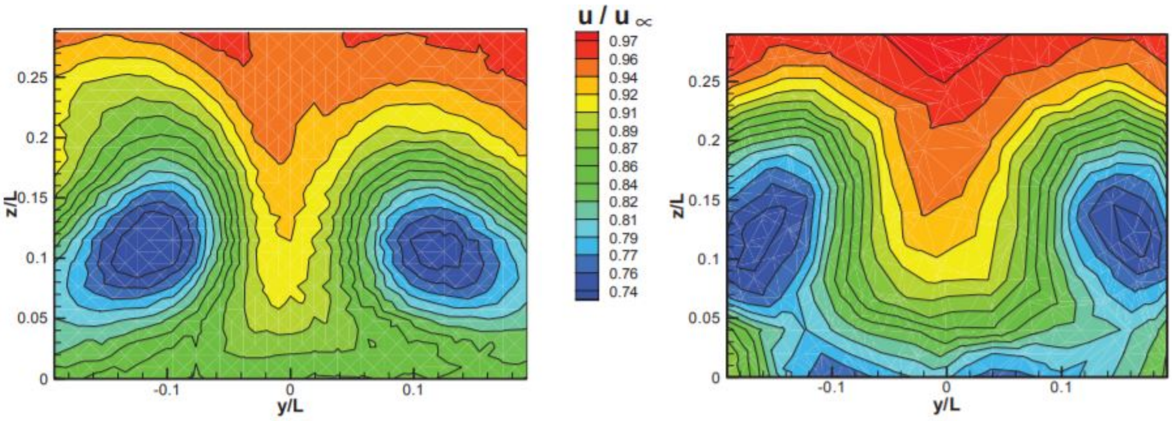

Figure 2.21: Velocity field comparison from Strachan et al., 2004

The drag coefficient is well predicted by the CFD. However, a breakdown of the different surfaces (front, rear, slanted) compared to Ahmed et al., 1984 shows that there are large differences found for the relative drag contributions. Where Ahmed, 1981 found values for the front, inclined section, back and viscous of 6.78%, 50.85%, 25.42% and 29.41%, the CFD results showed 22.5%, 15.77%, 39.41% and 22.32%, respectively. Therefore the conclusion can be drawn that although CFD can rather accurately predict the flow structure around the model and in the wake, it is unable to accurately compute a quantitative breakdown of the forces.

2.3.2 DrivAer model

The results obtained by A. I. Heft, 2011 are discussed in this subsection. Preliminary Reynolds-Averaged Navier-Stokes simulations were performed for a model based on the Audi A4 and BMW3 series, to further optimize the model. Three interchangeable rear ends (fastback, sedan and station wagon form) are designed for the model, along with two different underbody surfaces, to allow for a wide range of model shapes, thus applicability. For the numerical analysis, Large Eddy Simulation (LES) and Scale-Adaptive Simulation Shear-Stress Transport (SAS SST) were used. LES simulations are able to capture the vortex structures that are typically occurring at the Ahmed body rear end. Authors point out that due to an insufficient mesh resolution, inconsistencies of velocity profiles over the slant with literature are apparent. To describe the unsteady vortices, steady state is not satisfying and therefore transient turbulence models such as SAS SST and LES should be considered. Also for the DrivAer model, the SAS SST seems to capture the vortex structures adequately. Even though the coarse grid results in slight deviations of the turbulent flow simulation, a finer grid was too expensive. For the experimental analysis, time-accurate surface pressure and force measurements were conducted. Comparing the numerical results to these experimental results, the SAS SST shows good results, shown in Table 2.1. Although the SST shows the most promising results, the authors ascribe this to a summation of different errors. Therefore, the authors conclude that the SAS SST model proved to be the most suitable for this simulation.

Table 2.1: Comparison between numerical and experimental results for DrivAer, reproduced from A. I. Heft, 2011

	Experiment	SST	LES	SAS
C_D	0.297	0.302	0.256	0.275
$\Delta C_{D,exp}$	0	2%	14%	7%

2.4 On-road measurements

Next to the state-of-the-art measurement techniques used in wind tunnels and the numerical simulations using CFD, experiments intended to gain knowledge about the aerodynamics of passenger cars are also conducted on-road or on-site. Usually, such an on-road measurement is conducted through a coast down measurement. Coast down measurements are performed in the normal operating environment of cars, thus in open air and on a real road. Therefore, it is an exact representation of the drag behaviour of the car during its operational lifetime, which is a large benefit compared to wind tunnels and CFD, which will always be approximations of reality. During a coast down measurement, the car is accelerated up to a certain speed. When this speed is reached, the car is released in its neutral setting and allowed to freely decelerate. Through empirically obtained formulae for the friction and using equations expressing the mechanics of the car, the aerodynamic drag can be calculated. The equation is fitted according to the measured speed data where the sum of errors squared is minimised. Thus, the accuracy of the measured aerodynamic drag force is strongly dependent on the quality and realism of the used mathematical models.

One of the first series of researches using the coast down measurement technique was conducted by T. Buckley, who started researching this technique in 1976. A series of 11 researches followed, summarised in Walston et al., 1976b and Walston et al., 1976a. In 1995 a paper was written in which the author concluded and merged all of his researches in one specific coast down test and analysis method: the ABCD method Buckley, 1995. This is an anemometer method, where the anemometer extracts the wind speed and yaw angle during measurement, to ensure accurate data. In the early development years of the coast down techniques, non-anemometer methods were used and although they were simple and fast to conduct, the wind and yaw angle were not accounted for thus resulted in poor data. This method was able to capture the drag coefficient for typical cars, where the results fell between wind tunnel data corrected for pressure-signature blockage and for continuity, as shown in Figure 2.22.

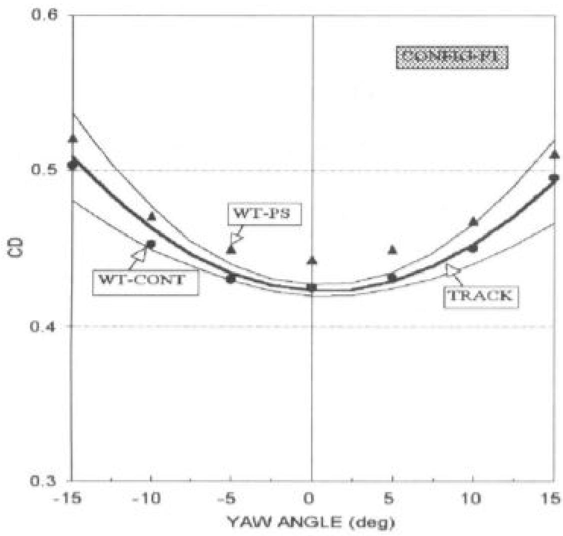

Figure 2.22: Cd vs yaw angle for typical automobiles Buckley, 1995

This showed the feasibility of this method and consequently also full-scale trucks could be tested, which are infeasible to test in the wind tunnel. Full-scale truck-trailer combinations were also tested. The ABC method is thus able to capture the highly unsteady drag in yaw conditions.

Good et al., 1998 compared the aerodynamic drag measurements inside the Pininfarina wind tunnel with coast down drag measurements. The Pininfarina wind tunnel was developed such that real scale cars could be tested on a moving ground, which allowed a more precise comparison between coast down drag measurements and wind tunnel tests. The coast down technique developed by Passmore M. Passmore and Good, 1994 was used in this paper to analyse the drag coefficient of the European car

Rover 820Si. The results are shown in Figure 2.23, from which it can be concluded that for the standard configuration with changing spoiler height and standard rough floor, the coast down drag result is 0.009 higher than the drag coefficient from the MIRA wind tunnel (excluding moving ground and including a correction for continuity blockage) and only 0.002 higher than the Pininfarina wind tunnel (including moving ground), showing the close agreement of this coast down technique with wind tunnel data.

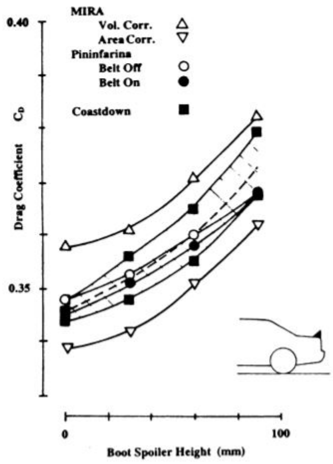

Figure 2.23: Comparison between drag coefficient from coast down measurements and wind tunnel measurements in MIRA and Pininfarina wind tunnel Good et al., 1998

In 2001, the ABCD coast down measurement technique developed by Buckley, 1995 was used in the Lockheed Low Speed wind tunnel to conduct a correlation and uncertainty analysis of the coast down technique, by comparing with wind tunnel data Walter et al., 2001. The absolute values of the coast down technique were lower than both the pressure-signature and continuity blockage corrections, whereas for the study conducted by Buckley they fell in between Buckley, 1995. Nonetheless, the systematic uncertainty was predicted to be within 4% at the 95% confidence interval, where the random uncertainty varied between 1.5% and 2.5%.

Howell et al., 2002 investigated the coast down technique on-road for a compact SUV by comparing the measurements with wind tunnel data. Previous researches have mainly investigated typical passenger cars and showed promising results, thus an interest in implementing this technique for an SUV car was sparked. In this research, it was concluded that there is a more consistent aerodynamic drag coefficient result compared to wind tunnels, which benefits this technique. Furthermore, a good correlation is found between the coast down technique and wind tunnel tests of the same vehicle as shown in Figure 2.24. This technique can therefore be used to demonstrate the effectiveness of other ground simulation strategies.

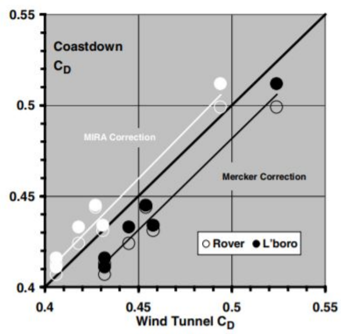

Figure 2.24: Correlation of SUV drag coefficient between coast down and wind tunnel measurements

2.5 Thesis objective and relevance

The literature in research towards the aerodynamic behaviour of the flow in the wake of cars is limited. Most available research has been conducted for simplified bodies (such as the Ahmed body), and scarce research is conducted towards the wake behaviour around more detailed car models (such as the DrivAer) which are more representative for the complex shape of real cars. Moreover, a large part of the research either focusses only on visualizing the flow behaviour around the car or only on determining the drag. With the implementation of the Ring of Fire system for on-site car aerodynamics, this project is the first research where the flow is visualized around a full-scale car outside the wind tunnel, where simultaneously the drag can be determined from the control volume approach. The goal of this research is therefore to investigate the applicability of the Ring of Fire system for the automotive industry, and identifying if it is a suitable measurement system for further aerodynamic research towards e.g. cornering and drafting, which are either very difficult or impossible to measure through other techniques. Based on the aforementioned research gap, the objective of this thesis is formulated as follows:

Implement the Ring of Fire system for full scale passenger in an outdoor, on-site environment and assess its feasibility for the automotive industry. Additionally, test the accuracy and uncertainty of the drag through comparison with wind tunnel measurements

Previous experiments towards the aerodynamic flow behaviour around cyclists have shown the feasibility and novelty of the Ring of Fire for the characterisation of the aerodynamic behaviour of transiting objects. Therefore, this project is an extension of this technique to the automotive industry.
A successful outcome of this project would show agreement with the state-of-the-art literature flow visualisation for comparable car models. Moreover, an agreement in uncertainty and accuracy of the drag values compared to previous Ring of Fire experiments for outdoor measurements would show that the Ring of Fire is a suitable, additional technique that can be used in the automotive industry. Lastly, good agreement between the drag values from the Ring of Fire and the wind tunnel experiments conducted with the same cars by Volkswagen would lead to a successful outcome.

Chapter 3

Background of the Ring of Fire concept

In this chapter, the fundamental principles of Particle Image Velocimetry are laid out in order to get a solid understanding of the theory that the Ring of Fire system is based on. Firstly, in Section 3.1, an overview is given of a standard PIV set-up, introducing the tracer particles, illumination and imaging, which allow the measurement of the flow velocity. For the drag analysis, the out-of-plane velocity is required and therefore stereoscopic PIV is emphasized. Moreover, the additional principles behind large-scale PIV in contrast to small-scale PIV are explained. Furthermore, in Section 3.2, the control volume approach is presented and the manner in which it is used in the Ring of Fire technique. This approach is implemented to calculate the drag of the cars. Moreover, the reconstruction of the pressure from PIV is introduced, by implementing the Pressure Poisson equation. Lastly, the development of the Ring of Fire system up to now is elaborated upon in 3.3.

Contents

3.1 Particle Image Velocimetry (PIV)

Particle Image Velocimetry is a non-intrusive, quantitative measurement technique which is capable of visualizing the flow and correlate this visualization with aerodynamic forces. Over the past decades this measurement technique has developed to become one of the most used flow measurement methods, where a drastic improvement was made around the year 2000 through the introduction of digital cameras and digital processing. In this section, a general overview of the working principle of PIV is shown in Figure 3.1 and will be explained in the following subsections. For a more in-depth explanation of the working principles of PIV, the reader is referred to the book of Raffel et al., 2018.

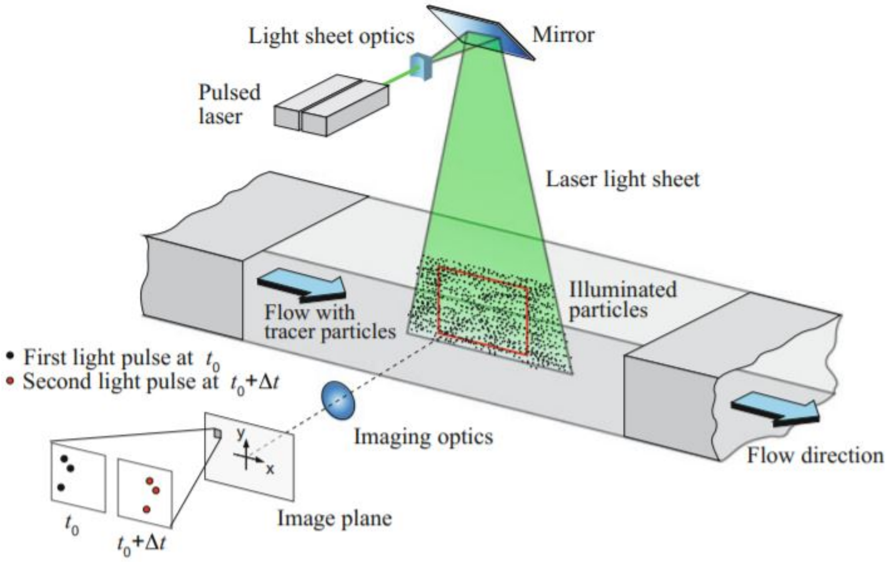

Figure 3.1: Schematic representation of a PIV setup

3.1.1 Tracer particles

To measure the displacement of air, it has to be made visible. This is achieved by injecting tracer particles in the flow, which can be seen and visualized by cameras. The particles therefore have to be reliable flow tracers (if this is not the case the flow is not accurately represented) and they have to possess good light scattering properties to make them visible on camera. A tracer's fidelity can be quantified by using the Stokes number, which is defined as the response time of a particle, τ_p over the characteristic time of the flow, τ_f. In general, this number should be as close to 0 as possible, to ensure nearly instantaneous reaction time of the tracer particles in case of the occurrence of a sudden velocity change. Since this is infeasible in practice, a difference will occur which is referred to as the slip velocity. This delay in the particle response time is expressed in Equation 3.1. This response time is the time that the particle requires to reach 63% of the fluid velocity it tries to follow.

$$\tau_p = \frac{\frac{\rho_p - \rho}{\rho} d_p^2}{18\nu} \tag{3.1}$$

In this formula, ρ_p is referred to as the tracer particle density, ρ is the air density, d_p is the tracer particle diameter and μ is the dynamic viscosity of the fluid. From this formula, it can be concluded that neutrally buoyant bubbles (where ρ_p = ρ) are beneficial for the tracing fidelity, allowing tracers to have a large diameter while maintaining a low response time. In theory, this could reduce the response time to 0, but in real experiments this is not feasible. From this formula it can also be concluded that smaller bubbles have a lower response time, which is beneficial for the tracing fidelity. However, when the bubble size decreases, the light scattering properties decrease as well. If the diameter of the tracer is larger than the wavelength of the light source used, Mie's light theory can be applied Raffel et al.,

2018. The light scattering properties depend on the ratio of refractive indices. The intensity scales with the size of the bubble as $I \propto d^2$, meaning that a larger bubble diameter implies higher intensity light scattering.

3.1.2 Illumination

The tracer particles are illuminated by means of a high intensity laser, which provides very short light pulses in the order of nanoseconds. This ensures that the tracers are visualized as dots and not as streaks in the images. Moreover, the time between light pulses should be long enough such that the particle displacement is sufficiently large to be measured but short enough such that the particles do not leave the laser sheet between pulses. Usually in PIV two images are taken shortly after each other, which is continuously repeated. However, it is also possible to have constant separation between two images, allowing for more advanced processing techniques to be applied. The laser is shaped in a sheet form using several lenses, allowing the visualization of a larger area, referred to as the field of view. The laser provides a high intensity light, which is required if the illuminated particles are to be captured by the camera. This is usually done by using Nd:YAG or Nd:YLF lasers in PIV experiments.

3.1.3 Imaging

The illuminated particles are visualized by the camera. The energy that is transmitted by the particles is converted to an electric current, allowing to assign a distinct intensity value to each pixel. The ratio of the focal length over the aperture diameter, called the f-stop or $f_{\#}$ is used to select the amount of incident light received by the camera. In typical wind tunnel experiments, fog droplets are used as tracers. Such tracers are very small particles in the order of μm, for which the diffraction diameter limits the minimum particle image diameter. Additionally, for large scale measurements, where the magnification factor becomes very low, the minimum particle image diameter is also limited by the diffraction diameter. The diffraction diameter can be calculated as follows:

$$d_{diff} = 2.44\lambda(1+M)f_{\#} \tag{3.2}$$

Where λ is the wavelength of the laser, $f_{\#}$ is the previously described f-stop and M is the magnification factor. The magnification factor is a ratio of the image distance to the lens over the object distance to the lens.

$$M = \frac{d_i}{d_o} = \frac{\text{pixel size} \cdot \text{pixel number}}{\text{Field of view}} \tag{3.3}$$

To determine the distance that the camera has to be located from the laser sheet, the focal length f is required and the thin lens equation can be used.

$$\frac{1}{f} = \frac{1}{d_i} + \frac{1}{d_o} \rightarrow d_0 = f(1+\frac{1}{M}) \tag{3.4}$$

The particle image diameter is not only dependent on the geometric optics but also on diffraction. Diffraction occurs when a light wave hits an obstruction such as the aperture of a camera, causing an interference. If the illuminated particle is a sphere, this results in a so-called "Airy disc", meaning that the particle is not visualized as a circle but rather as multiple circles around each other varying in intensity. The particle image diameter can be obtained through the Eucledian sum of the physical particle diameter and the diffraction diameter:

$$d_\tau = \sqrt{d_{geom}^2 + d_{diff}^2} \tag{3.5}$$

However, in most experiments the diffraction diameter is much larger than the physical particle diameter $d_{diff} >> d_{geom}$, therefore $d_\tau \approx d_{diff}$. For sub-pixel accuracy, the optimal particle image diameter should be about 2-3 pixels. If the particle image is smaller, peak locking may occur. This is especially noticeable for particle image diameter smaller than 1 pixel, since then the very small distances inside a pixel cannot be measured. For a more detailed explanation of peak locking, the reader is

referred to the book of Raffel et al., 2018
The f-stop also impacts the particle image diffraction, where especially for smaller particles this may be considered an advantage as this prevents peak locking due to the illumination being spread to adjacent pixels.

It should be noted that above relations can only be applied to particles in focus. The depth of focus can be changed by varying the f-stop and should be equal to or larger than the laser sheet thickness, to make sure all particles inside the laser sheet are in focus. The depth of focus is calculated according to the following equation:

$$\delta z = 4.88(\frac{M+1}{M})^2 f_{\#}^2 \lambda \tag{3.6}$$

Reviewing Equations 3.2, 3.5 and 3.6, it can be concluded that the f-stop controls two important parameters, namely the depth of field as well as the particle image diameter.

3.1.4 Cross-correlation

After the images have been acquired, they are split up in several small windows, called interrogation windows. For optimal results, at least 10 particles per interrogation window are required. Consequently, the interrogation windows of two subsequent images at the same location are cross-correlated, resulting in a cross-correlation map. The highest peak in this map should be identified, as this indicates the highest degree of matching of the intensity distribution of the two windows. The location of this cross-correlation peak determines the average particle displacement. Subsequently, to each interrogation window is assigned the average particle displacement of the particles inside that window. A Gaussian fit interpolation scheme can be used for determining the correlation peak at sub-pixel accuracy. Finally, with the known time separation between the images and the calculated displacement, the particle velocity can be determined.

When using time-resolved PIV, cross-correlation is performed for consecutive images, which are then combined to create velocity fields. In contrast to standard PIV where one pair of images creates one correlation map, each individual image contributes to two correlation maps. Each image creates one correlation map with the previous image, and one correlation with the following image. This allows for a constant time separation between all images, but has as a downside that if an image is erroneous, it affects two velocity fields instead of just one. Recently, the sliding sum-of-correlation algorithm and the pyramid algorithm have been developed in PIV Sciacchitano et al., 2012. These algorithms aim at increasing the accuracy and stability of the velocity fields. The working principle of time-resolved pyramid algorithm is displayed in Figure 3.2. It should be noted that the sliding sum-of-correlation algorithm is the same as the pyramid algorithm for n=1.

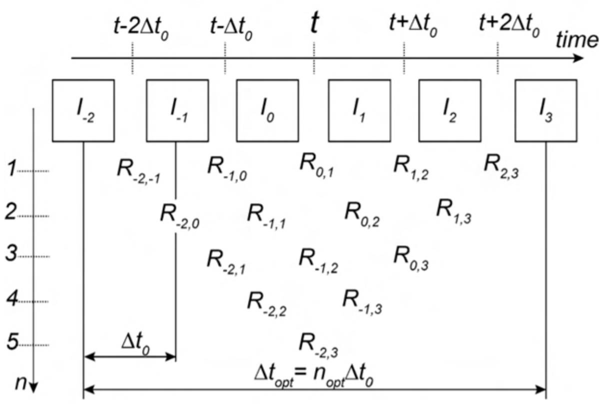

Figure 3.2: Working principle of the pyramid correlation algorithm for time-resolved PIV

All correlation maps within a certain range from a given image are added up. This range is indicated by the filter length, L. These images are Gaussian weighted, meaning that correlation maps at a further distance from the selected image have less influence on the final velocity field. This approach results in an increased stability due to the sum of correlation. Moreover, the created velocity fields show a continuous development of the flow over time, which is especially beneficial for highly dynamic flows, such as the turbulent flow in the wake of a car. The main disadvantage of this method is that it is relatively time consuming and computationally expensive compared to the standard PIV evaluation methods.

In the pyramid correlation function Sciacchitano et al., 2012, not only all correlation maps are combined of each different image pair, but additional correlation maps are created between images with a larger time interval, between Δt_0 and Δt_{opt}, where Δt_{opt} is the optimal time separation for the most reliable results. An additional homopethy correction is then performed to take the different Δt into account in order to combine all correlation maps. These images are Gaussian weighted, meaning that correlation maps at a further distance from the selected image have less influence on the final velocity field. This approach results in an increased stability due to the sum of correlation. Moreover, the created velocity fields show a continuous development of the flow over time, which is especially beneficial for highly dynamic flows, such as the turbulent flow in the wake of a car. The main disadvantage of this method is that it is relatively time consuming and computationally expensive compared to the standard PIV evaluation methods. Namely, the simulation time using the pyramid correlation increases exponentially with the number of time steps n, whereas the time for the sliding sum of correlation algorithm increases linearly with n. For this project, it is assumed that the sliding sum is sufficiently accurate, since large scale structures are aimed to be resolved and the improved accuracy of the pyramid algorithm does not outweigh the huge simulation time increase.

3.1.5 Stereoscopic PIV

When PIV research is conducted using one camera, the flow can only be described in two dimensions. This is for example used in wind tunnels, where the aerodynamic characteristics of a (assumed) two-dimensional flow over an airfoil are investigated. However, when the flow is not two-dimensional, perspective errors occur due to the out-of-plane component and the velocity fields become unreliable. Therefore, two-component PIV (planar PIV) is not recommended for analysing dynamic three-dimensional flows. When a second camera is employed with varying angle towards the field of view, the third velocity component can be calculated as well since the particles are recorded from different perspectives and the perspective error is eliminated. In case of two cameras, this technique is called 2D-3C (two-dimensional, three-component) stereoscopic PIV and the resulting velocity components are only calculated in a sheet. When more than 2 cameras are used, the third dimension is integrated as well and the technique becomes 3D-3C tomographic PIV Scarano, 2012, which allows for measurements inside a volume rather than a sheet.

The most commonly used stereoscopic measurement technique is the angular method. This method is shown in Figure 3.3:

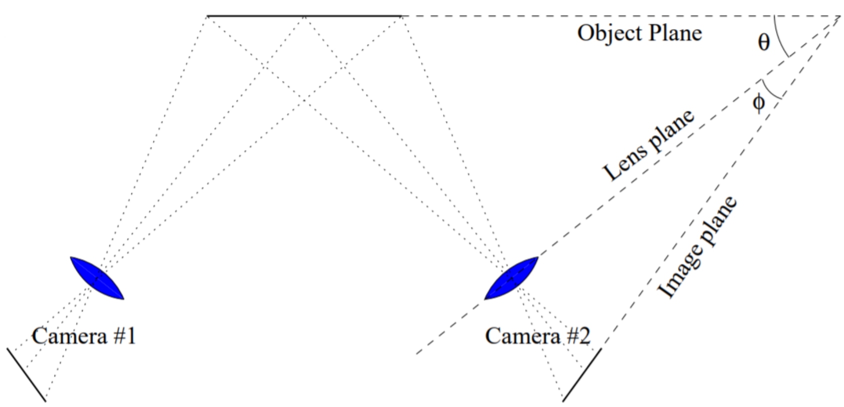

Figure 3.3: The angular stereoscopic PIV method Raffel et al., 2018

The angular stereo-PIV allows for a large off-axis angle θ, meaning that the lenses can perform at the centre of their optical specification, resulting in optimal performance. The larger off-axis angle increases the accuracy of the out-of-plane component. However, increasing the off-axis angle results in a more non-uniform magnification factor. This compromises the in-plane accuracy. When the angle is $45°$, the out-of-plane and in-plane accuracy are equal so therefore Prasad, 2000 suggest this angle for optimal accuracy.
As shown in Figure 3.3, the image plane has to be rotated by an additional angle ϕ in order to be collinear with the lens plane and object plane. This requirement, known as the Scheimpflug condition, ensures that all particles in the field of view are in focus. The Scheimpflug condition however creates an even more non-uniform magnification, resulting in a larger in-plane uncertainty. Usually a Scheimpflug adapter is attached to the camera, such that the lens plane can be moved with respect to the image plane.
Next to the non-uniformity, the rotation of the cameras also creates a distortion when the two images are mapped onto the object plane, resulting in a loss of field of view. This effect is shown in Figure 3.4:

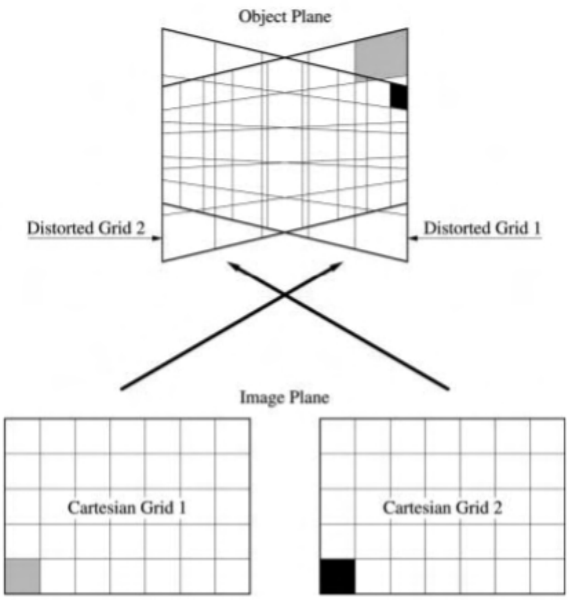

Figure 3.4: Distortion in the dewarped image due to the rotation of the image and lens plane Prasad, 2000

This distortion has to be corrected for using a mapping function. The images from each camera are then changed accordingly. A common technique implements a pinhole calibration plate to map the 3D object position onto the 2D image plane by means of a pinhole calibration plate. This calibration plate is nearly the same size of the field of view and has pinholes at two levels of depth, distributed in rows of equal spacing in horizontal and vertical direction. Mapping functions introduced by Willert, 1997 can be used, which require at least 6 calibration points, resulting in a solution for the twelve coefficients in the second-order mapping function using a least-squares approach. Wieneke, 2005 proposes a mapping function which further reduces the calibration error. This is based on creating a disparity map of the velocity vectors of approximately 50 images by implementing ensemble-average cross-correlation. This development meant that stereo-PIV could even be conducted when the calibration plate would be slightly misaligned with the laser sheet, since this function corrects that error.

Using the aforementioned correction methods, the actual velocities can be calculated as shown in Figure 3.5:
From this image it is clear that α represents the angle between the out-of-plane axis (z) and the object plane axis (x) as shown in the Figure and β (which is not shown) is the angle between the out-of-plane axis and object plane axis in the side view. The velocity components can be reconstructed accordingly and are defined as follows:

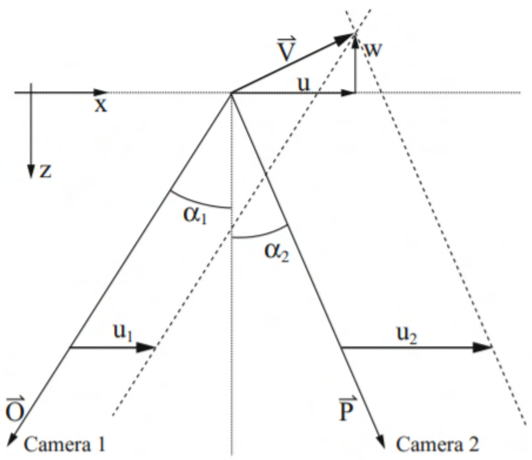

Figure 3.5: Out-of-plane velocity component construction Raffel et al., 2018

$$u = \frac{u_1 tan\alpha_2 + u_2 tan\alpha_1}{tan\alpha_1 + tan\alpha_2} \quad (3.7)$$

$$v = \frac{v_1 tan\beta_2 + v_2 tan\beta_1}{tan\beta_1 + tan\beta_2} \quad (3.8)$$

$$w = \frac{u_1 - u_2}{tan\alpha_1 + tan\alpha_2} = \frac{v_1 - v_2}{tan\beta_1 + tan\beta_2} \quad (3.9)$$

3.1.6 Large-scale PIV

The main limitation to enable large-scale PIV with measurement domains up to several meters, is the detectability of the traditional micron-sized tracer particles. As increasing the size of these particles influences the tracing fidelity too much, particles need to be investigated for which the density approaches the density of the working fluid. For this reason, Bosbach et al., 2008 investigated the feasibility of Helium-Filled Soap Bubbles (HFSB) in PIV. Naturally buoyant helium filled soap bubbles were investigated because of their very high light scattering efficiency, also in the backwards direction. Moreover, the size of the bubbles is easily adjustable by changing the operation parameters or changing the orifice diameter. Using Nd:YAG lasers, their standard large size between 2 and 7 mm could be reduced to sub-millimeter size. Due to their neutral buoyancy characteristics (helium is lighter than air, soap is heavier and by having the correct ratio the density can be easily adjusted) relatively large bubbles can be used compared to standard PIV size bubbles (HFSB with a size of up to 400 μm can be used compared to standard bubbles with a size of several μm). This greatly improves the light scattering properties and therefore could be the solution to increase the scale that PIV can be applied to.

Following the research conducted by Bosbach et al, Kühn et al Kühn et al., 2011 conducted a research in 2011, where they analysed the feasibility of helium-filled soap bubbles by looking at the final calibration error. In their experiment, a FOV of 750 mm x 450 mm x 165 mm was established and the calibration error was in the order of 0.1 pixels, as is required. Moreover, they concluded that the optical characteristics of the helium-filled soap bubbles had no influence on the measurement accuracy. A comparison of the mean velocity of the tomographic PIV set-up with the mean velocity of planar PIV data, the difference is less than $|\Delta v|$ = 0.005 m/s. Elsinga et al., 2006b showed very comparable results, showing the good agreement between the small-scale and large-scale experiments. Therefore, the authors conclude that HFSB do not significantly influence the measurement accuracy in such PIV measurements.

In 2015, the study in the use of helium-filled soap bubbles in tomographic PIV was continued by Scarano et al., 2015. The flow-tracing fidelity of sub-millimetre diameter helium-filled soap bubbles was analysed by injecting HFSB in the stagnating flow ahead of a circular cylinder of 25 mm diameter, for which the test setup is shown in Figure 3.6a. The flow velocity was increased up to 30 m/s. Using particle tracking velocimetry, the soap bubbles could be followed in the flow. By analysing the characteristic time response, resulting from the acceleration and slip velocity measurements, the feasibility of HFSB could be analysed. This is done by comparing this characteristic time response with fog droplets as reference. Different helium flow rates were tested and compared to fog droplets, which acted as a reference. At certain rates (4 and 5 ml/h) of helium injection, barely any differences could be noticed between the helium bubbles and the fog, as shown in Figure 3.6b. A lower or a higher injection rate resulted in either a floating behaviour or a delayed response, respectively. The main difference with earlier experiments is the significant decrease in bubble size (300 microns versus several millimeters) and no need of pre-filtering of negatively buoyant particles.

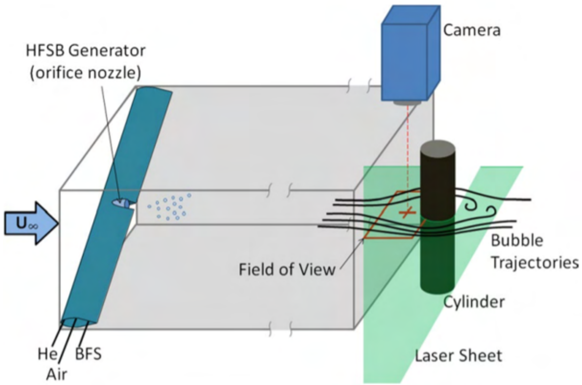

(a) Test setup, replicated from Scarano et al., 2015

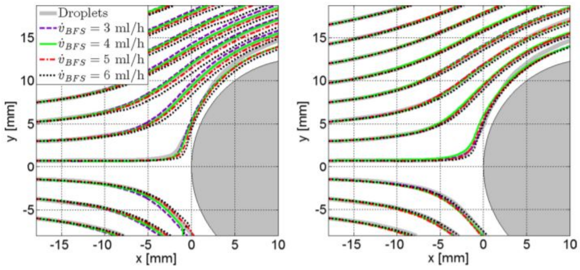

(b) Time-averaged streamlines of the helium filled soap bubbles compared to micron-sized fog droplets Scarano et al., 2015. Left: helium rate of 4 l/h. Right: helium rate of 5 l/h

Figure 3.6: Experiment conducted by Scarano et al., 2015

Another limitation to using large-scale particle image velocimetry was the limited number of seeding particles that could be generated in the flow by current seeding generators. Therefore, a significant improvement in seeding generator was required. In the experiment, a dedicated piston-cylinder device was used with which a higher seeding concentration using helium-filled soap bubbles of several orders of magnitude could be achieved. Using the standard tomo-PIV analysis with spatial cross-correlation, the instantaneous flow field and resulting large-scale flow structures such as the Kármán vortex structure in the wake of a cylinder could be resolved. Smaller turbulent substructures could not be resolved. The limiting factor for the spatial resolution is the low concentration of tracers. Since a significant improvement in seeding generation was established, the long awaited large-scale particle image velocimetry became a viable option for aerodynamic research.

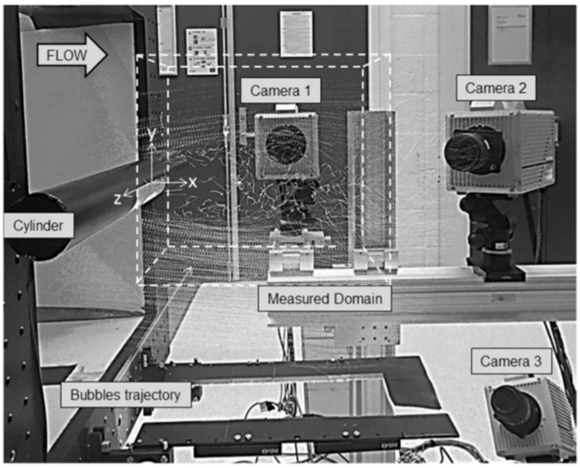

(a) Test setup, replicated from Scarano et al., 2015

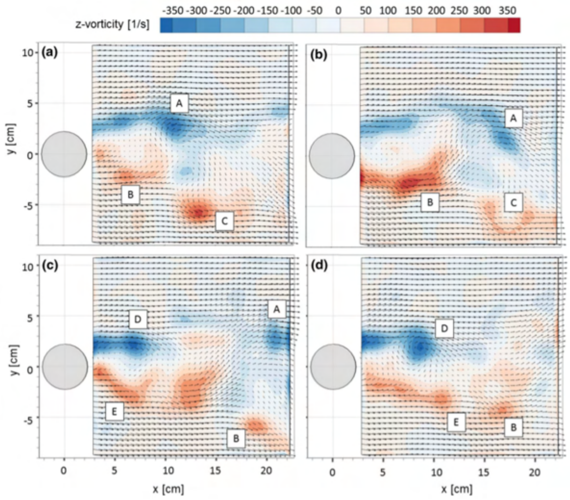

(b) Vorticity, replicated from Scarano et al., 2015

Figure 3.7: Experiment conducted by Scarano et al., 2015

Following these developments, Jux et al., 2018 implemented HFSB and the improved seeding generator to conduct robotic volumetric PIV of a full-scale cyclist in a measurement domain of approximately 2m^3. The research concluded that the flow topology corresponds well to literature and an uncertainty of the mean velocity is reported in the order of 4% in z-direction and 2% in x- and y-direction. The experimental set-up is shown in Figure 3.8a and the vorticity is shown in Figure 3.8b.

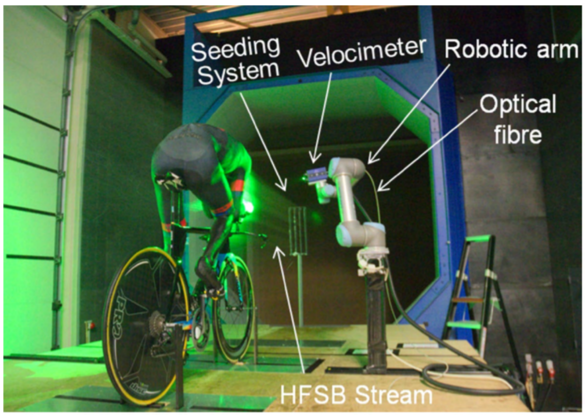

(a) Test setup, replicated from Jux et al., 2018

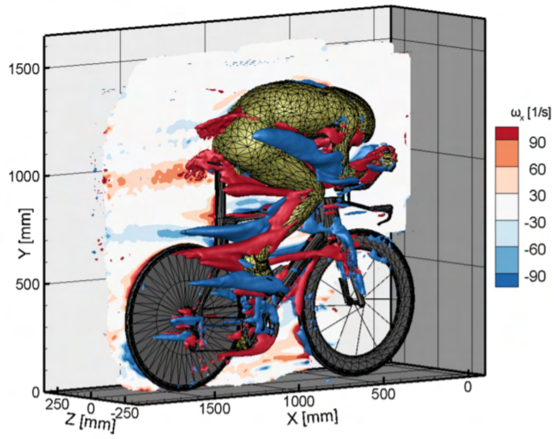

(b) Vorticity, replicated from Jux et al., 2018

Figure 3.8: Experiment conducted by Jux et al., 2018

3.2 Control volume approach

One of the benefits from stereoscopic PIV is that the drag can be calculated using the velocities in the flow field, which allows one to correlate the flow field properties to the drag value. The approach used in this thesis implements conservation of mass and using the momentum integral equation to determine the drag in a control volume, as described by Anderson, 2017. In the Ring of Fire, the control volume is considered to be part of a stream tube where the upper surface and side surfaces of the stream tube are streamlines. The ground is considered to be an impermeable surface, which leaves only the inlet and outlet plane where mass flow enters and leaves the control volume. A schematic representation of such a control volume is provided in Figure 3.9.

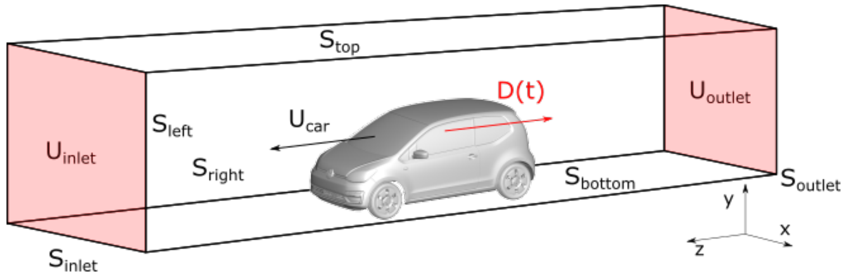

Figure 3.9: Control volume around a car

3.2.1 Momentum integration in the wind tunnel reference frame

Starting from the momentum integral equation and applying it to a stream tube where only the inlet and outlet plane allow mass flow and momentum exchange, the drag can be determined for incompressible flow. In aerodynamic research, wind tunnel measurements are commonly used where the fluid is moving at a certain constant velocity u_∞, replicating the velocity of the object in real life. The coordinate system is stationary and inertial with the test object. The drag can then be calculated according to Equation 3.10 Mohebbian and Rival, 2012:

$$D(t) = -\rho \iiint_V \frac{\partial \mathbf{u}}{\partial t} dV - \rho \iint_S \mathbf{u}(\mathbf{u} \cdot \mathbf{n}) dS - \iint_S p\mathbf{n} dS + \iint_S (\bar{\bar{\tau}} \cdot \mathbf{n}) dS \tag{3.10}$$

Where $D(t)$ represents the drag, ρ is the density, V is the control volume, t is the time, u is the z-component of the fluid velocity, n is the normal vector to the control surface which bounds the control volume, S is the control surface, p the fluid static pressure and τ is the stress tensor. The first term indicates that volumetric velocity measurements are required to calculate the drag. To avoid the need for such measurements and keep the measurements over the control surface, this term has been reformulated by Wu et al., 2005, leading to Equation 3.11:

$$D(t) = -\rho \frac{\partial}{\partial t} \iint_S z(\mathbf{u} \cdot \mathbf{n}) dS - \rho \iint_S \mathbf{u}(\mathbf{u} \cdot \mathbf{n}) dS - \iint_S (p - p_\infty) \mathbf{n} dS + \iint_S (\bar{\bar{\tau}} \cdot \mathbf{n}) dS \tag{3.11}$$

Where z is the distance of the object to a fixed reference frame.
The first term in Equation 3.11 is the unsteady term, the second term is the momentum term, the third term is the pressure term and the last term is the viscous term. In order to use this equation with large scale stereo-PIV, several assumptions and simplifications will be made.

- **Unsteady term**: the unsteady term due to the rolling of the wheels and the general motion of the object itself is assumed to be negligible, which is in line with previous Ring of Fire experiments where the rolling of the cycle wheels and the pedalling of the cyclists were neglected as well Spoelstra, 2017 de Martino Norante, 2018 Hirsch, 2018 Mahalingesh, 2020.
- **Momemtum term**: this term is defined as the product of the velocity with the mass flow across the control surfaces. As stated before, the left, right and top surfaces are assumed to be streamlines and the ground prevents a mass flow through this surface as well. Therefore, $\mathbf{u} \cdot \mathbf{n} = 0$ for these surfaces, leading to the momentum term being solely dependent on the choice of the inlet and outlet plane. This term can thus be split up in a term regarding the inlet plane and a term regarding the outlet plane.
- **Pressure term**: if the left, right and top surface are chosen sufficiently far away from the test object, the pressure has recovered to the environmental or freestream conditions and there is no force due to pressure differences here. Even in the case where these surfaces are still close to the body, the pressure term would act normal to the surface and therefore have a negligible effect on the drag force, which is aligned with these surfaces and not perpendicular. When the inlet and outlet surface are chosen sufficiently far away, i.e. more than 5 characteristic lengths (based on a towed sphere experiment) this term can be neglected according to Terra et al., 2017.

- **Viscous term**: the viscous term is the integral over the control surface of the stress tensor normal to this surface. Since the control surfaces are chosen sufficiently far from the tested object, the viscous term can be neglected. Moreover, if the inlet and outlet plane are consequently chosen sufficiently far away, the viscous stress over the surface of the object can also be neglected according to Kurtulus et al., 2007 and Mohebbian and Rival, 2012.

This leaves the following equation for the drag of a test object through the use of the momentum integration in a control volume:

$$D(t) = \rho \iint_{S_{inlet}} u_{inlet}^2 dS - \rho \iint_{S_{outlet}} u_{outlet}^2 dS + \iint_{S_{inlet}} p_{inlet} dS - \iint_{S_{outlet}} p_{outlet} dS \tag{3.12}$$

Where S_{inlet} is the inlet plane, S_{oulet} is the outlet plane, u_{inlet} is the velocity at the inlet plane which is equal to the freestream velocity u_∞ in a wind tunnel, u_{oulet} is the velocity at the outlet plane which is equal to the wake velocity u_{wake}, p_{inlet} is static pressure at the inlet plane, and p_{outlet} is the static pressure at the outlet plane.

3.2.2 Momentum integration in the Ring of Fire reference system

The control volume has been established in the aforementioned paragraphs but cannot yet be directly applied to the Ring of Fire measurement system. The above derivation assumes a reference system that is inertial and moving with the tested object (which is the passenger car in this project) and assumes a constant fluid velocity where the test object does not move itself. However, in the Ring of Fire method the reference system is stationary located at the light sheet and the car moves relative to the reference system. The inlet plane is considered to be the upstream plane before the transit of the car and the outlet plane is the downstream plane after transit. To apply the above derivation, the control volume is considered to move with the same velocity as the car, fixing the car at a location in the control volume. To do this, a Galilean transformation is performed, changing the reference frame from stationary to one moving at the car velocity. Hence, the car velocity is subtracted from the measured velocity at the inlet and outlet plane, where the measured inlet plane velocity consists of environmental fluctuations and the measured outlet plane velocity of the velocity in the wake of the car. A schematic representation of the stationary reference frame is shown in Figure 3.10a and after the Galilean transformation is shown in Figure 3.10b.

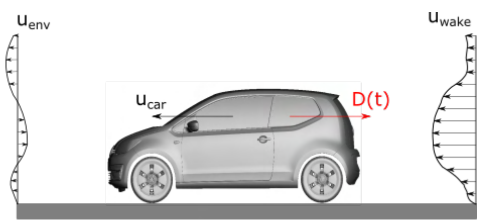

(a) Velocity distribution before and after transit of the car

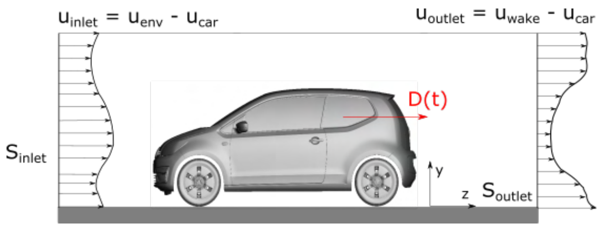

(b) Velocity distribution after Galilean transformation

Figure 3.10: Galilean transformation from static frame of reference to moving frame of reference, based on the figures provided by Spoelstra et al., 2019

In Equation 3.13 the result is shown which holds for the Ring of Fire, where u_{env} corresponds to the environmental fluctuations before the passage of the car:

$$D(t) = \rho \iint_{S_{inlet}} (u_{env} - u_{car})^2 dS - \rho \iint_{S_{outlet}} (u_{wake} - u_{car})^2 dS + \iint_{S_{inlet}} p_{inlet} dS - \iint_{S_{outlet}} p_{outlet} dS \tag{3.13}$$

To ensure that no additional mass flows enters or leaves the control volume and thereby increasing or decreasing the momentum deficit, conservation of mass is invoked as a requirement for the momentum integration. Since the velocity at the inlet plane is higher than the wake velocity, the inlet plane has to be smaller than the outlet plane and is shaped according to the size of the wake behind the car. The conservation of mass thus implies the following restriction:

$$\rho \iint_{S_{inlet}} (u_{env} - u_{car}) dS = \rho \iint_{S_{outlet}} (u_{wake} - u_{car}) dS \tag{3.14}$$

The drag is made non-dimensional with the dynamic pressure, which is expressed in Equation 3.15. It should be noted that for the dynamic pressure the freestream velocity is substituted by the relative motion of the car with respect to the environmental velocity, which is calculated by averaging multiple planes far before the car enters the light sheet.

$$CdA = \frac{D(t)}{\frac{1}{2}\rho(\overline{u_{env}} - u_{car})^2} \tag{3.15}$$

Where A is the frontal area of the car.
It should be noted that this equation is used to calculate instantaneous drag values. Usually in wind tunnel experiments the time-averaged velocity fields are of interest, to analyse the typical flow fields without fluctuations and get an understanding of the average flow structures. To get a proper understanding of the main flow structures in the wake of the car, velocity fields at specified distances behind the car from multiple passages are ensemble averaged.

$$CdA_{avg} = \overline{CdA} \tag{3.16}$$

3.2.3 Pressure from PIV

In theory, the outlet plane in the control volume can be chosen sufficiently far away such that the pressure has recovered to the environmental static pressure and there is no need to calculate the in-plane static pressure. However, if the measurement plane is located too close to the car the pressure significantly contributes to the drag and consequently the need for pressure calculations arises. Moreover, plotting the static pressure may prove useful in analysing the flow fields in the wake of the car. Therefore, an attempt to calculate the static in-plane pressure will also be made in this thesis. As implemented before by de Martino Norante, 2018, one of the methods to calculate this pressure is by implementing the Pressure Poisson equation at the planes in the wake van Oudheusden, 2013. PIV provides the velocity fields which are used to calculate the velocity derivatives required for the Pressure Poisson equation.

The Pressure Poisson equation results from taking the divergence from the momentum equation. To start, the momentum equation is provided in Equation 3.17:

$$\nabla p = -\rho \frac{D\mathbf{u}}{Dt} + \mu \nabla^2 \mathbf{u} \tag{3.17}$$

Where $\mathbf{u}$ is the instantaneous velocity, p is the instantaneous pressure and where the fluid density ρ and fluid viscosity μ are known values. The material acceleration described by $\frac{D\mathbf{u}}{Dt}$ can be rewritten from a Eulerian perspective:

$$\frac{D\mathbf{u}}{Dt} = \frac{\partial \mathbf{u}}{\partial t} + (\mathbf{u} \cdot \nabla)\mathbf{u} \tag{3.18}$$

To compute the pressure field, the divergence is taken from Equation 3.17:

$$\nabla \cdot (\nabla p) = \nabla \cdot (-\rho \frac{D\mathbf{u}}{Dt} + \mu \nabla^2 \mathbf{u}) \tag{3.19}$$

Substituting Equation 3.18 in Equation 3.19 and using the fact that the flow can be assumed to be incompressible due to the low speed aerodynamics regime (meaning that the flow is divergence free: $\nabla \cdot \mathbf{u} = 0$) results in the following expression:

$$\nabla^2 p = -\rho \nabla \cdot (\mathbf{u} \cdot \nabla)\mathbf{u} \tag{3.20}$$

Equation 3.20 implies that spatial derivatives are needed to compute the pressure field. Even though stereoscopic PIV provides the out-of-plane velocity component, it is impossible to determine the

out-of-plane velocity gradient. Only the velocity gradients of the in-plane velocity components can be calculated.
Nonetheless, Kat and Ganapathisubramani, 2013 suggest an improvement in the Eulerian approach for the determination of the out-of-plane velocity gradient by means of mapping the velocity evolution from temporal to space. This is done by implementing Taylor's hypothesis in the cross-plane time-resolved stereoscopic PIV results, calculated with Equation 3.21:

$$\frac{\partial u'}{\partial x} = -\frac{1}{u_c}\frac{\partial u'}{\partial t} \tag{3.21}$$

It should be noted however, that this technique requires a high temporal resolution. Moreover, it is assumed that the in-plane velocities are negligible with respect to the out-of-plane velocity, which is not the case for the wake of the car, where the in-plane velocities cannot be neglected. Therefore, using this equation would likely introduce more erroneous results than if the out-of-plane velocity gradient would be ignored, which is in line with previous Ring of Fire experiments (de Martino Norante, 2018, Mahalingesh, 2020).

As a result, for this Ring of Fire project the flow is assumed to be 'sufficiently' 2D, such that the 2D Pressure Poisson equation can be used and the out-of-plane velocity gradient is neglected. Rewriting Equation 3.20 in Cartesian form shows that the pressure gradient can be calculated from the in-plane velocity and acceleration van Oudheusden, 2013:

$$\frac{\partial^2 p}{\partial x^2} + \frac{\partial^2 p}{\partial y^2} = \rho\left\{(\frac{\partial u}{\partial x})^2 + 2\frac{\partial v}{\partial x}\frac{\partial u}{\partial y} + (\frac{\partial v}{\partial y})^2\right\} \tag{3.22}$$

Equation 3.22 is a partial differential equation and requires 4 boundary conditions in order to be solvable. Since the boundaries of the stereo PIV velocity fields are represented by the boundaries of a streamtube, Neumann boundary conditions are suitable options for each side, since it was already established that there is no mass flow across the boundaries. This implies that the pressure field is solved up to a constant, for which the freestream pressure is taken to scale the pressure field to the conditions during the experiment. This procedure replicates the process introduced by Terra et al., 2017 and de Martino Norante, 2018. In Chapter 5, the selection of the boundary conditions is visualised.

3.3 The Ring of Fire

3.3.1 Early development

As a result of the development of helium-filled soap bubbles as feasible seeding particles for large scale particle image velocimetry, Sciacchitano et al., 2015 introduce a new quantitative flow visualisation technique for on-site aerodynamics optimization. In this paper, a newly developed, on-site qualitative and quantitative measurement system is introduced, as current state-of-the-art measurement techniques only include wind tunnel measurements (using balances or pressure sensors) and CFD simulations. This on-site measurement system, called the "Ring of Fire", is based on large-scale tomographic PIV in a volume exceeding 10,000 cm^3, using helium-filled soap bubbles as flow tracers. With this technique, a non-intrusive way of calculating the pressure field and forces acting on a transiting object is developed, omitting the need for intrusive pressure probes or sensors. An on-site visualization of the flow can be generated and thereby contributes to the understanding of the typical turbulent flow structures behind bluff bodies, such as cyclists, ice-skaters and cars. With this on-site technique, dynamic motions are naturally measurable without the need for difficult moving ground simulations in a wind tunnel or CFD, the variables in the flow field are supported by both instantaneous and time-averaged drag calculations and it is much easier to perform drafting configurations or movements during corners. The feasibility of the HFSB was shown in an experiment where the flow over a vertical-axis wind turbine was measured and analysed. The test setup and the vorticity with in-plane vector fields are shown in Figure 3.11.

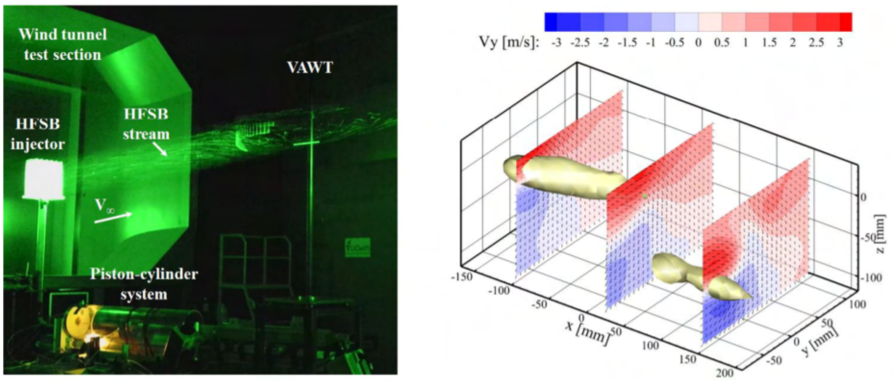

Figure 3.11: VAWT experiment by Sciacchitano et al., 2015. Left: test setup. Right: in-plane velocity with vorticity isosurfaces

Terra et al., 2017, a Ring of Fire proof of concept study was performed researching the feasibility of the use of helium filled soap bubbles for transiting objects. In this specific paper the flow around a sphere was investigated. A viability analysis is performed on the drag estimation of such object through the momentum conservation application in tomographic particle image velocimetry.
Time-resolved tomo-PIV measurements are conducted using neutrally buoyant, 300 micrometer sized helium-filled soap bubbles. The tunnel entrance and exit are closed before the experiment while the soap bubbles are generated, to ensure the proper distribution inside the testing domain for the experiment. The sphere passes through the tunnel and images are taken. The streaklines are taken by averaging 10 frames. The test setup and the velocity results are shown in Figure 3.12a and 3.12b

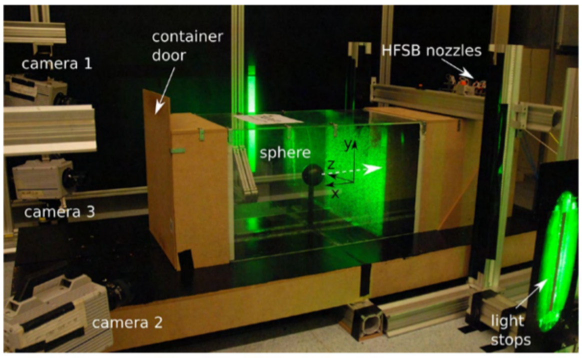

(a) Test setup, replicated from Terra et al., 2017

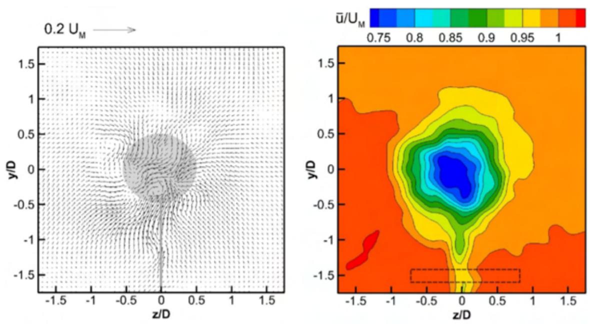

(b) In-plane velocity vectors and out-of-plane velocity contour, replicated from Terra et al., 2017

Figure 3.12: Experiment conducted by Terra et al., 2017

From this study it is found that after 5 diameters behind the cylinder, the pressure term vanishes. This implies a great practical use for the measurement procedure for ground vehicles and passenger cars in particular, meaning that it can be assumed that 5 car lengths behind the car the pressure term likely vanishes as well. Also, despite the simple geometry, the vortex structures behind the sphere are representative of the vortex structures behind a bluff body or ground vehicle, such as the Ahmed body.

In a later research, Terra et al., 2018 aim to evaluate the accuracy of the "PIV wake rake" method. Measurements are performed on a sphere, which is towed at different speeds. Being able to measure the flow field before passage of the light sheet and after passage is critical in the ability to accurately estimate the drag for such models. The measurements could be conducted where the drag resolution was approximately 20 drag counts. This result is coarser than in usual wind tunnel tests, but comparable to on-site techniques for field measurements. The results consisted of an instantaneous and mean aerodynamic load. The authors noted that the environment that the towed object enters may not be completely stagnant, for which in this study the helium filled soap bubbles were the cause, as these introduced a motion in the flow. If this is not accounted for during the momentum conservation approach to calculate the aerodynamic loads, the quadratic behaviour with respect to the velocity is not established.

However, when this initial velocity is taken into account, a good agreement with the theoretical quadratic velocity scaling is observed.

3.3.2 Research with the Ring of Fire

After the early development and research into the potential of large-scale particle image velocimetry for transiting objects, the first Ring of Fire research was conducted by Spoelstra, 2017. In this research, the feasibility of the Ring of Fire as a quantitative flow visualisation technique for transiting cyclists was investigated, as well as testing the accuracy of the system by comparing to measurements at a scaled test set up. The main experiment consisted of implementing the Ring of Fire on a real cyclist outdoors, where a schematic overview is presented in Figure 3.13a and the actual setup shown in Figure 3.13b. This implied a torso based Reynolds number of $3.17x10^5$. The results showed comparable flow structures in the wake of the cyclist when compared to flow structures found in literature. Also, vorticity plots indicated the inner hip vortices and shoulder vortices which are also found in literature when testing in wind tunnels. However, a large difference was found when comparing the wake below the pedals, i.e. the lower 15 cm of the wake. For the Ring of Fire, the wake contour was rounded there whereas for wind tunnel tests without a moving ground showed an extension towards the ground, increasing the overall wake area. The drag area calculations where performed by implementing the momentum integration in a control volume, leading to a deviation from the literature of 10%. Nonetheless, the uncertainty of these values was only 5%.

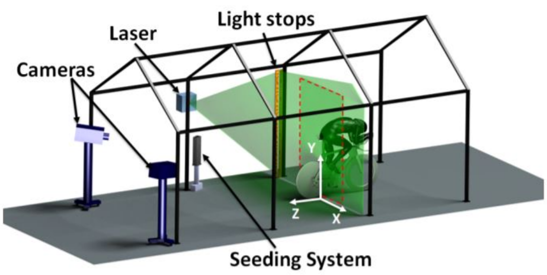

(a) Schematic view of the Ring of Fire conducted by Spoelstra in 2017 Spoelstra, 2017

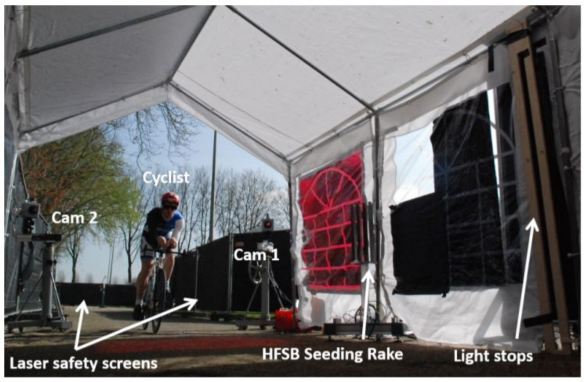

(b) Ring of Fire set-up for the experiment by Spoelstra Spoelstra, 2017

After this first research, the development of the Ring of Fire system for cyclists was continued by de Martino Norante, 2018. He hypothesised that an indoor Ring of Fire experiment using low speed cameras in the PIV set-up would increase the accuracy of the drag measurements. Also, the much shorter upload time of the data during measurements (5-10 minutes for high speed compared to an order of seconds upload time for the low speed) implies a more practical and interesting approach when only statistical data for the drag evaluation is required. Additionally, a new tunnel was implemented, which was designed to have a larger width since the wake tends to spread out laterally with increasing distance behind the cyclists.

When comparing the dynamic spatial range and the dynamic velocity range between the low speed system and the high speed system, de Martino Norante de Martino Norante, 2018 reported a DVR of 250 and DSR of 25, compared to the previously found DVR of 100 and DSR of 60 by Spoelstra, 2017. It should be noted that the experiment by Spoelstra was conducted outdoors, whereas de Martino Norante conducted his experiment indoors, leading to smaller environmental fluctuations in the seeding concentration and measurement set-up. The resulting drag calculations for the low speed experiment were found to be in line with literature, having an uncertainty of 2% for the mean drag values at a 95% confidence interval.

For the velocity fields, the following comparison was made, where on the left the low speed Ring of Fire results are shown and on the right the high speed Ring of Fire results are shown in Figure 3.14:

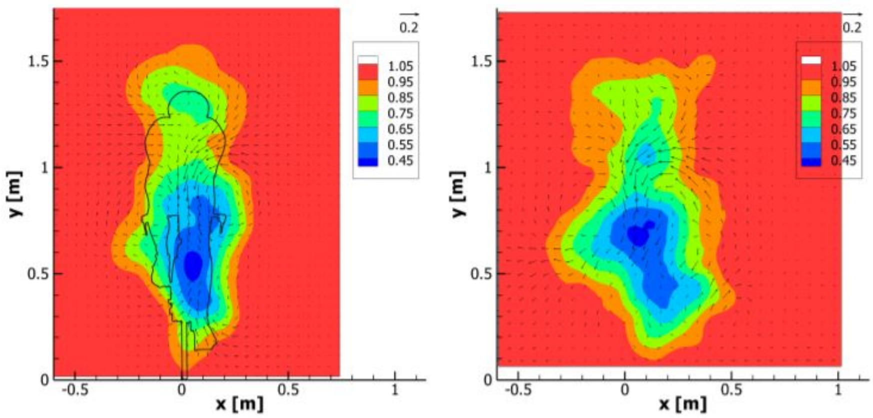

Figure 3.14: Comparison of low speed vs high speed Ring of Fire de Martino Norante, 2018

A difference in the width of the wake was visualised, which de Martino Norante contributed to the fact that the high speed measurements were performed at twice the reduced pedalling frequency, as well as to the higher turbulence and thus fluctuations in the outdoor measurements.

Where the study of de Martino Norante ended in June 2018, the research in the application of the Ring of Fire system for cyclists continued in the same year Hirsch, 2018. An indoor Ring of Fire experiment was set up to assess the accuracy of the Ring of Fire measurement system and its correlation with power meter measurements. Several configurations from changing helmets to changing posture were tested.
Regarding the drag area coefficients, good agreement with literature was found, within 5% of the Ring of Fire results. Also, the Ring of Fire was demonstrated to be a feasible option for assessing long distance drafting between two cyclists (7-9m from front wheel to front wheel), resulting in a 15% lower drag area coefficient for the trailing cyclist.
In a later published report, Spoelstra et al., 2020 analysed the uncertainty, where the results of the thesis report by Hirsch, 2018 were used. In this report, it was concluded that the drag area coefficient is dependent on the conservation of mass and thus the contouring of the inlet and outlet plane in the conservation of momentum approach. Moreover, the interrogation window size used during the processing of the data is of negligible influence on the drag coefficient, as long as this size is within 5% to 25% of the torso width of the cyclists, thus in general of the equivalent diameter of the respective cross-section of the object. The Ring of Fire drag area coefficients deviated up to 20% from the simultaneously acquired power meter drag area coefficients. This is shown in Figure 3.15, where these values are shown with bars indicating the 95% confidence interval.

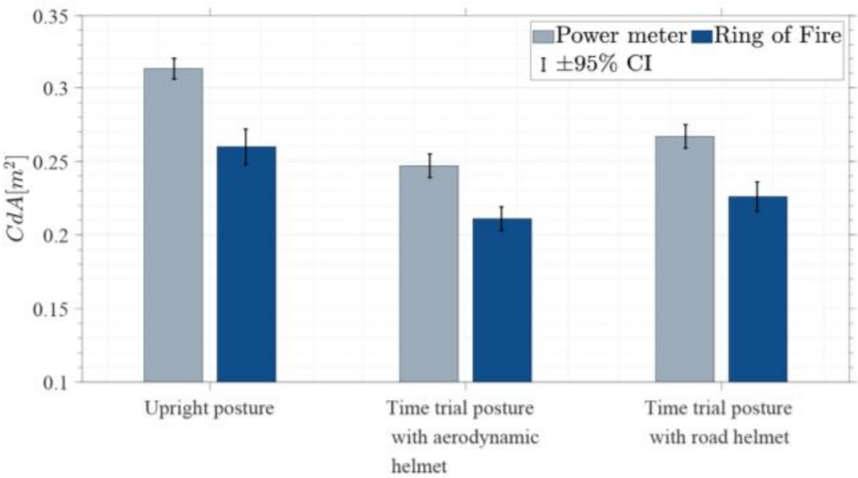

Figure 3.15: Comparison of the Ring of Fire CdA values with power meter CdA values

The authors noted that this is most likely the result of systematic errors in the Ring of Fire setup, as well as systematic errors in the simplified power meter model used (e.g. assumed rolling resistance coefficients). This reasoning is underlined by the relative results, since the difference between the upright and time-trial position for the power meter measurements is reported to be 27% compared to relative difference calculated through the the Ring of Fire of 23%. Moreover, a small delta was also investigated between different helmets, resulting in an 8% difference for the power meter measurements compared to 7% for the Ring of Fire measurements.

The most recent Ring of Fire research was conducted by Mahalingesh, 2020, which ended in early 2020. During this project, the aerodynamics of drafting cyclists using the Ring of Fire system in an outdoor experiment was assessed. In addition to previous Ring of Fire projects, also the planar pressure fields in the near-wake of the cyclists were constructed, as these are required to determine the drag of the two or more closely drafting cyclists. For this, the 2D pressure Poisson equation was implemented. Individual cyclists as well as drafting cyclists were tested, where a feasibility challenge was imposed for optical access with the cameras for drafting cyclists. The measurements for 3 different individual cyclists (named small, medium and large) agreed well with literature and the uncertainty of the mean values were reported to be 5.6%, 2.3% and 2.4% for the small, medium and large cyclist, respectively. The higher uncertainty of 5.6% was attributed to the limited number of good runs that could be used for the analysis, large variation in wind and different helmet positions. Based on the uncertainty of the medium and large cyclist, the accuracy of the Ring of Fire system was improved in this experiment compared to the previous experiments conducted, e.g. by Spoelstra, 2017.
Due to the relatively large out-of-plane velocity gradient for the drafting configuration, the quasi-2D pressure Poisson equation was not able to correctly capture the pressure field thus drag area calculations. This velocity gradient was assumed to be negligible, but in hindsight it could not be neglected.
The effect of drafting distance in lateral direction was found to be 3 times as large as in longitudinal direction. This means that the effect of 10 cm further from the leading cyclist results in a 3 times larger drag increase for the longitudinal re-positioning compared to lateral re-positioning. This effect is visualised in Figure 3.16.

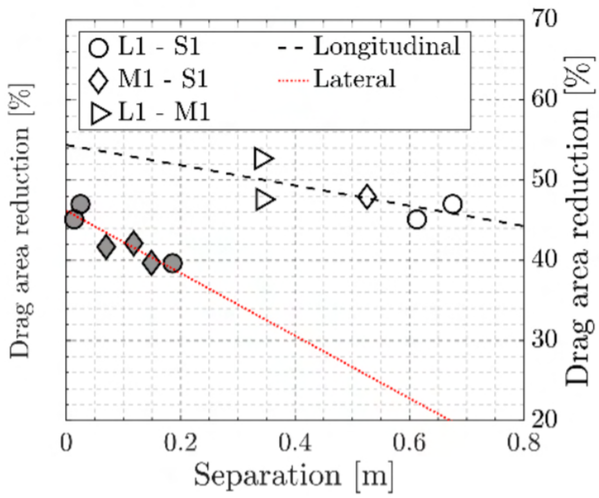

Figure 3.16: Effect of lateral and longitudinal distance in drafting

Chapter 4

Experiment setup and procedures

In this chapter, the setup of the Ring of Fire experiment is described and the associated test procedures are discussed. Firstly, in Section 4.1, the installation of the Ring of Fire is provided, elaborating on the tunnel structure, laser light system, seeding system, imaging system, triggering hardware and acquisition system. Secondly, in Section 4.2, the objects to be tested during the experiment are described. Lastly, in Section 4.3, the daily procedure of the experiment as well as the acquisition procedure are discussed.

Contents

4.1 The setup of the Ring of Fire

The Ring of Fire experiment was conducted outdoor at the Volkswagen proving ground in Germany. This proving ground is located near Ehra-Lessien, a small town located about 20 kilometres north of the Volkswagen headquarters in Wolfsburg. For the Ring of Fire experiment, a road with total length of 950 meters could be used, shown in Figure 4.1. This road was entered from the roundabout located on the right in Figure4.1. The Ring of Fire setup was located at about 300 metres to the left from the roundabout. This part included an additional stroke asphalt of about 30 metres length and 20 metres width on both sides of the road, making it the ideal location for the setup of Ring of Fire construction. The car starting position was located at 685 metres to the left of the Ring of Fire setup as shown in Figure 4.1. This was just long enough to accelerate the cars to the desired test speed of 120 km/h and activate cruise control before entering the laser sheet.

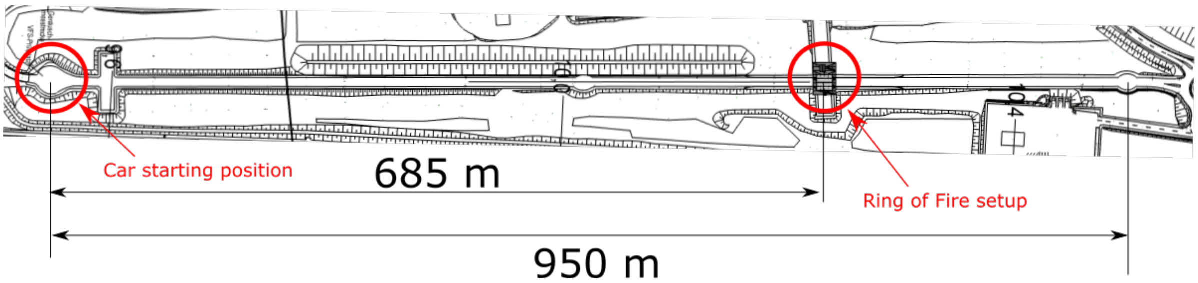

Figure 4.1: Top view of the road including Ring of Fire setup location and car starting position

In this section, consecutively the tunnel structure, laser light system, seeding system, imaging system, triggering hardware and acquisition system are described.

4.1.1 Tunnel structure and general overview

For the Ring of Fire experiment, a tunnel structure is required to keep the soap bubbles inside the measurement domain and generate a sufficient seeding density. Previous experiments by de Martino Norante, 2018 and Hirsch, 2018 were conducted indoors, whereas Spoelstra, 2017 and Mahalingesh, 2020 conducted their respective experiments outdoors. All four showed the necessity for a tunnel structure to contain the particles inside the measurement domain. Especially the outdoor experiments showed that it was difficult to keep the seeding inside the measurement domain and therefore included curtains at the front and back of the tunnel to limit the influence of the environmental conditions during the generation of the seeding. Since the scale of this experiment is larger than previous Ring of Fire experiments (cyclists versus cars), a panel construction or commercial tent would not suffice. Rather, a large, heavy tunnel structure designed by a third party was used.

In Figure 4.2, the tunnel structure that was built for the experiment is shown. The tunnel consisted of two walls and a roof, where both the front and the back of the tunnel were left open. Each wall was located next to the road and consisted of two pairs of ship containers. Two containers were aligned in the driving direction with a small gap between them of about 2 meters and two more containers were placed on top. This was done on both sides of the road. Furthermore, on top of the walls, an aluminum triangular construction was placed which spanned from one side of the road to the opposite side. This construction was covered with a black plastic sheet, which was spanned over it. These together acted as the roof of the tunnel. The final construction was 14 meter long and 5 meter high, measured from the road up to the top of the containers. The distance between the containers on opposite sides of the road was in total 9.17 meters where the road itself was 8 meter wide.

After several days of preliminary testing, it was concluded that the slightest bit of wind would blow too many bubbles outside the tunnel. Therefore, a tarp was placed at the entrance and the exit. These tarps were connected to a metal cord. Metal rings that could be opened and closed were used to attach the tarp to the cord. On one side of the tarp, a rope was connected at the upper corner, so that it could be manually opened from the side of the road by pulling the rope. Closing the tarps while the seeding generators were switched on resulted in an improved seeding density inside the measurement domain. The tarp used for this experiment is shown in Figure 4.2 on the left, hanging in front of the containers.

As shown in Figure 4.2, a construction consisting of beams was created on the ground on both sides of the road, inside the tunnel. The seeding rakes, cameras and lasers could be attached to these beams. This ensured a safe operation of these systems, preventing them from moving around or falling over. Moreover, this way the height and location of each system was easy to set up each day, since these beams were placed at the exact location where the systems had to be.

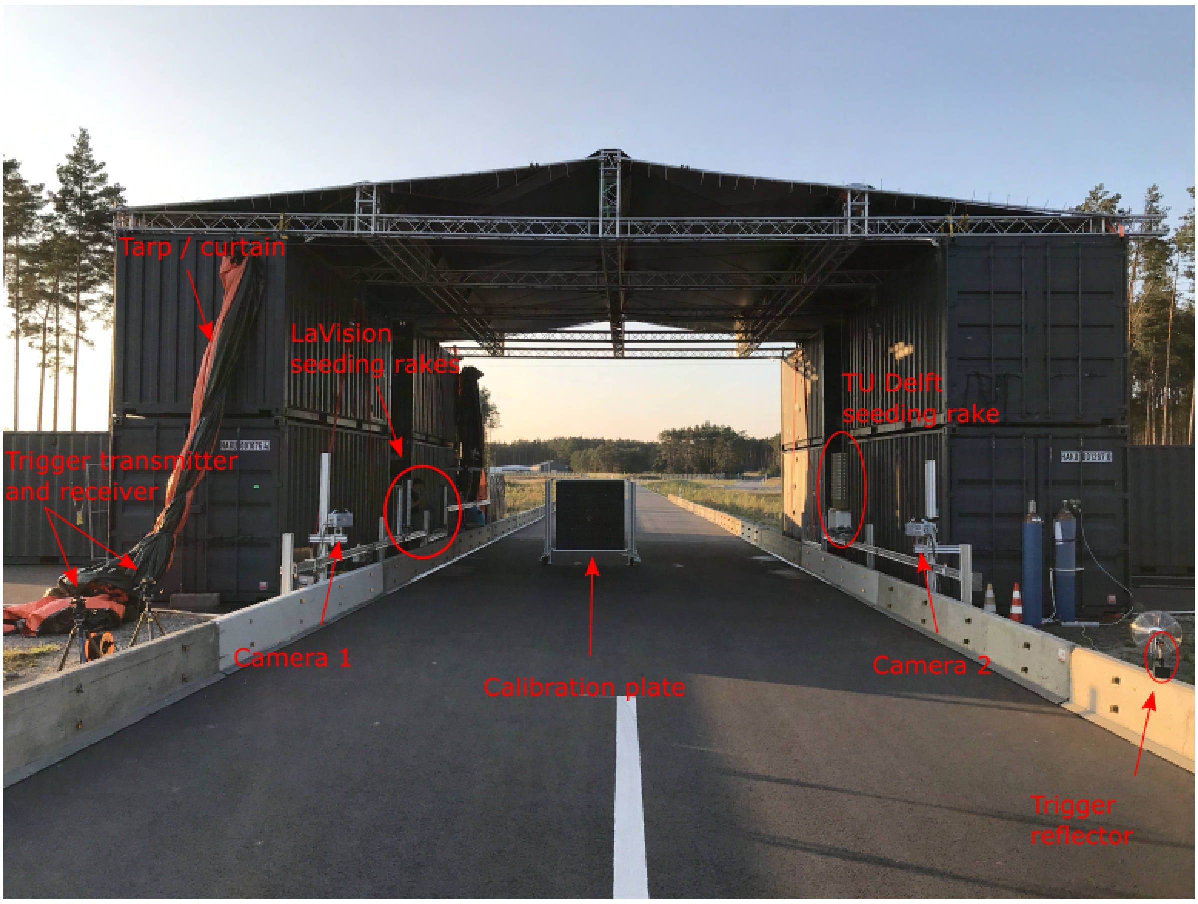

Figure 4.2: Front view of the Ring of Fire tunnel structure

A general overview of the setup is shown in Figure 4.3. It should be noted that this is a schematic of the setup in which the roof and additional tarps are not shown. This Figure will be referred back to in the following subsections when different parts of the setup are discussed.

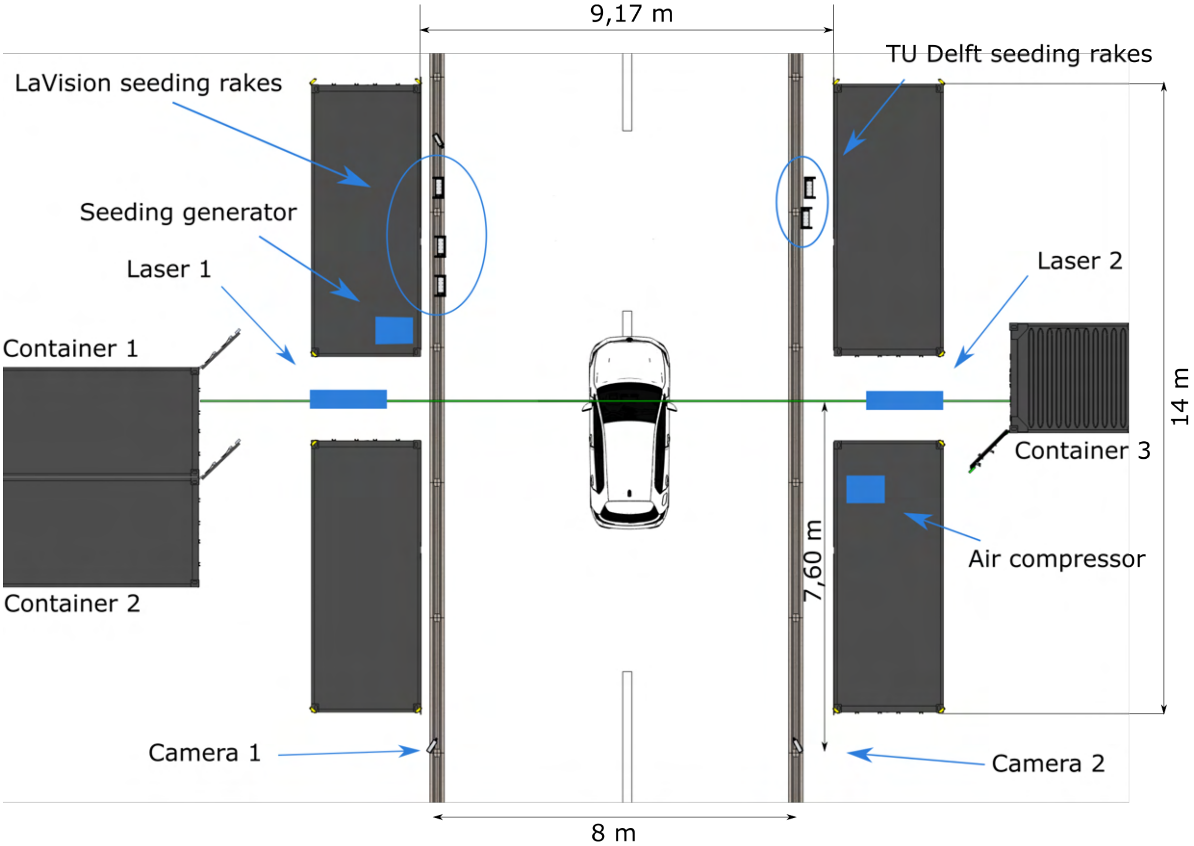

Figure 4.3: Close up top view of the Ring of Fire setup

4.1.2 Laser light system

For the illumination of the field of view, 2 Nd:YAG lasers were used which were provided by LaVision. One laser was the Hawk Pro 40-M, generating an intensity of 6 mJ at a frequency of 6000 Hz, which is shown in Figure 4.4a. The other laser was the Hawk-II 40-M, which was also capable of generating a laser with an intensity of 6mJ at 6000 Hz, which is shown in Figure 4.4b.

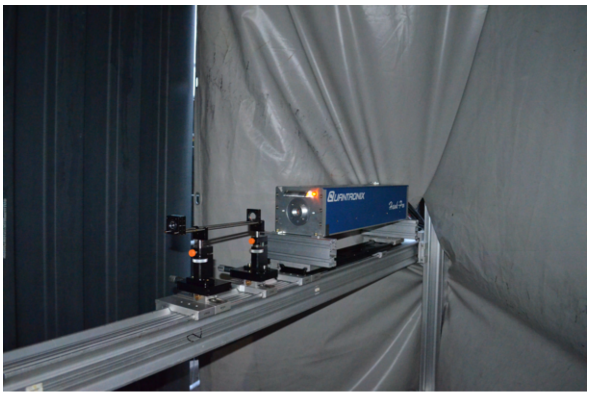

(a) Quantronix Hawk pro laser

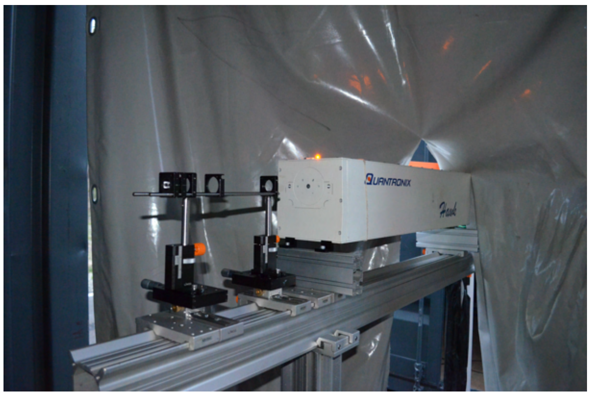

(b) Quantronix Hawk II laser

Figure 4.4: Lasers used in the experiment

Both lasers emitted a green light at a wavelength of 532 nm. During preliminary testing at the start of the measurement campaign only the Hawk II laser was used but it soon became clear that the laser was not strong enough to enlighten the complete field of view, therefore a second laser was used. These lasers were located on either side of the road in between the containers, as shown in Figure 4.3. Their

respective location was at about 6.5 meter from the centreline of the road. Moreover, the lasers were located at 7 meter from the tunnel entrance. A tarp was attached to the roof and hung over the laser in between the containers, to prevent water dripping on top of the lasers from the side of the construction. The lasers were placed at a height of approximately 1.70 meter and laser safety screens were placed around the laser to prevent any laser light from escaping the tunnel.
To shape the laser beam in a sheet, several lenses were used to ensure that the light would expand over the complete field of view without limiting the intensity too much. A spherical lens was placed at approximately 30 cm from the laser output aperture, and a cylindrical lens was placed 10 cm in front of the spherical lens. Since two lasers were used, two trapezoidal laser sheets were formed resulting in an almost rectangle shaped laser sheet, with the upper right and left corner only consisting of light from one laser due to the expansion of the laser. As both lasers also expanded in their thickness, the smallest laser sheet thickness was located at the centre instead of on the right or left as was the case for previous Ring of Fire projects. The laser sheet thickness was approximately 5 centimetres on average in the centre of the road. It was essential that the lasers were aligned, otherwise the intensity of the particles varies and this would lead to suboptimal results. Namely, higher light intensity results in better capturing of the particles by the cameras due to the increased light scattering of the tracers. A thinner light sheet would also increase the light intensity, but would result in less particles inside the laser sheet and would reduce the depth of field that could be achieved with the stereoscopic camera setup.

4.1.3 Seeding system

In previous Ring of Fire experiments only one seeding system was sufficient to fill the measurement domain with enough bubbles. However, due to the large measurement domain that is required to study the flow around cars, two seeding systems were required. These seeding systems consisted of a Fluid Supply Unit (FSU), which was connected to an air compressor, a soap bottle and a compressed helium bottle, a seeding rake and tubes to connect the two. The FSU and air compressor were stored inside the containers, as shown in Figure 4.3. For this Ring of Fire experiment, Helium-Filled Soap Bubbles with a size of 0.3 mm are used which are generated by the FSU, where the pressure for air, helium and soap can be manually modified Scarano et al., 2015. The HFSB were generated continuously at an air pressure of 2.6 bar, helium pressure of 2.1 bar and soap pressure of 1.7 bar. The soap used was LaVision Bubble Fluid Solution (BFS), which consists of soap, glycerin and water.
The seeding generators were connected through tubes to PIV wake rakes. One seeding rake was provided by TU Delft and another one by LaVision. The TU Delft seeding rake was one large rake with 204 nozzles, divided over 12 separate airfoil shaped structures which were equally spaced with a spacing distance of 5 cm. The TU Delft seeding rake is shown in Figure 4.5a. The LaVision seeding rake consisted of three separate rakes, each with 80 nozzles, divided over 4 separate airfoil shaped structures with equal spacing of 5 cm between the nozzles. These were all three connected to the second seeding generator. One of the LaVision wake rakes is shown in Figure 4.5a. Both the seeding rake from TU Delft and from LaVision are commonly used in wind tunnels, where they are aligned with the flow. The airfoil shapes of the rake cause minimal turbulence in the flow, which is desired in wind tunnels. Therefore they have an airfoil shaped structure.

(a) LaVision seeding rake **(b)** TU Delft seeding rake

Figure 4.5: Seeding rakes used in the experiment

The TU Delft seeding rake was located on one side of the road and the seeding rakes of LaVision were located on the opposite side. The seeding rakes were attached to a metal beam construction, which made sure that the rakes operated safely without falling or moving. Depending on the wind direction, the seeding rakes could be manually detached from the beams and moved downstream or upstream, to optimise the seeding density inside the laser sheet.
After the first couple of testing days, it was clear that the soap was too cold due to the weather outside. To have similar operating temperatures for the HFSB compared to indoor experiments, a water tank was heated through which the tubes were lead in order to heat the water, helium and bubble fluid solution. This greatly increased the bubble production and consequently resulted in a higher seeding density.

4.1.4 Imaging system

To capture the movement of the illuminated HFSB, multiple cameras were used. The experiment consisted of an analysis of the flow field in the wake of the cars and an analysis of the flow field around the side mirror. For the wake, two SA-X2 cameras were used, with a resolution of 1024x1024, a pixel size of 20 μm and a limit of 10,000 fps (12 bit, CMOS sensor). These cameras both operated with a 60 mm focal length lens. For the visualization of the side-mirror, one Phantom v2011 and one v1610 were used, both with a resolution of 1280x800 and a pixel size of 28 μm. The Phantom v2011 could provide images up to 22,000 fps and the v1610 up to 16,000 fps. Since the laser could only provide light pulses up to 6 kHz, all cameras were set to capture images at 6 kHz as well. The camera on the left side of the road is shown in Figure 4.6a and the camera on the right side of the road is shown in Figure 4.6b.

(a) Camera on the left side of the road **(b)** Camera on the right side of the road

Figure 4.6: Cameras used in the experiment

The cameras for the stereoscopic PIV measurements of the wake were placed on both sides of the road at the entrance of the tunnel. A quick calculation was performed to determine the location of the cameras and the stereo angle required to capture the field of view. This resulted in a location at 7.60 meter distance from the laser sheet (as shown in Figure 4.3), at a stereo angle of 25 degrees for both cameras. The cameras were placed at a height of 1.20 metre, both pointing at the centre of the laser sheet. The resulting field of view was equal to 3 m by 3 m. Moreover, an image resolution of 0.38 pixel/mm was obtained.

4.1.5 Triggering hardware

At a speed of 120 km/h, it would be extremely difficult to properly start the acquisition of images at the exact same moment each time the car drives through the tunnel. Even though the high speed system takes images at 6000 Hz and therefore the longitudinal alignment when averaging several runs has a maximum offset of 2.8 mm (offset = $\frac{1}{2}\frac{33.33m/s}{6000} = 2.8$ mm), part of the wake may not be captured due to a too early or too late start of the system. Moreover, for convenience sake, an automatic approach for the start of the laser and image acquisition is preferred. Therefore, a triggering system was placed in front of the tunnel entrance on the side of the road at a distance of 5 meter from the tunnel entrance. The transmitter and receiver were located on one side of the road and a reflector on the other side, at a separation distance of 9 meter. The transmitter transmits an invisible laser, which is reflected by the reflector and received by the receiver. When the front wheel of the car passed through the invisible laser of the trigger, a signal was sent to the computer and the laser and acquisition of the images by the cameras was initiated. The triggering hardware is shown in Figure 4.7, where in the front of the image the transmitter and receiver are clearly shown and in the background the reflector is shown.

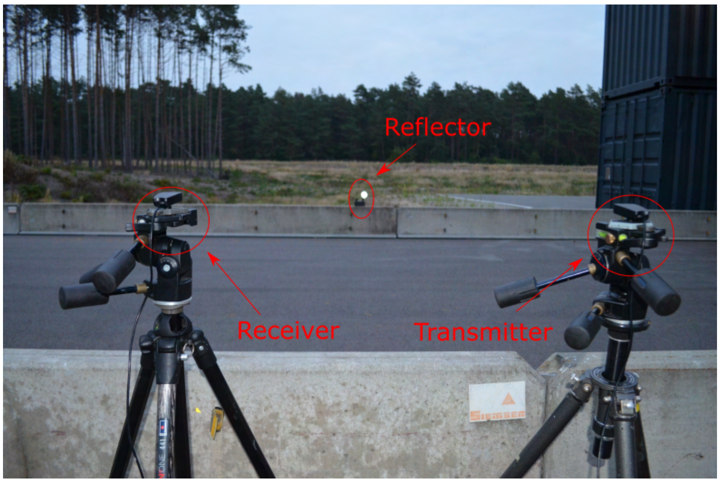

Figure 4.7: Triggering hardware

In the Davis software, the option is selected where the trigger input is used to start the laser and image acquisition. Consequently, the manual option to start the laser and image acquisition is disabled. A signal is sent by the triggering system when an object interrupts the laser between the transmitter and receiver. However, sometimes large rain drops would activate the triggering system as well. This was fortunately only the case for very few runs and unfortunately these runs could therefore not be used. When the laser beam is briefly disconnected, the trigger signal is sent to the computer and based on a user defined delay the laser and image acquisition is started. After the acquisition is completed, the trigger is reset and waits for the next passage of the car.

4.1.6 Acquisition system

The acquisition system consisted of a Microsoft Windows 10 computer provided by LaVision with the latest version (10.2) of the Davis software installed. The computer was located inside container 1 in Figure 4.3 to protect it from the rain and for safe storage. The computer was connected to the

seeding system, the cameras and the triggering system. A network connection between the FSU and the computer was used to start and stop the generation of seeding in the tunnel. A programmable timing unit was connected to the computer through a network cable, to ensure synchronization between the computer, laser and cameras.
The cameras were capable of storing approximately 10,000 images each run at a frequency of 6000 Hz. In the Davis software, this recording frequency and number of desired images are defined. The frequency was limited due to the maximum frequency of the lasers of 6000 Hz. Therefore, images were captured for approximately 1.67 seconds, meaning that the movement of the car was captured over a distance of 55.6 meters. The triggering system was located at 10 meter in front of the entrance and due to a small manually input delay the first image was taken at approximately 10 meters before the car entered the light sheet and the last image at approximately 40 meter in the wake of the car. Due to storage space constraints and time, only 6000 images were saved of each run. Of a few very good runs the full 10,000 images were saved.
With those high speed cameras, a constant pulse separation Δt could be used. This allows the use of time-resolved PIV measurements, meaning that the sliding sum of correlation can be used as explained in Chapter 3.

4.2 Test objects

The test objects in this project were the Volkswagen Tiguan and the Volkswagen Up. These cars were provided by Volkswagen and are shown in Figure 4.8a and Figure 4.8b, respectively. As can be seen in these Figures, the cars were painted completely black and also tape was applied at parts where paint was not sufficient, to ensure that the reflection of the laser light on the cars would be kept at a minimum. Such reflections have caused some trouble in previous Ring of Fire experiments where they lead to erroneous vector fields. Moreover, the cars had pressure taps applied to them and hence pressure measurements could be taken during the experiment as well.

(a) Volkswagen Tiguan **(b)** Volkswagen Up

Figure 4.8: The Volkswagen passenger cars to be tested

The dimensions of the Volkswagen Up and Tiguan are provided in Table 4.1. This shows that the Tiguan is larger than the Up and also the L/W ratio is slightly larger for the Tiguan (2.44) than for the Up (2.20).

Table 4.1: Up and Tiguan dimensions

	Up	Tiguan
Length in [m]	3.60	4.51
Width in [m]	1.64	1.85
Height in [m]	1.50	1.67

Although it is not visualised in Figure 4.8a and Figure 4.8b, the Tiguan has a slightly larger slant angle at the back of the car compared to the Up. Besides, the Up has a slightly more compact shape, whereas the Tiguan has a more stretched out shape and has a relatively larger front part. Moreover, the Tiguan has a small spoiler at the back of the car, as shown in Figure 4.9. The Up does not have such a spoiler.

For the Up, only one configuration was tested where the basic design was considered. For the Tiguan, a distinction was made between a configuration where the radiator at the front of the car was open and a configuration where this radiator was closed. The cars and configurations are referred to as Up, Tiguan front closed and Tiguan front open for the remainder of this report For all three configurations measurements were conducted.

Figure 4.9: Back of the Tiguan

4.3 Experiment procedure

The procedure of the setup of the Ring of Fire started in April 2021 and the aim was to start measurements in the second half of July. However, due to a delay in the design and construction of the tunnel, the experiment could only start at the beginning of August. At that time, the beam construction to which the lasers, cameras and seeding rakes could be attached was built and the computer was installed. Power for the devices was supplied by a power generator located near the setup of the Ring of Fire.
The measurements were conducted at a constant velocity of 120 km/h, which was reached by accelerating the car up to 120 km/h and setting the cruise control to ensure a constant car velocity. This certainly is a benefit implementing the Ring of Fire for cars compared to cyclists, as it is much more convenient to keep a constant velocity for a car than it is for a cyclist.
Since the experiment took place outside, the wind had a big influence on the quality of the measurements. This factor should be reduced as much as possible to keep the seeding concentration inside the tunnel as high as possible. Fortunately, the proving ground of Volkswagen could be accessed by night, as the wind was weaker during this time. Therefore, the decision was made to start the daily setup procedure in the late afternoon when there was still enough day light such that measurements could start when it was dark. Consequently, higher quality measurements could be conducted since the seeding was better contained inside the measurement domain.
The aim of the campaign was to accumulate as many runs as possible in the time frame that the Ring of Fire system could be used, which was approximately from halfway through August until the end of September. The campaign would have been successful if 10-15 runs could be conducted each measurement day. The first two weeks mainly consisted of getting acquainted with the setup procedure and improving it, since some problems arose during this time.

At the beginning, some issues arose that had to be solved. The laser did not work properly as the laser light energy was not constant, it inconsequently fluctuated at high and low energy. After the first two weeks this was suddenly solved by itself, for which no explanation could be given. Moreover, during the

first week the seeding rakes performed poorly and LaVision came up with the idea to heat the seeding by directing the tubes through a small heated water tank of about 50 cm high and a diameter of 50 cm. The operation of the seeding particles as well as the rakes was designed for a higher temperature than the temperature during the experiment and this solved the problem.
Another issue was that especially during the first week there was too much wind and no tarps were used to cover the entrance and exit. Thus, all the seeding particles would fly out of the tunnel structure almost immediately and no proper seeding density could be obtained. It was therefore concluded that tarps were needed and these were installed at the entrance and exit.
The last problem was caused by the rain. The roof was constructed in a flat triangular shape from the front view, as shown in Figure 4.2, to prevent water from accumulating on top. However, the material that was used was a plastic tarp spanned over the metal construction. Due to the wind and rain, water started accumulating at some parts of the roof in large pools. Therefore, these first had to be removed to ensure safe measurements, which took another 2 days to solve. For the rest of the second week the weather was too poor to do any measurements.
Fortunately, during the next 4 weeks in September, the weather was much better and a total of 128 runs were acquired. Out of this total, 31 runs were measured for the Up, 42 runs were measured for the Tiguan with the front closed and 55 runs were measured for the Tiguan with the front open.

4.3.1 Daily setup procedure

The daily setup procedure took about 1.5 hours to complete with 3 operators. Firstly, the power generator was started and the computer was turned on. Next, the cameras, lasers, triggering hardware and seeding generators were put in place and the network connection to the acquisition computer was established. When everything was in place, the valve of the helium bottle and the air compressor were switched on. Preliminary testing of the cameras, lasers and triggering hardware was conducted and the seeding generators were tested. Moreover, atmospheric data was continuously recorded during the complete course of the measurement campaign.

After the setup was completed, the calibration was performed. The geometrical calibration was done using a large calibration plate of size 1.44 x 1.44 meter, which is shown in Figure 4.10. This plate was stored inside the lower left container in Figure 4.3 and was transported to the tunnel using a van. The calibration plate was aligned with the laser pointing axis and perpendicular to the driving direction of the car. The square wooden plate consisted of 324 large white dots with an 8 mm diameter, divided over two levels which formed a staggered grid, with a difference in depth of 20 mm between the levels. 18 holes were equally spaced in the horizontal direction with a spacing of 80 mm and in the vertical direction also 18 holes were equally spaced with a spacing of 80 mm. Moreover, the plate itself was 60 mm thick. A pinhole model was used which is integrated in the Davis software.

The first step in the calibration procedure was an intensity calibration, which was conducted with covered lenses. After the intensity calibration, the caps were removed from the lenses and the f-stop and Scheimpflug adapter were adjusted to get the holes on the calibration plate in focus. When this was achieved, about 10 images were taken of the calibration plate. Using the Davis software, three holes had to be selected to set the reference frame. The centre hole on the plate, which was to be selected as the origin of the reference system, was made clear by placing small pieces of tape on all 4 sides next to it, as shown in Figure 4.10.
The geometrical calibration resulted in a RMS fit of 0.0342 for the left camera and 0.0386 for the right camera. These values were approximately the same for each testing day, where the maximum RMS fit was found to be 0.0378 for the left camera and 0.0432 for the right camera. After the geometrical calibration was finished, the acquisition procedure started. However, still a self-calibration had to be conducted to further reduce the RMS fit. This self-calibration takes a relatively long time and therefore this was not done during the measurements but at the start of the PIV analysis in Davis. Therefore, the self-calibration procedure will be explained in Chapter 5.

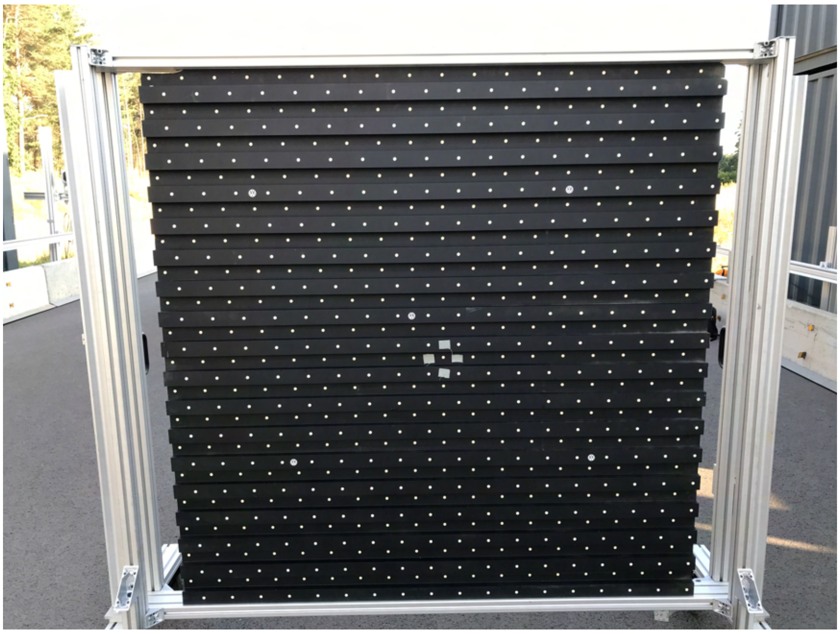

Figure 4.10: Calibration plate on site

4.3.2 Acquisition procedure

After the experiment was set up and the calibration was finished, the measurements could start. At least 3 operators were required to conduct the measurements: operator 1 drove the car and operator 2 and 3 were needed to open the curtain, which could not be done by one operator. For each run, the following procedure was performed for the acquisition of the data:

1. The car was driven to the end of the road by operator 1 to wait for the starting signal
2. Seeding generator was started. It took about 2-3 minutes before sufficient seeding was established inside the tunnel
3. The Davis program was set to triggering mode
4. When operator 1 and 2 agreed that the seeding density was sufficient, a signal was given to the car driver that the measurement could start and operator 1 started driving
5. Approximately 100 meters before the car entered the tunnel, a light signal was given by the driver and the curtain was opened
6. At a distance of 20 meters before the car entered the tunnel, the car drove past the triggering system and the laser and image acquisition were initiated
7. After 1.67 seconds the laser automatically switched off and the image acquisition was finished
8. Operator 1 decelerated the car and drove back to the tunnel
9. The seeding generator was switched off
10. The curtain was put back in place
11. The selected images were stored on the computer, which took about 10-15 minutes

12. The images were checked on their quality (sufficient seeding, reflections, laser fluctuations)

Every 4-5 runs the soap reservoir was checked and more soap was added when the soap level became too low.
At the end of the measurement day, the laser, seeding generator, cameras and triggering system were switched off. The cameras and lasers were dismantled and stored inside container 2. The helium valve and air compressor were closed.

Chapter 5

Data analysis and reduction techniques

In this chapter, the first step in the analysis of the acquired stereoscopic PIV data is described. The process used to create velocity fields from the raw images is elaborated upon in Section 5.1. A selection is made where erroneous velocity fields were excluded and only error free velocity fields were included, which is explained in Subsection 5.2.1. Since it is practically impossible to drive the car exactly at the centre line for each run, lateral repositioning of the velocity fields is required in order to create accurate averages. This process is described in Subsection 5.2.2. The procedure implemented to create vorticity and turbulence plots is explained in 5.2.3 and 5.2.4.
In Section 5.3, the drag is calculated using a Matlab script where the theory explained in Chapter 3 is applied to a car moving inside a control volume. The contouring of the wake and consequently the contouring of the inlet is explained in Subsection 5.3.1 and Subsection 5.3.2. Lastly, the pressure analysis is described in Subsection 5.3.4.
In previous Ring of Fire experiments the data processing for the flow structure around cyclists has been established. Its feasibility for automotive measurements is assessed and adjustments are discussed, proper for the application of the Ring of Fire for cars.

Contents

5.1 Davis processing

The raw data acquired during the Ring of Fire campaign is processed in the same software that was used during the measurements, Davis 10.2. This newer version provided the option of distributed processing, for which the installation of a dispatcher and worker is required. In previous versions of Davis, the user had to wait until the selected PIV operation was finished before the next one could be selected and started, which had to be done manually. Using distributed processing, the PIV operation can be added to a queue, which is processed by a background worker. This means that the user does not have to wait for the job to be finished before the next operation can be started. When the PIV operation is defined, it is sent to the dispatcher which manages the list of jobs to be performed and asks the worker to start these jobs one after the other. Consequently, the user can continue using the software to define changes to the set of images or start looking at the PIV procedure for another set of images without having to wait for the results.
Since the experiment was conducted using a high speed system (at 6000 Hz), about 10,000 images were acquired each run. Analysing such a large amount of data in Davis results in hours and perhaps even days of processing one run for standard stereoscopic PIV. Moreover, due to the relatively low seeding density, non-uniformity of the seeding and the very high out of plane velocity component the sliding sum of correlation method is used for the analysis of the images Sciacchitano et al., 2012. The theory behind this was elaborated upon in Chapter 3. This processing technique however takes even longer to perform than standard PIV operations due to the combination of multiple image pairs and resulting correlation fields, therefore leading to higher waiting times. Thus, for the analysis of the velocity in the wake of the cars, the decision was made to create velocity fields at specified distances behind the car instead of at every few centimetres to severely reduce the computational time. Additionally, an attempt was made to calculate the drag values based on the velocity fields at these distances.

5.1.1 Self-calibration

The processing procedure started with a self-calibration for each individual testing day. Self-calibration should be conducted because the PIV software assumes that all particles are at the calibration plate plane. When the light sheet is not perfectly aligned with the calibration plate, it means that there is a small disparity between the actual location of particles in space and the location where the software ”sees” them. A mathematical tool integrated in the Davis software can be used which takes this misalignment into account by defining a disparity map and correcting the data for this. Especially during this Ring of Fire campaign, being such a large-scale experiment and using two lasers to form one laser sheet, a slight misalignment is likely to happen.
In order to conduct a proper self-calibration, a set of images should be taken where no disturbances such as movement of objects or reflections are visible. Following the suggestions from Wieneke, 2005, 100 images were taken from the start of a good run where the car does not influence the flow, so at approximately 10 meters before the car entered the light sheet. Firstly, the self-calibration procedure was conducted twice using an interrogation window size of 256 pixel with a 50% overlap, followed by using twice an interrogation window size of 128 pixels with a 50% overlap. This resulted in a computed disparity of just below 0.5 pixel (or 1.3 mm), which is in line with the suggestions made by Raffel et al., 2018. More repetitions or smaller interrogation windows did not reduce the disparity further.

5.1.2 Pre-processing

Before the images could be processed with the stereoscopic PIV tool in Davis, several pre-processing steps were undertaken to optimise the results. The main goal of these pre-processing steps is to create more equal intensities across the tracer particles and a sharper contrast between the image and particles, which results in a more similar contribution of each particle to the correlation function.

Since this project is focused on the analysis of the flow topology in the wake of the car, the image set was split in two parts. The first one contained 100 images at 10 meter distance in front of the car which are processed and used for the drag calculation. The second part consisted of the images in the wake of the car, where the first image was taken at the exact moment that the car left the laser sheet. This allowed for a more convenient processing approach since the wake consequently starts at image 1 for all runs (instead of for example 1935 for run 1, 1943 for run 2, etcetera) and reduced the required storage capacity. Namely, the storage capacity was also a limitation to the analysis of complete wake flow fields. To visualise which image is hence taken as the first image in the wake of the car, in Figure 5.1 the first wake image is shown.

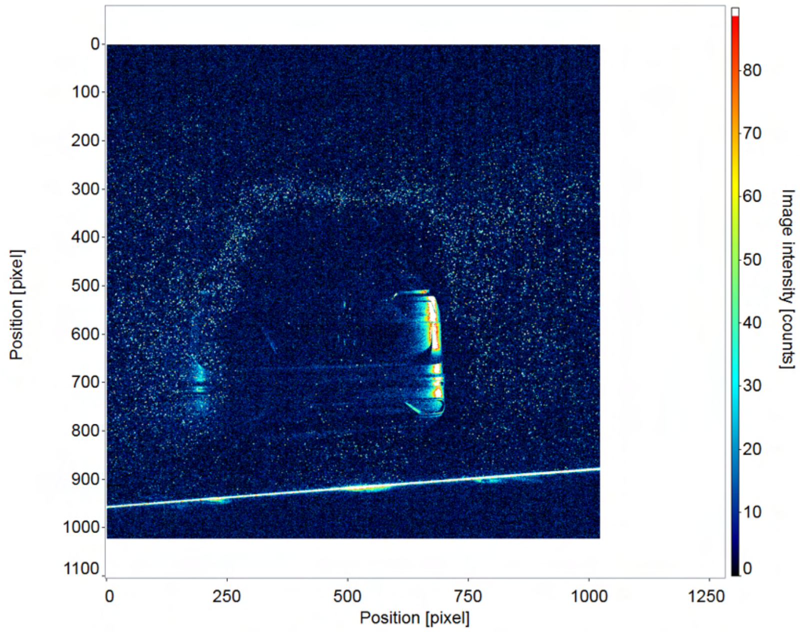

Figure 5.1: First image in the wake, when the car has just left the laser sheet

The first step in this optimisation process was the subtraction of the image background. This was done to ensure equal particle intensity and therefore increasing the accuracy of the correlation function used in the PIV processing. The first 200 images of the image set of each individual run were taken and their average was calculated. This averaged image shows stationary objects, reflections and laser glare which reduce the signal-to-noise ratio (SNR). This average was consequently subtracted pixel by pixel from all the images in the run.

After the subtraction of the average background from the freestream and wake images, a geometrical mask was defined which cut-off the images just above the line where the laser sheet hit the ground. This removed the influence of the reflection of the laser sheet on the ground (even though the intensity of this reflection was already reduced by subtracting the average background, it was still present) and also shaped the dewarped images such that the bottom was a horizontal line and not a combination of two trapezoids.

The last two steps in the pre-processing of the data consisted of subtraction of a sliding background and a min/max filter. Even though the average of the first 100 images was already subtracted from the complete data set, in the first meters of the wake the car still causes reflections in the images and therefore introduces unwanted additional noise. With the operation subtract the sliding background, for each pixel the minimum intensity is determined in the surrounding L pixels and subtracted from that pixel, where L is the filter length. The intention of subtracting the sliding background is to remove large intensity fluctuations in the background while maintaining the lower intensity of the particles. Therefore, the filter length should be at least twice the particle image diameter, to prevent the reduction of the particle intensity. A filter length of 4 was chosen, since this is more than twice the maximum particle image diameter of 2 pixel and larger filter lengths reduced the effect of the sliding background subtraction. After this step, a min/max filter was applied to each image to correct the intensity of each particle, as suggested by Westerweel, 1993. This function is used to create more equally intense particles, reducing the influence of varying bubble size, reflections of the car and laser sheet and non-uniform intensity across the laser sheet. More equally intense particles means that they also contribute more equally to the correlation function, resulting in more robust velocity fields and a higher signal-to-noise ratio. The min/max filter is also used for a user defined tile size, which should be small enough to eliminate spatial fluctuations and large enough such that it is larger than the particle image diameter. Therefore, a filter length of 4 was chosen.

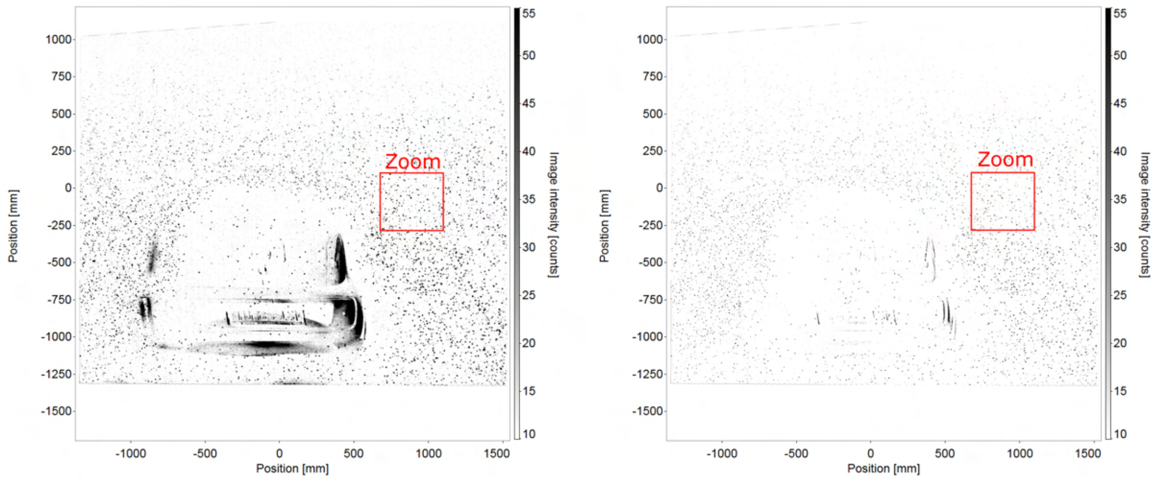

(a) Raw image **(b)** Pre-processed image

Figure 5.2: Comparison before and after pre-processing of a raw image

The result of the pre-processing procedure for the left camera, including the masking, is shown in Figure 5.2. For these figures, an image very close to the car is taken. On the left, in Figure 5.2a, a raw, dewarped image is shown with the illuminated particles inside the laser sheet, without any pre-processing. On the right, in Figure 5.2b, a pre-processed, dewarped image is shown. From these images it is clear that the reflections from the car behind the laser sheet have been reduced drastically and it can be seen that the particles have more or less equal intensity, which is the result from the intensity normalisation using the min/max filters. These images mainly show the effect with respect to the background. In Figure 5.3a and Figure 5.3b, a zoom in of Figure 5.2a and Figure 5.2b to the right of the car is shown, to provide a clearer representation of the effect that the pre-processing procedure has on the display of the particles.

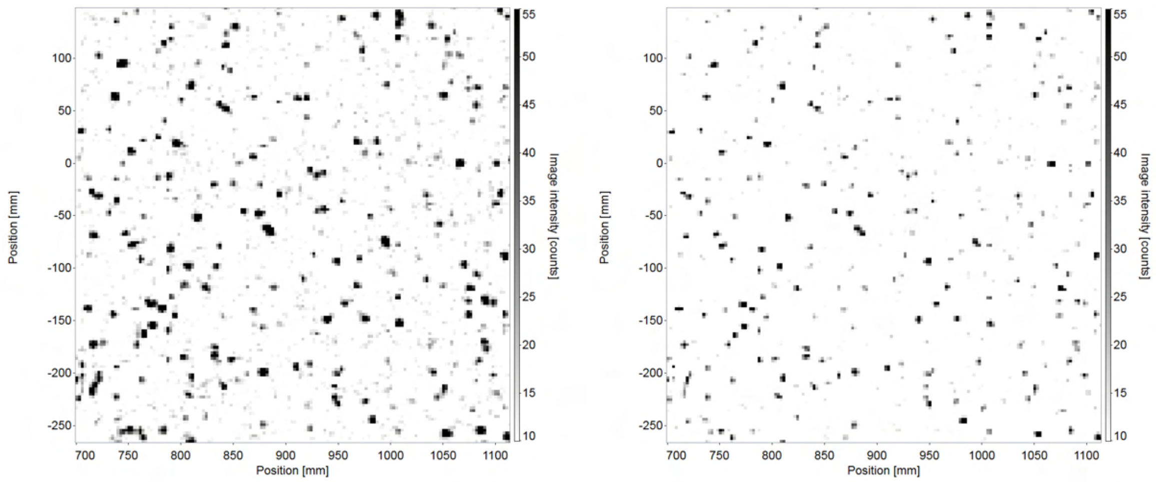

(a) Raw image zoom **(b)** Pre-processed image zoom

Figure 5.3: Zoom in of Figure 5.2a and Figure 5.2b, to show the effect of pre-processing

From these figures, it can be concluded that pre-processing leads to significant reduction in background noise, as the particles are more easily distinguished from the background and also have a more equal intensity. To quantify this reduction in noise, a freestream field is processed twice with the same procedure discussed later in this Chapter. For the first field, the procedure is applied without pre-processing, whereas for the second field the aforementioned pre-processing steps are implemented. The resulting signal-to-noise in the field is plotted to show the reduction in background noise. This is shown in Figure 5.4a and Figure 5.4b, where the signal-to-noise ratio across the image is shown for both the raw image and the pre-processed image.

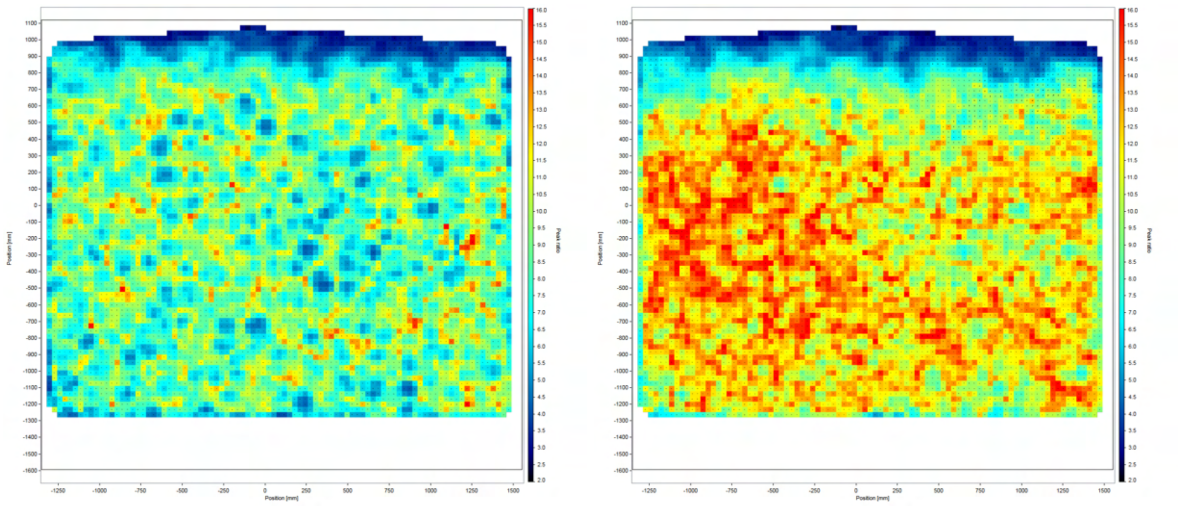

(a) Raw field SNR

(b) Pre-processed field SNR

Figure 5.4: Comparison of cross-correlation SNR field of a raw image and a pre-processed image

Here it is visualised that the SNR for the pre-processed image is a lot better than the SNR of the raw image. This ensures a more robust analysis of the images, since a high SNR indicates a good agreement between the displacement of the particle pairs inside an interrogation window. This is especially beneficial in the near wake, where the SNR is typically a lot lower due to the high velocity and turbulence.

5.1.3 Processing

The pre-processed data is subjected to the stereo-PIV time resolved sliding sum of correlation in Davis 10.2. This method has been explained in Section 3.1.2. The filter length L and the separation time Δt should be manually chosen by the user. The choice of Δt is based on the maximum out-of-plane displacement allowed for stereoscopic PIV. As a rule of thumb, the maximum displacement across the laser sheet should not exceed 1/4th of the sheet thickness. If the displacement becomes larger than this, too many particles leave the sheet between subsequent images, resulting in a loss in correlation and thus widening and lowering the correlation peak. This leads to a higher uncertainty and possibly even to areas without velocity vectors. In this project, an acquisition frequency of 6 kHz is used and the cars ride at a velocity of 120 km/h, or 33.33 m/s. From preliminary analysis of the images using basic stereo PIV operations, the maximum velocity occurred in the near wake and was about 40 m/s. This results in a maximum displacement of the particles between images of $40/6000 = 0.0067$ m. This would result in a minimum laser sheet thickness of 2.6 cm. Since the laser sheet in this project is about 5 cm thick, a $\Delta t = 2\Delta t_0$, where $\Delta t_0 = 1/6000 = 0.167$ s could be used as well. This means that each image is correlated with the second successive image. Typically, PIV measurement errors are in the order of 0.1 pixels as reported by Adrian and Westerweel, 2011. Thus, by increasing the total distance covered by particles between images the relative uncertainty becomes smaller. Preliminary analyses done with a larger Δt of $3\Delta t_0$ showed that for some data sets this was a feasible option, but for most it resulted in erroneous vector fields. Therefore, a Δt of $2\Delta t_0$ was used.

The next step was to select an appropriate interrogation window size. A multi-pass operation was used with decreasing window size. Firstly, an initial pass using an interrogation window of 64x64 with an overlap of 50% and no weighting was used. This initial pass serves as a reference vector field for a decreasing window size in the next passes. This allows for a more reliable and accurate vector field, as the information from larger window sizes is used to determine the particle displacement in smaller windows, meaning that it is much less of an issue if a particle leaves the window since its displacement has already been estimated in a prior pass. The interrogation window for the final pass is based on the one-quarter rule. This rule indicates that the in-plane displacement should be at most one quarter of the interrogation window. Preliminary PIV showed that the in-plane components were at maximum about 17 m/s, meaning that between two consecutive images (with $\Delta t = 2\Delta_0$) the average displacement was 5.7 mm. This equals to a pixel displacement of approximately 2-3. Therefore, the interrogation window should be at least 12x12 pixels. However, for good results, the number of particles inside one interrogation window should be at least 10-15 particles. With an average particle per pixel density of 0.009-0.018, the minimum required interrogation window is 48x48. Moreover, a previous Ring of Fire uncertainty analysis conducted by Spoelstra et al., 2020 suggested an interrogation window size between 0.05c and 0.25c, where c is the characteristic length of the test object. This was based on an uncertainty analysis where smaller windows would lead to random errors in regions of insufficient seeding and where larger windows would lead to modulation. For the cyclists, this characteristic length was the width of the shoulders and therefore it seemed most reasonable to use the width of the car for this project. With a width of 1.85 meters, this implicated a minimum window size of 36 pixels, meaning that the minimum interrogation window size was 48x48 pixel as the first window that was smaller was the 32x32 pixel window. The authors noted however that this suggestion should be used with care, since it depends a lot on seeding density and pixel size of the camera. Nonetheless, since this project is also a Ring of Fire experiment and the seeding density was more or less the same, the suggestion is assumed to be applicable. Most runs could have been processed with smaller window sizes, however for consistency a final interrogation window of 48x48 was chosen. The complete multi-pass process started a single pass with a 64x64 interrogation window, 50% overlap and square weighting. Consecutively, 3 passes were conducted at a window size of 48x48, 75% overlap and Gaussian weighting. 3 passes were selected since according to Raffel et al., 2018 convergence is then commonly reached. A 75% overlap was chosen to increase the spatial resolution. An even higher overlap may increase the spatial resolution even more but the computational time becomes a big issue, and this overlap was deemed sufficient for reliable and accurate results. For the interrogation windows, a Gaussian weighting was applied. This weighting basically applies a higher weight to particles in the centre of the window compared to particles at the edge of the window, since these particles are more likely to move outside the interrogation window. This therefore also enhances the reliability and accuracy of the vector fields. Lastly, a universal outlier detection is used during the multi-pass processing. This already filters out any outliers in between the first pass and the subsequent passes, resulting in less erroneous vector fields.

For choosing an appropriate filter length, a velocity field was created at 1 meter in the wake using the aforementioned time separation Δt and interrogation window size. Filter lengths starting from 1 up to 10 were analysed and from this analysis the vector field became error free once the filter length became 7 or higher. This filter length essentially increases the number of correlation maps used to create the velocity field. It should be noted however, that these correlation maps are Gaussian weighted. This means that the influence of correlation maps furthest away from the desired image are dampened. Another aspect to take into account is that although a Gaussian weighting is used, a larger filter length creates more "average-like" velocity fields. That is, if the filter length becomes too large the velocity field can no longer be considered instantaneous but rather should be considered as averaged. With a filter length of 7 and a Δt of $2\Delta t_0$, this results in a velocity field where the outer images used for the correlation are approximately 15 cm apart, hence 7.5 cm in front of the desired vector field location and 7.5 cm behind.

5.1.4 Post-processing

After the processing of the velocity fields, a post-processing routine was applied when necessary. Since this is the first ever application of the Ring of Fire system in the automotive industry, there is no prior knowledge (except for the previous Ring of Fire campaigns for cyclists) about the potential uncertainty, as well as the wake behaviour around cars in an outdoor environment. Besides, the Ring of Fire has not been deployed using two lasers and at a scale this large, much larger even than the cyclist Ring

of Fire experiments. Therefore, the vector fields should be kept as raw as possible and no smoothing is performed. Smoothing could lead to the reduction in velocity peaks and result in a too smooth, unphysical wake behaviour.
By visual inspection, the vector fields were analysed and when clear outliers were visible, a post-processing routine was performed consisting of a universal outlier detection with a size of 5x5 pixel. This would remove the outlier and replace it with a vector consistent with the surrounding vectors in a range of 5x5 pixel. Moreover, if any empty spaces were left in the vector fields, an interpolation function was used to fill them up.

To show the quality of the measurements, commonly the Dynamic Spatial Range (DSR) and the Dynamic Velocity Range (DVR) are used. The DSR is the ratio of the maximum resolvable length scale over the minimum resolvable length scale. The maximum resolvable length scale is the size of the field of view, therefore a DSR can be defined in the horizontal and vertical direction in case these are not of equal length. The minimum resolvable length scale is the size of the interrogation window. The size of the dewarped images was 1094x1032 pixels and an interrogation window size was used of 48x48 pixels.
This results in the following value for the DSR:

$$DSR = \frac{1094}{48} = 23 \tag{5.1}$$

The second indicator is the Dynamic Velocity Range. The DVR is the ratio of the maximum resolvable velocity over the minimum resolvable velocity. The maximum velocity was obtained in the near wake of the car, where a velocity up to 42 m/s was measured. For the minimum resolvable velocity, one standard deviation is taken from 40 velocity fields taken in the almost quiescent air. This standard deviation is then taken as measurement noise and used as the smallest resolvable timescale. This results in the following DVR:

$$DVR = \frac{42}{0.15} = 282 \tag{5.2}$$

A higher DVR is achieved compared to previous Ring of Fire experiments using cyclists. This is to be expected, certainly because the car is moving a lot faster than the cyclists. However, due to the wind in the outdoor environment the minimum resolvable velocity is rather large, therefore the DVR is only slightly larger than those reported by de Martino Norante, 2018 (250), Spoelstra, 2017 (100), Hirsch, 2018 (266) and Mahalingesh, 2020 (124).

5.2 Data reduction

After the PIV analysis in Davis, firstly a run selection is performed to exclude the runs with erroneous vector fields due to insufficient seeding. Next, the included velocity fields were exported to dat files. This type of file was required to analyse the velocity fields in Matlab and also calculate the drag. In this Section, the procedure is explained where the exported vector fields are loaded in Matlab and how vorticity, turbulence and average velocity fields were established.

5.2.1 Run selection

One of the drawbacks of the Ring of Fire, especially for the large scale considered in this project, is the extreme difficulty to create sufficient seeding density in a uniform manner. Even though the four seeding rakes together produced a lot of bubbles, it was in practice very hard to keep the bubbles inside the tunnel near the laser sheet. Moreover, due to the convection of the wake behind the car, up to several meters before the laser sheet in driving direction the seeding density should already be sufficient. These particles follow the car due to the convective nature of the wake and therefore travel several meters behind the car. Thus, to ensure proper measurements up to 5-10 meters behind the car, a very large volume should be uniformly filled with bubbles.
Windy and rainy days resulted in poor quality measurements, which meant that quite some runs had to be excluded. For this experiment, it was rather easy to distinguish between good runs and poor runs,

since the vector fields resulting from poor runs contained lots of erroneous vectors as well as small or large spots with very low velocity in the near wake. An example of a poor quality run is shown in Figure 5.5a, where an example of a good quality run is shown in Figure 5.5b. It can be seen that for the poor quality run, the seeding is insufficient in the lower region of the field of view (below 0.5 meter). For the good quality run, this part of the field of view is sufficiently seeded. Comparing the resulting vector fields in Figure 5.5c and Figure 5.5d, erroneous vectors as well as holes inside the wake occur for the insufficiently seeded image, whereas the sufficiently seeded image provides a good vector field. Hence, the insufficient seeding results in too few particles to get accurate velocity vectors or in some parts of the field, no velocity vectors at all.

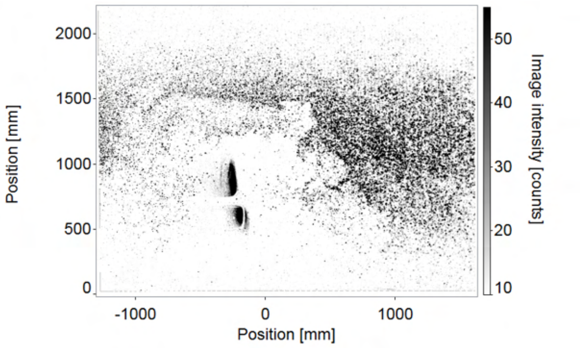

(a) Raw image at 1 meter of run 03 on 01-09-2021, insufficient seeding

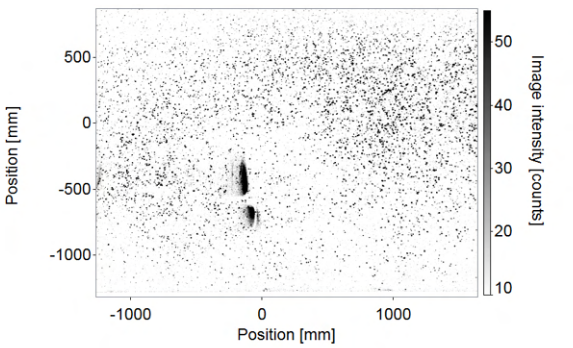

(b) Raw image at 1 meter of run 03 on 21-09-2021, sufficient seeding

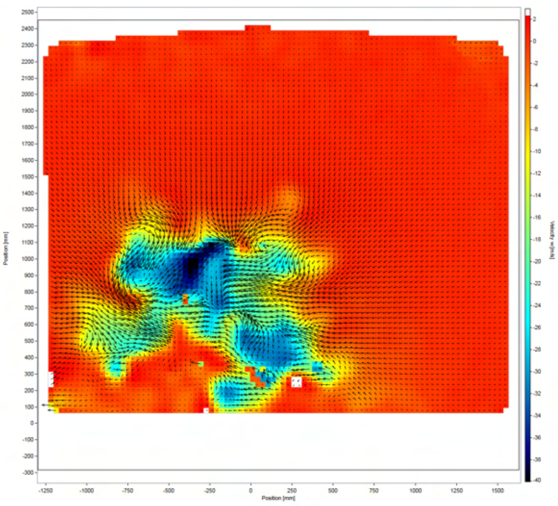

(c) Run 03 of the Up on 01-09-2021, showing clear errors

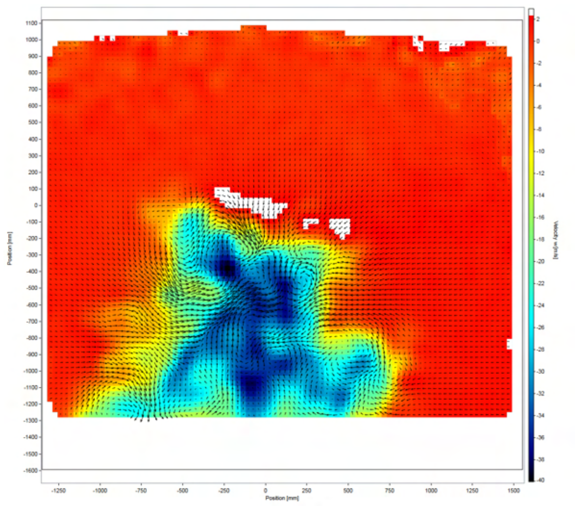

(d) Run 03 of the Up on 21-09-2021, good run

Figure 5.5: Good and bad run

5.2.2 Lateral repositioning

One of the other drawbacks of the Ring of Fire system is the repeatability. In this Subsection, not necessarily the repeatability itself is discussed but rather the difficulty to create wakes at the same lateral position for each run. This is necessary in order to ensemble average multiple runs to get an ensemble averaged velocity field and thus visualise the macrostructures in the wake. If this would not be done properly, the vortices that would be the same "in real life" would occur at different locations in the velocity field, giving the false impression that these vortices are separate.

During the experiment, markers were drawn on the ground to show the centre of the road to the driver of the car. Nevertheless, the car had a slight offset for nearly all runs with a maximum of approximately 20 centimetres either to the left or to the right of the centreline. Fortunately, this could be resolved through visual inspection. For each run, the image was taken where the Volkswagen logo at the back of the car just moved through the laser sheet, and the lateral position of the centre of the logo with respect to the origin of the coordinate system was noted. This was later corrected for when the ensemble average plots were created in Matlab, which will be described in Subsection 5.2.5. In Figure 5.6a, a run is shown on 03-09-2021, during the measurements of the Up, where an offset of 210 mm to the left of the origin occurred. In Figure 5.6b, a run is shown on 16-09-2021, during the measurements of the Tiguan, where an offset of 120 mm to the right of the origin occurred. These values were used as correction in later averaging of the velocity fields.

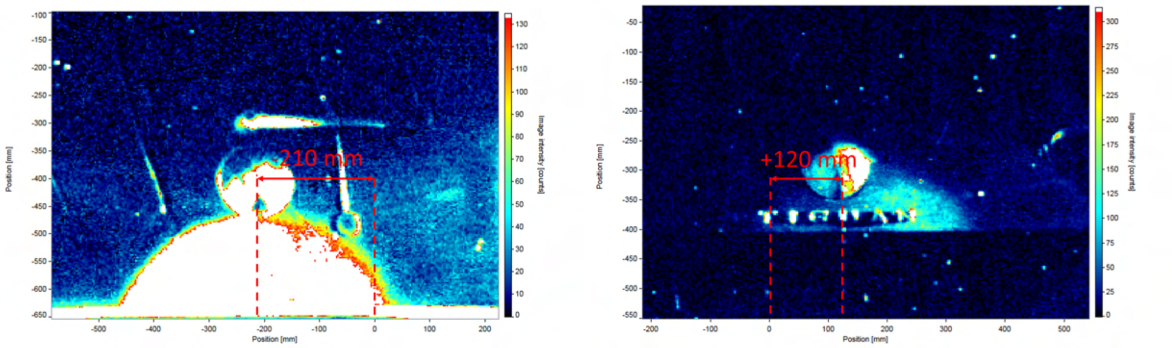

(a) Run 08 of the Up on 03-09-2021, offset 210 mm to the left

(b) Run 01 of the Tiguan on 16-09-2021, offset 120 mm to the right

Figure 5.6: Example of different offsets with respect to origin during the Ring of Fire measurements

5.2.3 Vorticity

For the drag calculations using the control volume approach, only the vector fields of the velocity are necessary. Nonetheless, for a proper aerodynamic analysis of the flow topology in the wake of a car, the vorticity provides useful information as well. The vorticity aids in defining the coherent structures in the wake of the car, providing additional aerodynamic insight next to the already computed velocity fields. Jeong and Hussain, 1995 define coherent structures as *"spatially coherent, temporally evolving vortical motions"*. In this project, only the out-of-plane vorticity can be computed with the planar vector fields resulting from the stereo PIV measurements. The out-of-plane vorticity is defined as the z-component of the curl of the velocity field, and is therefore calculated in 2D using equation 5.3:

$$\omega = \nabla \times \vec{u} = \frac{\partial v}{\partial x} - \frac{\partial u}{\partial y} \tag{5.3}$$

It should be noted however, that only the two dimensional velocity gradient tensors can be analysed. This means that no distinction can be made between a shear layer and a vortex, for which three dimensional velocity gradient tensors are required. In a previous Ring of Fire experiment conducted by Spoelstra, 2017, the Q-criterion was used to distinguish a vortex from a shear layer. The main idea of the Q-criterion is to use the second invariant of the velocity tensor and decompose it in a symmetric and asymmetric part, where the symmetric part S represents a vortex and the asymmetric part Ω represents a shear layer:

$$\nabla\vec{u} = S_{ij} + \Omega_{ij} = \frac{1}{2}(\nabla\vec{u} + \nabla\vec{u}^T) + \frac{1}{2}(\nabla\vec{u} - \nabla\vec{u}^T) \tag{5.4}$$

The symmetric and asymmetric part of the tensor are then used to define the Q-criterion:

$$Q = \frac{1}{2}(||\Omega||^2 - ||S||^2) \tag{5.5}$$

Equation 5.5 shows a balance between the asymmetric and symmetric part. Therefore, when $Q > 0$, this means that the asymmetric part dominates and therefore the vorticity consists of a real vortex. Contrary, if $Q < 0$, the symmetric part dominates the equation and the vorticity consists of a shear layer. In a later Ring of Fire experiment conducted by de Martino Norante, 2018, the λ_2 criterion was used, which was first defined by by Jeong and Hussain, 1995. The authors came up with the λ_2 criterion, which defines a vortex as *"pressure minimum in a plane, when contributions of unsteady irrotational straining and viscous terms in the Navier-Stokes equations are discarded"*. A vortex core is defined when two negative eigenvalues are found in a connected region of the sum of the symmetric and antisymmetric parts of the velocity gradient tensor. Therefore, the equation is slightly different from Equation 5.5, as shown in Equation 5.6:

$$A = \frac{1}{2}(\Omega^2 + S^2) \tag{5.6}$$

Where λ_2 is defined as the second eigenvalue of A.
The Q-criterion and λ_2 criterion are both able to distinguish between shear layers and actual vortices and may therefore be a more useful tools to show and analyse the vorticity field. Nonetheless, the authors noted that the regions defined by the Q-criterion and λ_2 criterion in planar flows should be the same Jeong and Hussain, 1995 as both lead to the same result when applied to a 2D flow, which is assumed to be the case in this project since the out-of-plane gradient cannot be measured and is therefore assumed to be negligible.

5.2.4 Turbulence

Another flow variable that can be looked at in the analysis of the flow topology in the wake is the turbulence. Turbulence is commonly defined as the unsteadiness or disorder of a flow. However, the basic nature and an exact definition of turbulence has not been defined and is still being studied nowadays. Therefore, for the scope of this project, the turbulence is defined as the deviation from the mean flow. Moreover, it is defined as the deviation from the mean in a plane at a specified distance behind the car. This means that for each day, the standard deviation of all runs at e.g. 1 meter is calculated and plotted, to show the unsteadiness of the flow at this distance.

5.2.5 Averaging of the flow fields

Averaging of the velocity fields is necessary if the macro behaviour of the wake behind the car is to be analysed. Therefore, the lateral reposition approach described in Subsection 5.2.2 is implemented to shift all velocity fields such that their respective centres are aligned. Consequently, all velocity fields are cropped in lateral position, since the outer edges are not the same due to the lateral shift. Therefore, the inner "edges" of the velocity fields are used as the lateral limits of the plotting. A schematic of this procedure is shown in Figure 5.7.

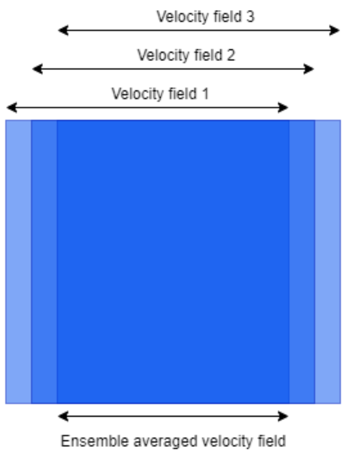

Figure 5.7: Schematic of lateral repositioning procedure

In this Figure, it can be seen that the velocity fields are laid on top of each other and the inner boundaries are selected to act as the limits of the ensemble averaged velocity field. After the lateral shifts have been measured through visiual inspection and the fields are cropped, the mean function in Matlab is used and the average velocity field is computed.

5.3 Drag calculation

For the drag calculation, the control volume approach as discussed in Chapter 3.2 is used. From Equation 3.15, it is evident that the inlet contour, outlet contour or wake contour, velocity of the car and the pressure are necessary. Firstly, the wake contouring is performed and the inlet plane is created accordingly. Secondly, the pressure field is calculated and the resulting momentum and pressure deficit together lead to the calculation of the drag.

5.3.1 Wake contouring

To create an an outlet plane in the wake, a procedure was implemented where a contour was drawn around the wake of the car. A similar approach to the one described by Hirsch, 2018 was used. Outside of this contour, the environmental velocity fluctuations were set to 0 and only the velocity values inside the contouring were used for the outlet plane.

The wake behind the car is assumed to be a coherent structure. Typically, in the centre of the wake the largest velocities are reached which gradually decrease outwards, until the freestream conditions are recovered. Since the velocities in this experiment are defined negative in driving direction, the smallest velocities are found inside the wake region. To define the boundary of the wake, a cut-off velocity is used. Most values that are smaller than the cut-off velocity are located inside the wake and are therefore assigned the value 1 and all values that are larger than the cut-off velocity are assigned the value 0, since these are located outside the wake. However, there may still be velocities in the vector fields that are smaller (more negative) than this cut-off velocity hence they have been assigned a value of 1, but are not part of the wake. To prevent these from influencing the drag calculations, the wake of the car is considered to be a coherent structure. Therefore, the largest island of ones is found in the matrix. All ones that are not included inside this island are set to 0 as well.

Additionally, since this wake contouring procedure is used for planes in the near wake as well as in the far wake, selecting a constant value for the cut-off velocity is not sufficient. Namely, if this value is set too low then the contouring is inaccurate in the near wake due to the potential inclusion of non-wake regions but if the value is set too high than the wake contouring does not work in the far wake as the velocities inside the wake approach the cut-off velocity. Through visual inspection of the wake contour size, the cut-off velocity could be determined.

At last, the cut-off velocity is a rather rigorous and absolute definition of where the wake starts and ends. To take into account the shear layer, a Gaussian 3x3 matrix is used to estimate the dilation of the wake. Therefore, the cells directly connected to the outer ring of the largest coherent structure are also assigned the value 1 and are hence also included in the wake contour.

The resulting wake contours for varying cut-off velocities are shown in Figure, where the wake at 1 meter behind the car is shown for several cut-off velocities of 20%, 30% and 40% of the 5th percentile of the wake velocity, which equals -6.47, -9.71 and -12.95 m/s, respectively. The outer layer of the contour is shown in comparison to the actual velocity field, to determine which velocity should be used.

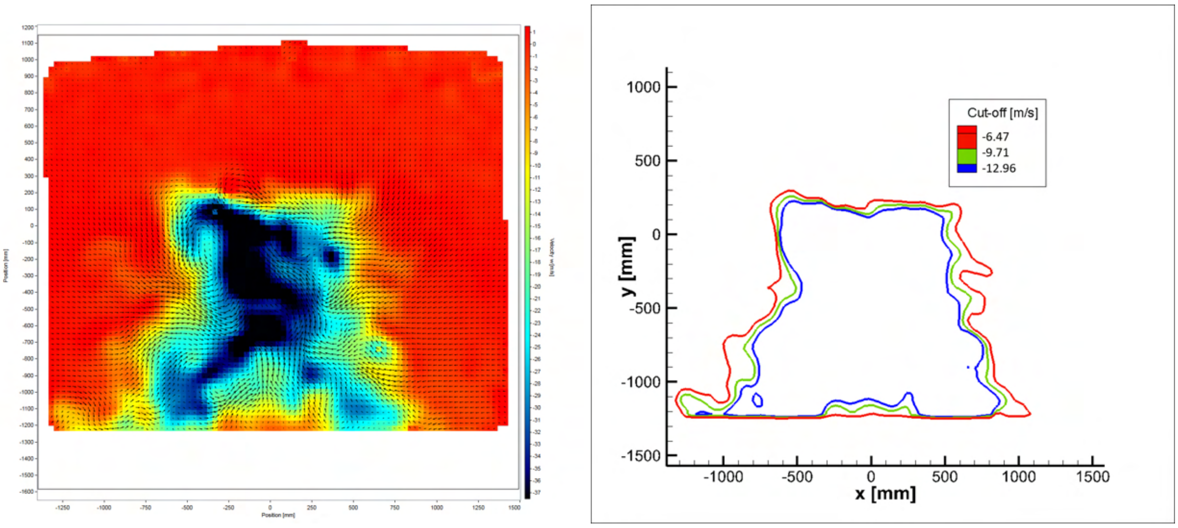

(a) Velocity field as a demonstration for the cut-off velocity

(b) Different cut-off velocities for wake contouring

Figure 5.8: Effect of cut-off velocity on wake contouring

Comparing this figure to the velocity profile for which this contouring had been calculated, it can be seen that for values lower than 30% the wake is too dilated and for values larger than 30% the wake is excessively cut. The 40% contour contains holes in the wake which is not in line with the previously defined assumption that the wake is a coherent structure. The 20% contour is too dilated, which follows from preliminary drag calculations resulting in a too high Cd, which will be discussed in Chapter 6. Hence, the cut-off velocity is determined as 30% of the 5th percentile of the wake velocity. This means that the cut-off velocity is adjusted further downstream leading to a universal use of this velocity in the complete wake, without excessive cutting in the contouring which would likely happen for a constant cut-off value.
After the wake contouring has been established, the original values of the velocity in the wake are again superimposed inside the wake region. This results in one island of velocities where all velocities outside the wake are 0, which is used in the calculation of the momentum deficit between the outlet and inlet plane.

5.3.2 Inlet plane selection by conservation of mass

As the wake contouring has now been established, the inlet plane can be shaped accordingly. The inlet plane contour is constrained by conservation of mass. In the control volume, it is assumed that the mass flow through the upper, lower, right and left boundary is 0. Mass is assumed to only flow through the inlet and outlet plane. Since solely the velocity inside the wake contour is used for the drag calculations, the mass flow in the outlet plane outside the wake region is also set to 0. Hence, the mass flow occurs through the wake plane and the inlet plane should be adjusted accordingly. Since for the drag calculations the car velocity is added to the velocity vectors in the inlet and outlet plane, the inlet plane has a higher velocity and consequently should be smaller than the outlet plane for mass conservation. Therefore, a shrinking function has been defined. The function starts by projecting the wake contour on to the inlet plane and the mass flow ratio between the inlet and outlet is calculated accordingly. Then, if this value is larger than one, the outer 'layer' of the island of 1's is set to 0 and the mass flow ratio is recalculated. This procedure is repeated until the value for the mass flow ratio converges to 1, which indicates that mass is conserved inside the control volume. This technique is shown in Figure 5.9, where on the left the wake contour is shown and on the right the shrinking procedure to the inlet contour is shown. The resulting contour surface is then used to calculate the momentum deficit.

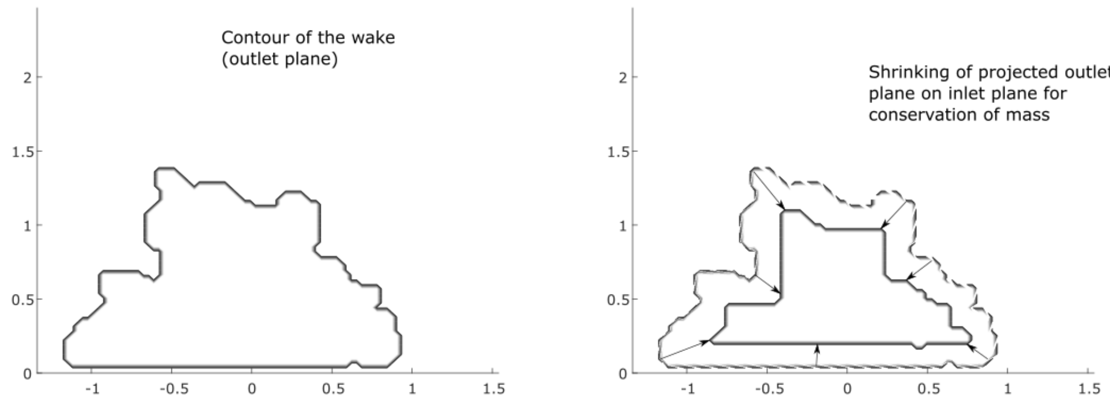

Figure 5.9: Shaping of the inlet plane according to mass conservation

5.3.3 Momentum deficit

The main contributor to the calculation of the drag is the momentum term as was shown in Equation 3.15. The momentum term is calculated using the velocity field obtained through the outlet and inlet plane contouring. For both the inlet plane as well as the outlet plane, the momentum is calculated by multiplying each individual out-of-plane velocity component with its area. This area is a square, of which the width and height are equal to the spacing between the vectors. Subsequently, the difference between the inlet and outlet is defined as the momentum deficit.

5.3.4 Pressure determination

Additionally to the momentum deficit, the pressure should be calculated as well in order to get accurate drag values close to the car. Not only does the pressure aid in a more accurate calculation of the drag, the pressure field can also be used as a visualisation to elaborate in the characterisation of the wake structures. The approach as described in Chapter 3 is used, where a 2D Pressure Poisson equation is implemented in Matlab.

In order to solve the Equation 3.20, the 2D Pressure Poisson equation was rewritten, which is shown in Equation 5.7:

$$\frac{\partial^2 p}{\partial x^2} + \frac{\partial^2 p}{\partial y^2} = \frac{\partial}{\partial x}(\frac{\partial p}{\partial x}) + \frac{\partial}{\partial y}(\frac{\partial p}{\partial y}) \tag{5.7}$$

Where

$$\frac{\partial p}{\partial x} = -\rho(u\frac{\partial u}{\partial x} + v\frac{\partial u}{\partial y}) + \mu(\frac{\partial^2 u}{\partial x^2} + \frac{\partial^2 u}{\partial y^2}) \tag{5.8}$$

$$\frac{\partial p}{\partial y} = -\rho(u\frac{\partial v}{\partial x} + v\frac{\partial v}{\partial y}) + \mu(\frac{\partial^2 v}{\partial x^2} + \frac{\partial^2 v}{\partial y^2}) \tag{5.9}$$

When the velocities are discrete measurements divided over a grid, the following linear system of equations has to be solved:

$$Ap = b \tag{5.10}$$

Where A represents the two dimensional Laplace operator, which is discretized and consequently solved with a second order five-point difference scheme:

$$\Delta p = \frac{p(i+1,j) + p(i-1,j) + p(i,j+1) + p(i,j-1) - 4p(i,j)}{h^2} \tag{5.11}$$

Where h is the spacing between the points and i and j are the points in x- and y-direction on the grid. The second derivative of the velocities was calculated with a central difference scheme for the inner points, a forward difference scheme for the top and left boundaries and a backward difference scheme for the right and bottom boundaries.
For the boundary conditions, Neumann was applied on the bottom, right and left boundary whereas on the top boundary a Dirichlet boundary condition was applied using Bernoulli:

$$p_{topboundary} = p_\infty + \frac{1}{2}\rho V_\infty^2 - \frac{1}{2}\rho V_{topboundary}^2 \tag{5.12}$$

A schematic representation of the implemented boundary conditions is shown in Figure 5.10:

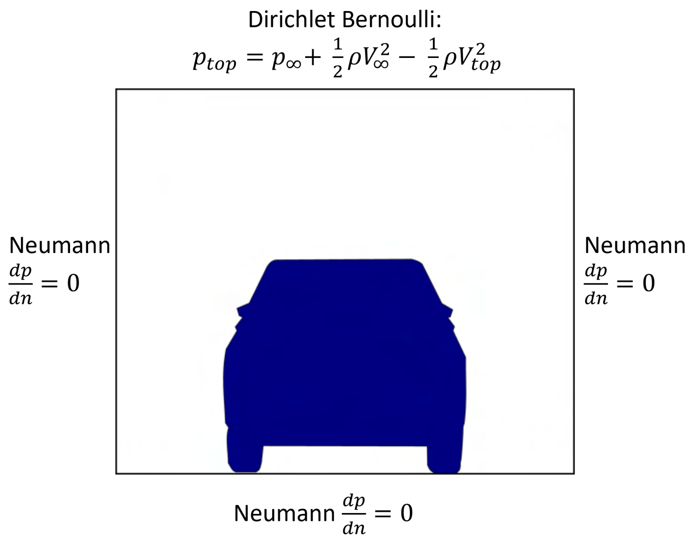

Figure 5.10: Schematic of boundary conditions for Pressure Poisson equation

Chapter 6

Results and discussion

In this section, the results for this Ring of Fire project are presented and discussed. Firstly, a qualitative analysis of the flow topology is performed in Section 6.1, where the wake of the Tiguan and Up are discussed individually and also compared to one another. The flow topology is expressed in the streamwise velocity component, vectors representing the in-plane velocity and an estimation of the vorticity as well as the pressure is shown. Moreover, the turbulence in the form of the standard deviation is calculated and visualised.

In the second part of this Chapter, the drag analysis is discussed in Section 6.2. The drag area coefficients of both cars are presented and their statistical significance is discussed. Moreover, the influence of the momentum and pressure term on the drag is elaborated upon. Lastly, an attempt is made to correlate the flow topology to the respective drag coefficients of the cars in Section 6.3, in a comparative manner.

A limited amount of literature is available on the flow topology in the wake of a passenger car, presumably because car companies keep their designs confidential. Therefore, an attempt is made to compare the processed flow field with the available literature on simplified car models and to the best of the authors knowledge, similarities and differences are highlighted.

Contents

6.1 Flow field analysis

In this Section, the flow field is analysed and a comparison is made between the flow field of the Up and the Tiguan. Firstly, the development of the flow field in streamwise direction is discussed and a direct comparison is made between the Tiguan front closed and the Up at 0.25, 0.50, 0.75, 1, 1.50, 2, 3 and 5 meter in the wake. In this Chapter, the flow fields at 0.25, 0.50, 0.75 and 1 meter are referred to as the near wake and the flow fields at 1.50, 2, 3 and 5 are referred to as far wake. The vorticity fields are included in this discussion and the pressure and turbulence in the form of the standard deviation are also shown. At last, the flow fields of the Tiguan front open and closed are discussed.

The coordinate system used for the flow field analysis is a Cartesian system, where the car moves into the plane, along the z-axis in negative direction. The vertical direction is the y-axis and the lateral direction is the x-axis. The velocity components are defined as u in x-direction, v in y-direction and w in z-direction. For the analysis of the flow fields, ensemble averages are created from several days of testing, after lateral repositioning and proper cropping of the final fields. For the Tiguan with the radiator front closed, many more runs have been acquired than for the Tiguan with the front open (36 runs versus 11 runs). Therefore, the comparison between the Tiguan and the Up (which accumulated a total of 23 good runs over 2 days) is made using the ensemble averaged fields of the front closed measurements. An instantaneous three-dimensional rendering of the velocity isosurfaces in the wake is shown in Figure 6.1 for illustration purposes. Blue represents -33 m/s, green represents -25 m/s and orange represents -14 m/s. It should be noted that during this experiment the car drives in negative z-direction, leading to the negative velocities.

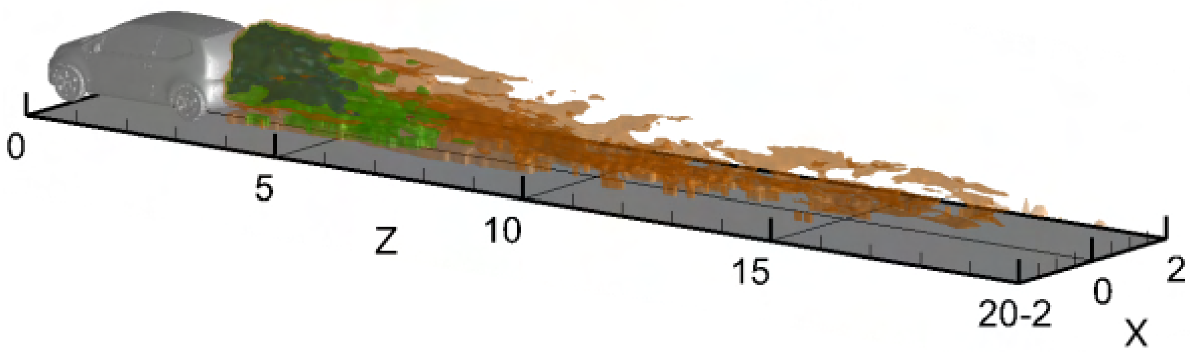

Figure 6.1: Three-dimensional velocity isosurfaces from an instantaneous measurement

The velocity, vorticity, pressure and turbulence are all non-dimensionalized after the velocities have been corrected for the car velocity of 33.33 m/s. The width of the car is the respective width of the Tiguan and Up, as discussed in Chapter 5. For the pressure coefficient, p_∞ represents the ambient pressure value measured during the campaign with a weather measurement system and w_{env} is the averaged streamwise velocity at the inlet plane. The turbulence is expressed in the standard deviation, for which the non-dimensional velocity is used. $w^*_{wake_i}$ is the streamwise non-dimensional velocity of the individual runs, whereas $\overline{w^*_{wake}}$ is the mean of the runs.

$$w^* = \frac{w_{wake} - w_{car}}{w_{car}} \tag{6.1}$$

$$\omega^*_x = \frac{\omega \cdot width_{car}}{w_{car}} \tag{6.2}$$

$$c_p = \frac{p_{wake} - p_\infty}{\frac{1}{2}\rho(w_{env} - w_{car})^2} \tag{6.3}$$

$$\sigma_w^* = \sqrt{\frac{\sum_{i=1}^{n} w_{wake_i}^* - \overline{w_{wake}^*}}{n-1}} \tag{6.4}$$

6.1.1 Streamwise velocity and wake topology

The streamwise velocity contours along with the in-plane velocity vector components are shown in this Subsection. The discussion of these Figures consists of two parts: the evolution of the out-of-plane velocity contour in streamwise direction and the evolution of the in-plane vectors. In this discussion, an attempt to correlate the in-plane vectors with the streamwise wake topology is made. For this analysis, in Figure 6.2 the XY-planes at 0.25, 0.50, 0.75 and 1 meter are shown. The XY-planes at 1.50, 2, 3 and 5 are shown in Figure 6.3. On the left the Volkswagen Up is shown, whereas on the right the Volkswagen Tiguan is shown. Also, silhouettes of these cars are implemented in the Figures to give a clearer visualisation how the wake shapes and develops with respect to the car.

Looking at the near wake velocity vectors, which represent the in-plane velocities, the following can be analysed. First of all, the vector fields at 0.25 and 0.5 meter behind the Up and Tiguan show a very similar pattern. These fields are shown in Figure 6.2a, Figure 6.2b, Figure 6.2c and 6.2d. The air outside the distinct wake region undergoes a clear suction towards the wake, which can be concluded from the velocity vectors outside the wake pointing towards the centre of the wake. For the Up, this suction appears to be slightly stronger on the left and right side of the car at a height of about 0.7 meter. Where the wake shape of the Tiguan stays relatively the same with respect to the car silhouette at this height, the wake of the Up narrows and both on the left and right between y = 0 and y = 0.5 meter, the wake forms a semi-circle. On the contrary, the wake of the Tiguan starts to dilate outward in close proximity to the ground. Secondly, for the vector field inside the wake contour, a clear upwash is visible for both car models. The air is sucked into the wake from the side and from underneath the car, resulting in vectors that move towards the centre of the wake and simultaneously move upwards. For each model, this upward flow moves from the lower side of the car all the way up to about the height of the car and meets the flow getting sucked in the wake from outside. This causes the formation of the wake boundary on the upper side of the wake, where the visualisation of the wake contour shows that the streamwise velocity very rapidly recovers to freestream conditions so close to the car. Additionally, the wake for both cars remains at the same height due to the upwash. Lastly, the vector fields show for both cars the start of the formation of vortices, shown by the circular movement beginning to occur on the left and right of the upwash. These vortices are stretched in the vertical direction, creating an oval shape.
When looking at the vector fields at 0.75 and 1 in the wake, shown in Figure 6.2e, Figure 6.2f, Figure 6.2g and Figure 6.2h, a clear distinction between both cars starts to form. The vector field at 0.75 meter for the Up shows that the downwash from outside the wake enters the wake contour region of the wake, which is stronger than the upwash. Therefore, a downward movement of the velocity vectors occurs which is even more apparent when looking at the velocity field at 1 meter behind the car. Due to this downwash, the wake contour starts to shrink in vertical direction with respect to the car shape. Where at 0.25 and 0.50 meter the wake was still at the same height as the top of the car, at 0.75 and more at 1 meter in the wake the contour starts to shrink, where the largest decrease in height is visualised around x = 0 meter. In contrast to the Up, the upward movement of the flow inside the wake of the Tiguan is stronger than the downward movement of the flow outside the wake and partly counteracts this movement and partly deflects the flow outward.
The wake contour topology up to 1 meter is already quite different between the cars. Firstly, the wake seems to be slightly wider for the Tiguan than for the Up, which may be attributed to the fact that the Tiguan is wider than the Up, therefore causing this difference so close to the car. However, the wake seems to dilate closer to the ground for the Tiguan than for the Up, where the wake more closely follows the contour of the tyres, which already starts to occur at 0.25 meter in the wake. Secondly, the wake of the Up already reached the ground at 0.25 meter, whereas for the Tiguan the two tyres are still separated by a region of low velocity, even up to 1 meter in the wake. This may indicate that the wake of the Up is characterized by a stronger downwash compared to the Tiguan, however this does not explain why the wake already reaches the ground at 0.25 and 0.50 meter, since the Up also shows a clear upwash in this region. Rather, an explanation could be that the floor of the Up is located in closer proximity of the ground compared to the Tiguan. For 0.75 meter and further in the wake, the upwash behind the Tiguan

prevents the wake from moving towards the ground.

When the planes further downstream in the wake are analysed, a clear distinction between the Up and Tiguan takes shape. At 1.50 and 2 meter in the wake of the Up, shown in Figure 6.3a and Figure 6.3c, the upwash becomes stronger and the formation of two counter-rotating vortices starts to shape between y = 0 and y = 0.5 meter, based on the in-plane vectors. Additionally, the wake shrinks in height and dilates outward towards the ground, up to x = -1.0 and x = 1.0 meter. On the contrary, the wake of the Tiguan at 1.50 and 2 meter, shown in Figure 6.3b and Figure 6.3c, does not seem to lose height and two counter-rotating vortices start to take shape, between y = 0.9 and y = 1.4 meter. The suction of the flow into the wake of the Tiguan, together with the flow circulation, causes the formation of a mushroom kind of shape, with a thicker circular part between 1 and 1.5 meter above the ground, a smaller part between 0.6 and 1 meter and below 0.6 meter dilates outward in a triangular manner.
Looking at the fields at 3 and 5 meter in the wake, the Up shows a clear reduction in height, where at 3 meters the wake is still about 1 meter high whereas at 5 meters the wake has shrunk to a height of approximately 0.5 meter and dilated outwards up to x = 1.0 and x = 1.0. This is shown in Figure 6.3e and Figure 6.3g. For the Tiguan, the flow fields at 3 and 5 meter, shown in Figure 6.3f and Figure 6.3h, the wake does not lose height and finally reaches the ground between the wheels at 3 meter in the wake. The mushroom shape becomes even more apparent and the lower part of the wake dilates even further outward with the same triangular shape as analysed before.

For both cars, the lowest non-dimensional velocity reaches a value of -0.25, at a location of 0.50 meter in the wake. This means that the maximum velocity in the wake is about 125% of the car velocity. At 1 meter, the velocity in the wake of the Up reaches a maximum of 110% of the car velocity, as the non-dimensional velocity equals -0.1. At 3 meters, the maximum velocity is between 0.3 and 0.4 and at 5 meters the velocity has been recovered up to about 0.6. For the Tiguan, the velocity at 1m in the wake of the car has a maximum velocity of 120% of the velocity of the car in small regions near the centre of the wake. The non-dimensional velocity reaches a value of -0.2. At 3 meters, the maximum velocity in the wake is about 0.4 and at 5 meters the maximum velocity is about 0.7. This means that within the first 5 meters behind the car the out-of-plane velocity decelerated from -0.2 or -0.1 to about 0.6 or 0.7, meaning that about 80% of the car velocity has been recovered within that range.
For both cars, the centre of the wake contains a region where the normalized velocity is negative. This means that the velocity of the air in the near wake is moving faster than the car itself. Therefore, the flow moves towards the car, which could suggest the presence of a recirculation bubble. Such a regime is widely found in literature, most commonly for standard models such as the Ahmed Body, DrivAer and Mira model, as discussed in Chapter 2.

An interesting conclusion that can be drawn from these images is that from these plots it is suggested that the streamwise velocity component at 0.25 meter in the wake is lower than at 0.50 meter, for the Up as well as for the Tiguan. Since it is the case for both cars, it could be the case that there is a physical reason for this phenomenon. Looking at the streamwise velocity field provided by Sellappan et al., 2018, shown in Figure 2.8, it can be seen that the minimum region of minimum velocity occurs between 0.15 and 0.45 z/H. The Ring of Fire measurements at 0.25 meter behind the Up correspond to 0.17 z/H and to 0.15 z/H for the Tiguan. It is therefore most likely that the measurement plane at 0.25 meter behind the car is at a distance behind the car where the minimum velocity has not been reached yet. At 0.50 meter, or 0.33 z/H for the Up and 0.3 for the Tiguan, the minimum velocity is reached, which is in correspondence to the results from the Tomographic PIV measurements condcuted by Sellappan et al., 2018.

It should be noted however, that most of the measurements for the Up where conducted in the first few days of testing. Due to less clear driving lines during this time and less experience of the driver, a constant shift of at least 10 to 20 centimeter occurred. Hence, the lateral position of the Up inside the field of view is shifted to the left, which is the reason why the Up velocity field is plotted with a limit in x-direction from -1.0 up to 1.5. This also resulted in the wake moving outside of the field of view for distances larger than 5 meter, which is the reason why the velocity fields up to 5 meter are taken into consideration for this analysis. For the Tiguan this was much less an issue and more accurate lateral positions where acquired, resulting in an average lateral position close to the centreline. Therefore, the Tiguan plots could be created with the x-axis from -1.3 to 1.3.

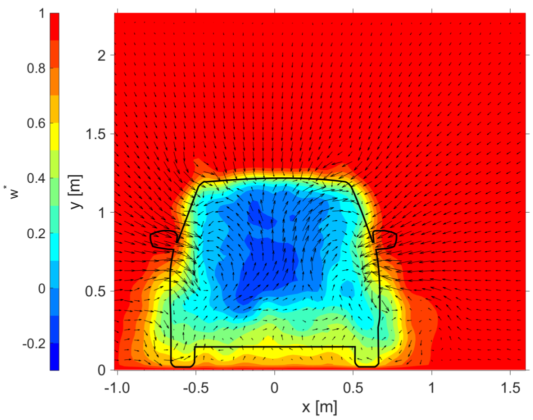

(a) 0.25m in the wake, Up

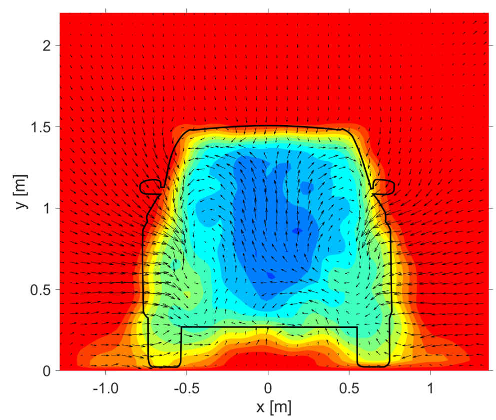

(b) 0.25m in the wake, Tiguan

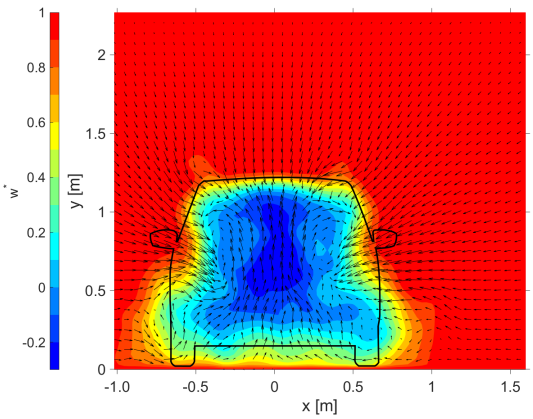

(c) 0.50m in the wake, Up

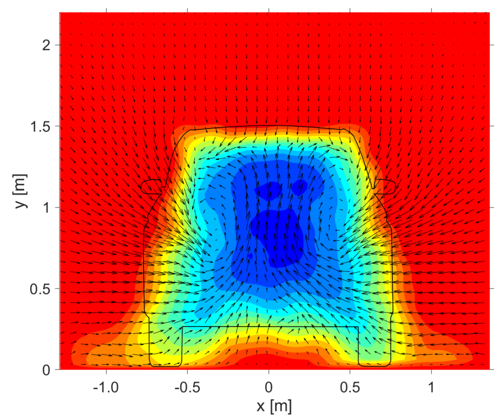

(d) 0.50m in the wake, Tiguan

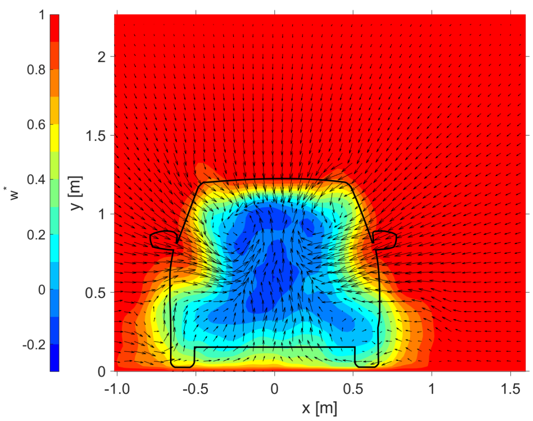

(e) 0.75m in the wake, Up

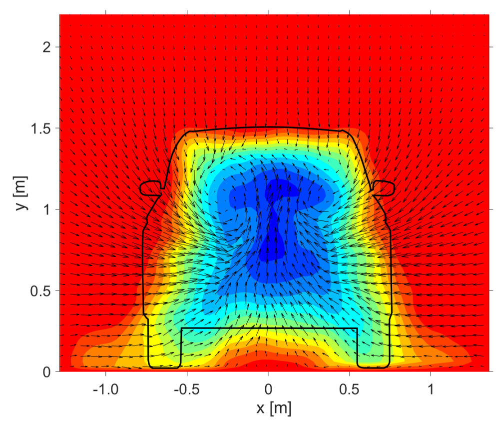

(f) 0.75m in the wake, Tiguan

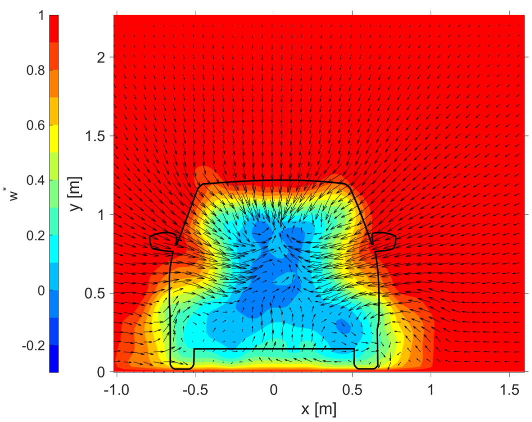

(g) 1m in the wake, Up

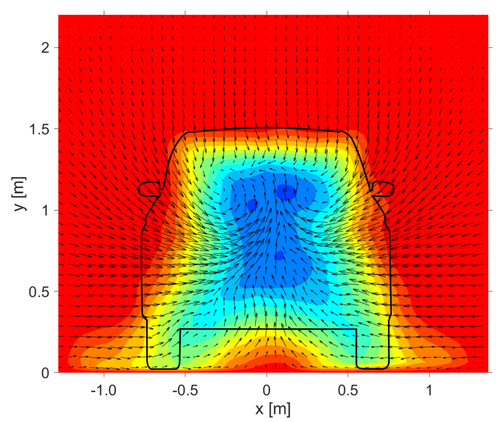

(h) 1m in the wake, Tiguan

Figure 6.2: Comparison of the in-plane velocity vectors with wake contour at 0.25, 0.50, 0.75 and 1 meter

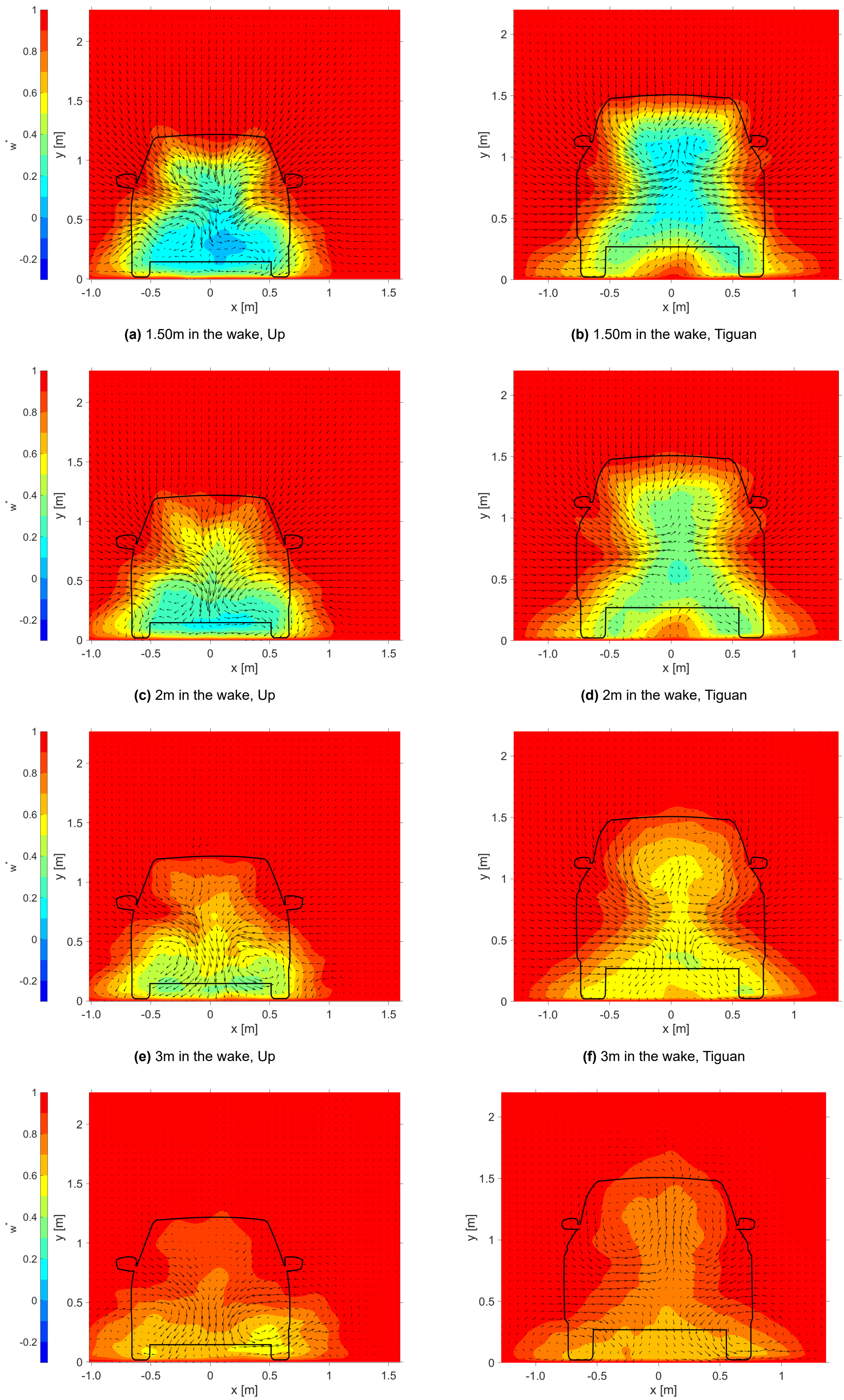

(a) 1.50m in the wake, Up

(b) 1.50m in the wake, Tiguan

(c) 2m in the wake, Up

(d) 2m in the wake, Tiguan

(e) 3m in the wake, Up

(f) 3m in the wake, Tiguan

(g) 5m in the wake, Up

(h) 5m in the wake, Tiguan

Figure 6.3: Comparison of the in-plane velocity vectors with wake contour at 1.50, 2, 3 and 5 meter

6.1.2 Vorticity field comparison

In this Subsection, firstly the vorticity fields at 0.25 meter in the wake of the Up and Tiguan are shown simultaneously with isolines of the λ_2 criterion and Q-criterion, to assess whether the vorticity calculation is sufficient to distinguish shear layers from actual vortices. Secondly, the near wake vorticity fields are analysed and identified vortex structures are discussed. For this analysis, again the vorticity field at 0.25 meter in the wake is used, directly comparing the Up and Tiguan, shown in Figure 6.5. Thirdly, the streamwise evolution of the vorticity in the wake between the Up and Tiguan is compared and discussed. For this comparison, the vorticity at 0.50, 0.75, 1, 1.5, 2, 3 and 5 meter in the wake of the cars is used. Similarly to the previously discussed velocity fields, also for this analysis the ensemble averaged flow is visualised. A red to blue colour bar is used, which is common practice for the display of vorticity. A positive, hence red colour means a counter-clockwise rotation, whereas a negative, hence blue colour means a clockwise rotation. The laterally stretched regions of blue and red colour at the lower border of the vorticity plots are the shear layer on top of the ground in reality, therefore these are ignored in the vorticity analysis.

The vorticity is calculated according to Equation 5.3 and shown in Figure 6.4 using a filled contour plot. The λ_2 criterion for the Up, shown in Figure 6.4a, and Tiguan, shown in Figure 6.4c, are shown through isolines, represented by the dotted line. The Q-criterion is shown in the same manner in Figure 6.4b and Figure 6.4d for the Up and Tiguan, respectively. Isolines for both the λ_2 and Q-criterion are shown for 5% of their respective maximum value at this distance behind the car. The vortices calculated with the vorticity equation are well marked by both the λ_2 criterion as well as the Q-criterion. Hence, it is concluded that the wake largely consists of coherent circulation in streamwise direction and that planar vorticity already suffices in the distinction between shear layers and large scale vortex structures.

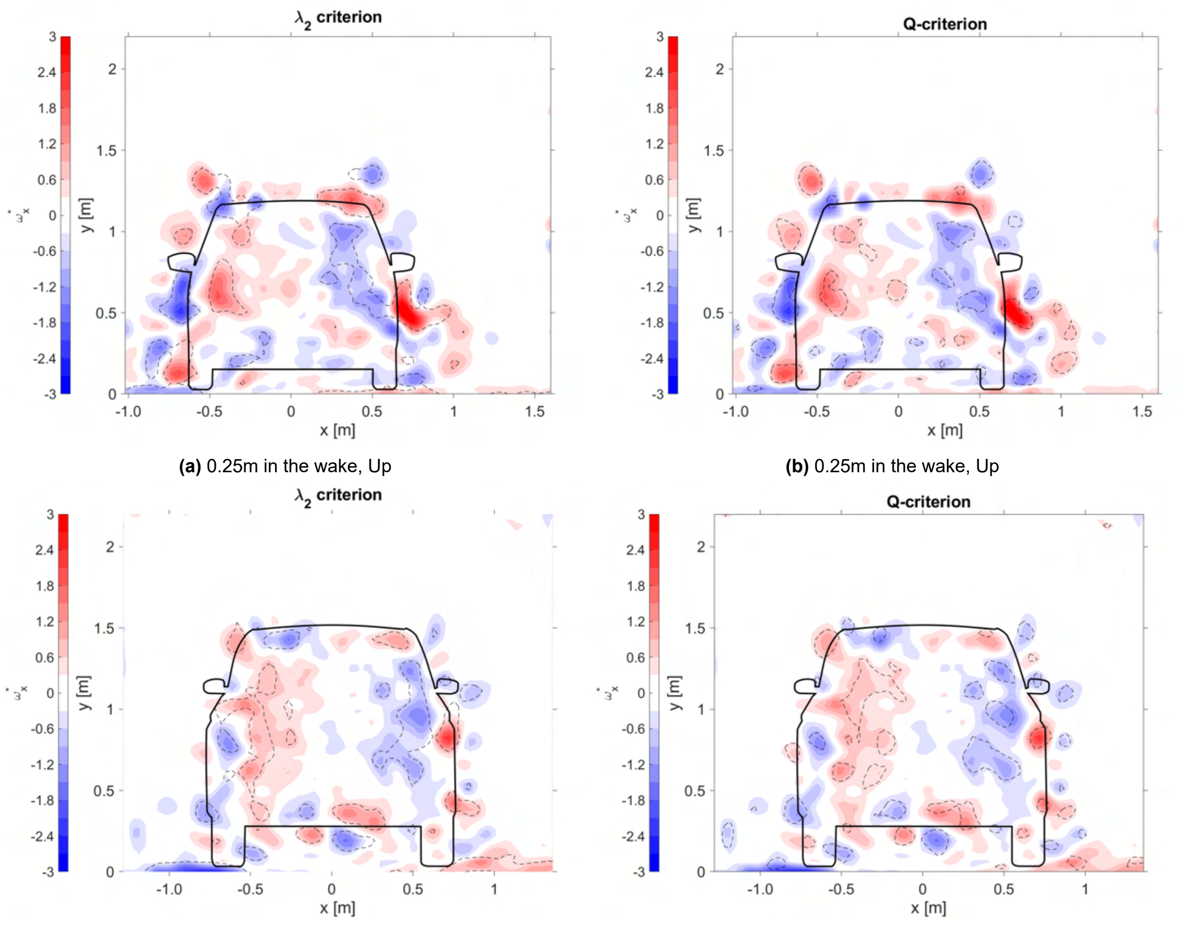

(a) 0.25m in the wake, Up

(b) 0.25m in the wake, Up

(c) 0.25m in the wake, Tiguan

(d) 0.25m in the wake, Tiguan

Figure 6.4: Vortex identification using λ_2 and Q-criterion

Now that the vortices have been established as coherent structures with the aforementioned criteria, the next step is the identification of the different vortices in the near wake. By providing each large scale vortex structure with a letter, a more detailed discussion can be given and their evolution over time is easier visualised. The vorticity field at 0.25 meter for both the Up and Tiguan, including labels for the identified vortices is shown in Figure 6.5.

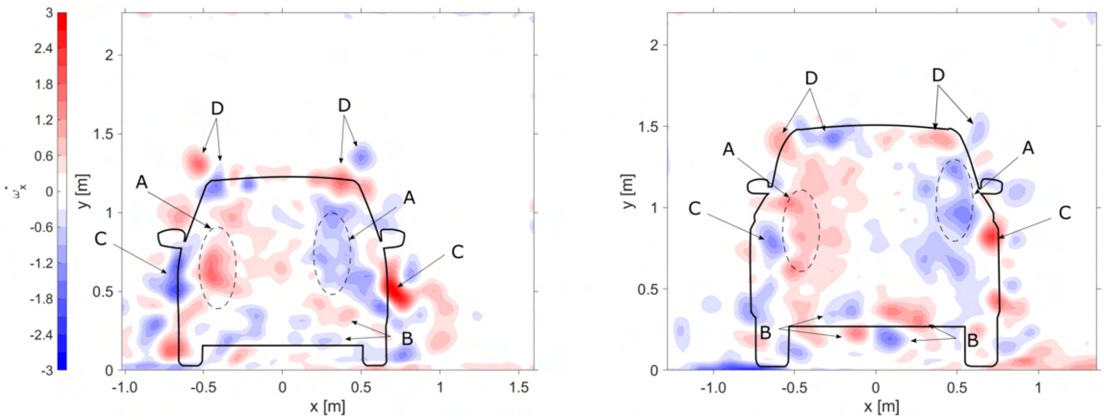

(a) 0.25m in the wake, Up

(b) 0.25m in the wake, Tiguan

Figure 6.5: Identification of the near wake vortex structures for the Up and Tiguan

The vorticity fields show comparable vorticity. A distinction can be made between several vortex pairs, which are indicated by the letters A, B, C and D. Pair A shows two large counter-rotating vortices, shown in Figure 6.5a and Figure 6.5b. The left vortex is positive, where the right vortex is negative and therefore together create the upwash that was previously visualised in the near wake comparison at 0.25 meter behind the cars. This vortex pair is commonly referred to as the A-pillar vortex in the car aerodynamics literature (Ahmed et al., 1984, Venning et al., 2017, Sellappan et al., 2018), which is a result of the formation of the circulation bubble due to the separation of the flow over the back of the car. The second pair of identified vortices is indicated with the letter B. For the Up, only one pair was found, whereas two pairs of vortices were found for the Tiguan. For both the Up and the Tiguan, these vortices show a combination of a clockwise and counter-clockwise vortex located right above each other on the right side of the centerline. For only the Tiguan, on the left of the centerline a counter-clockwise vortex is located right above a clockwise vortex. These vortices are commonly referred to as the B vortical structure (Ahmed et al., 1984, Venning et al., 2017, Sellappan et al., 2018), which are induced by the separation of the flow coming from underneath the car in between the wheels. The third pair of vortices identified are indicated with C. Both vortices of pair C are located to the outer side of vortex pair A. For the Up, these vortices are much stronger than the A vortices and for the Tiguan these are somewhat stronger, especially the C vortex on the right. These vortices are commonly referred to as the C-pillar vortices in car aerodynamics literature (Ahmed et al., 1984, Venning et al., 2017, Sellappan et al., 2018), and are a result of the roll up of the shear layer over the side of the car. The last vortex pair identified is indicated with D. This pair consists of two combinations of a positive and negative vortex. To the best knowledge of the author, only X. W. Wang et al., 2013 refers to these vortices. They suggest that these could be a result of the partly separation of the shear layer over the top surface of the car. This slight overshoot in horizontal, streamwise direction results in the formation of vortices. X. W. Wang et al., 2013 suggest that these vortices are a result of the rolling effect of the C-vortices, but when looking at Figure 6.5a and Figure 6.5b, these vortices are located too low to interact with the shear layer. Perhaps, an interaction of the shear layer with the A vortices results in these vortices. Another explanation could be that these vortices result from interaction of the flow over the front window with the car structure on the left and right of the front window. As shown in Figure 4.8a and Figure 4.8b, the window is slightly lower compared to the car structure that it is attached to. Nonetheless, additional information could not be found in literature and the aforementioned reasoning is merely based on observations.

Next, the streamwise vorticity development of the Up and Tiguan is visualised in Figure 6.6. Firstly, the Up will be analysed and discussed. The near wake vorticity at 0.50, 0.75, 1 and 1.50 meter are discussed first and are shown in Figure 6.6a, Figure 6.6c, Figure 6.6e and Figure 6.6g, respectively. The vorticity field at 0.50 meter shows a similar structure compared to the field at 0.25 meter. It appears however, that the previously defined C vortex on the right is very weak and not clearly displayed, which could be caused by an inaccurate ensemble averaging. Looking at the fields at 0.75 meter and 1 meter, it appears as though the C vortex starts to shift from next to the A vortex to underneath the A vortex. Moreover, whereas the C vortex appears to become larger, the A vortex reduces in size. This is even more apparent in the vorticity at 1.50, where the C vortices become dominant vortex and the A vortices weaken.

The velocity fields at 2, 3 and 5 meter are shown in Figure 6.7a, Figure 6.7c and Figure 6.7e. At 2 meter, the A vortices have shrunk to two small vortices, whereas the C vortices have grown to two larger vortices and are located right below the A vortices. At 3 meter, only the left A vortex can still be slightly distinguished, whereas the right A vortex has disappeared. The C vortices remain the strong vortex pair comparable to the vortices at 2 meter, causing the downwash in the wake. At 5 meter in the wake, only those two lower vortices remain. The explanation for these two vortices most in line with the aforementioned vortex evolution is that these are the C vortices and the A vortices have disappeared as these were weaker. Nonetheless, it could be the case that the lower vortex pair B has merged with the C vortex, strengthening this vortex and also contributing to its growth.

Comparing the evolution of the averaged vortex evolution in the wake of the Up with the averaged velocity field, it can be concluded that the upwash previously described in the wake of the up at 0.25 and 0.50 meter is due to the large A vortices, which cause the flow to be directed upwards. Moreover, the A vortices start to disappear downstream whereas the C vortices gain strength and become larger, eventually starting to become the dominant vortices. Since these vortices are in the opposite direction of the A vortices, the upwash in the near wake transits into a downwash between 1 and 1.50 meter behind the car. An explanation for this transition could be that for the Up, the A vortex gains its strength from the recirculation bubble formed in the near wake of the car. This means that the A vortex is at its strongest when the circulation bubbles is at its largest, which is right behind the car and weakens when the bubble become smaller, which is evidently the case moving further downstream. Contrary, the C vortices gain strength moving downstream, potentially due to a merge with the smaller B vortices coming from underneath the car. Eventually, only the C vortices are still maintained at 5 meter in the wake, and have also severely weakened compared to the vortices at 1.50 and 2 meter. As discussed, the downwash generated by these vortices together with the ground cause the wake to shrink in vertical direction, which was shown before in Figure 6.3g. Moreover, the flow is directed in lateral direction due to these vortices, causing the outward expansion of the wake.

The streamwise development of the vorticity of the Tiguan is shown in Figure 6.6 on the right. At 0.50 meter, the wake is still similar to the wake of the Up, where the difference can be observed that the C vortices are weaker and the A vortices are stronger compared to the Up. Additionally, the D vortices are weaker as well and less well defined and distinguishable compared to the Up. The vortices are located approximately 20 cm higher than those of the Up, which is ascribed to the fact that the height of the Tiguan differs with the same distance compared to the height of the Up. Looking at the vorticity fields at 0.75, 1 and 1.50 meter in the wake, in Figure 6.6d, Figure 6.6f and Figure 6.6h, the A vortices do not seem to lose much strength and size, whereas they also remain at the same location in lateral and vertical direction. Additionally, the C vortices are not easily identified at 0.75 and 1 meter, which could mean that they merge together with the B vortices at this distance to eventually form the pair of lower vortices shown at 1.50 meter. At this distance, the A vortices have somewhat decreased in size, with a more dense vortex and consequently stronger vortex centre located at $y = 1$ meter and at $x = -0.2$ meter and $x = 0.2$ meter. These vortices cause the upwash that was already visualised and discussed by showing the in-plane velocity vectors in Figure 6.3b, due to the clockwise circulation of the right vortex and the counter-clockwise circulation of the left vortex. Underneath this pair of counter-rotating vortices, the combination of the C and B vortices, referred to as the BC vortex, also show a pair of counter-rotating vortices, which rotate in opposite direction compared to the pair of A vortices. At 2, 3 and 5 meter in the wake, shown in Figure 6.7 on the right, this division in 4 different vortices maintains, but their strength further downstream decreases. Moreover, it can be seen that the upper vortex pair remains at its position, barely moving in lateral and vertical direction. On the contrary, the lower vortex pair seems to dilate outward in lateral direction and also loses about 20 to 30 cm in height. The dilation of these vortices cause the expansion of the wake in the somewhat triangular shape of the wake below y = 0.5 meter visualised in Figure 6.3h. Additionally, a counter-rotating motion of the right vortex of the upper pair with respect to the right vortex of the lower pair is established, which is also the case for the left vortices. This motion causes the wake to be directed inward at approximately y = 0.7 meter, resulting in the previously described mushroom-like shape of the wake contour.

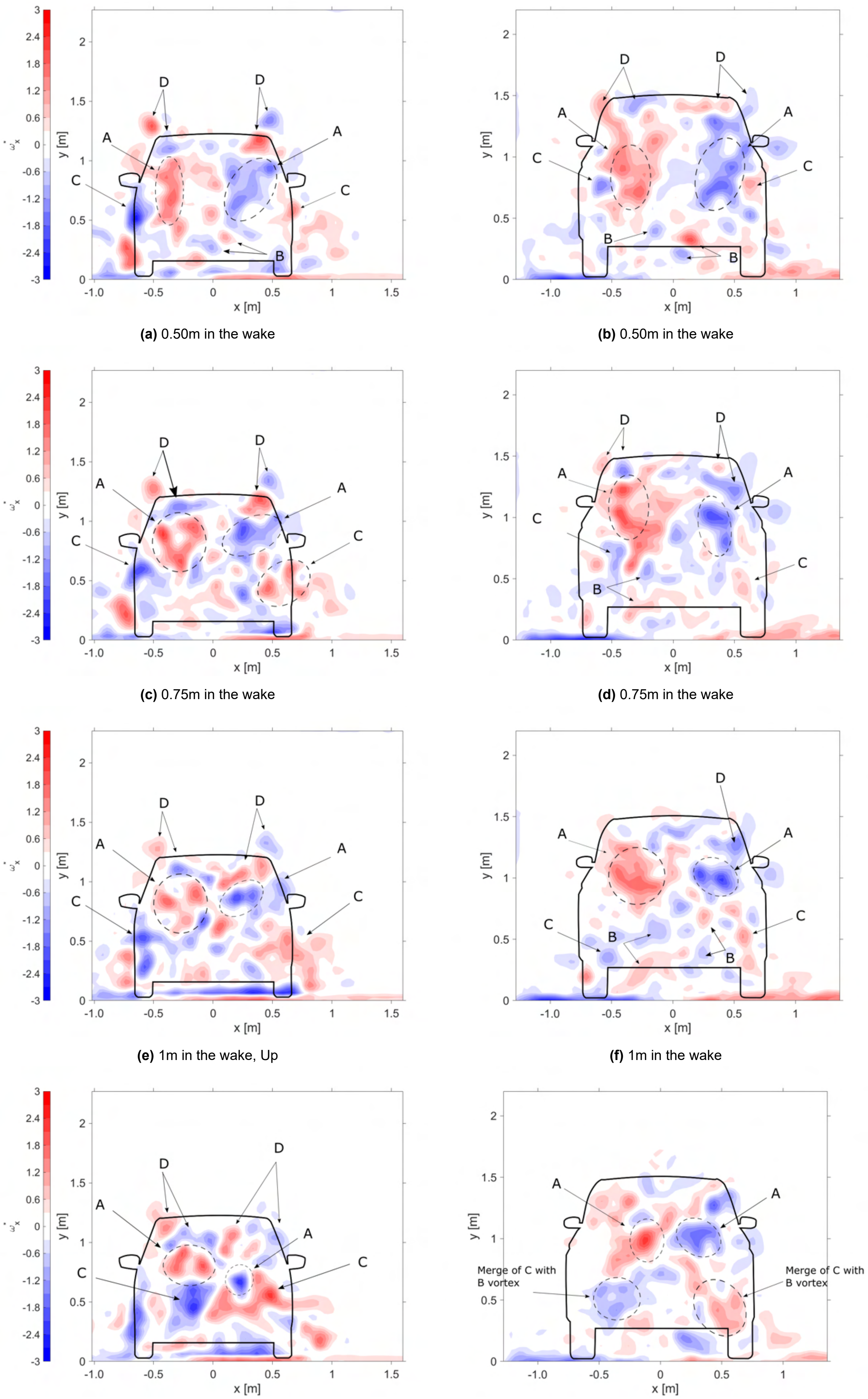

(a) 0.50m in the wake

(b) 0.50m in the wake

(c) 0.75m in the wake

(d) 0.75m in the wake

(e) 1m in the wake, Up

(f) 1m in the wake

(g) 1.50m in the wake

(h) 1.50m in the wake

Figure 6.6: Streamwise vorticity comparison between the Up and Tiguan at 0.50, 0.75, 1.0 and 1.5 meter

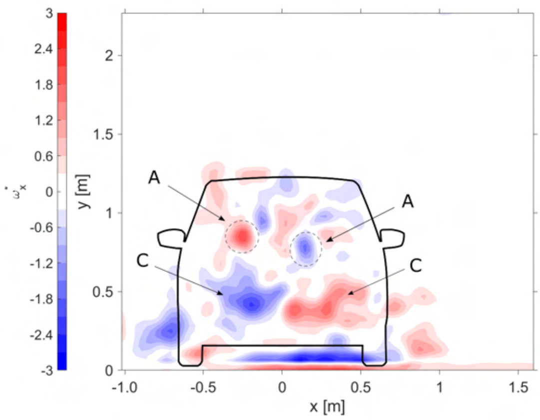

(a) 2m in the wake

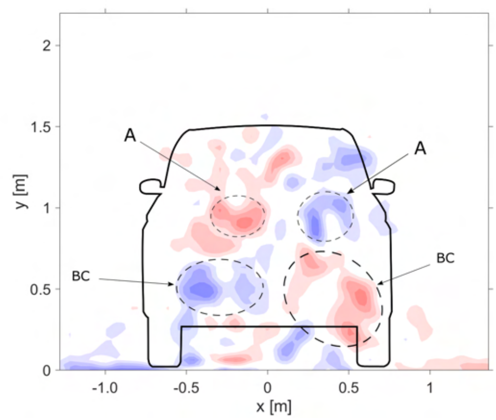

(b) 2m in the wake

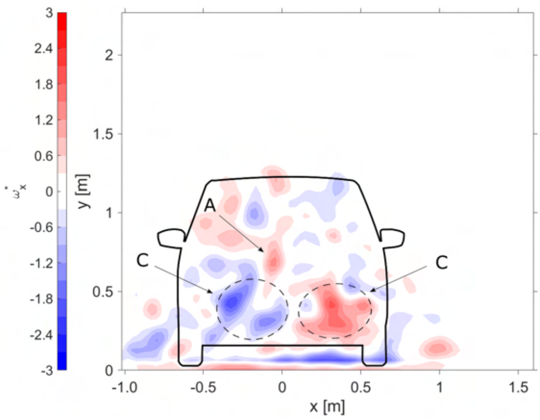

(c) 3m in the wake

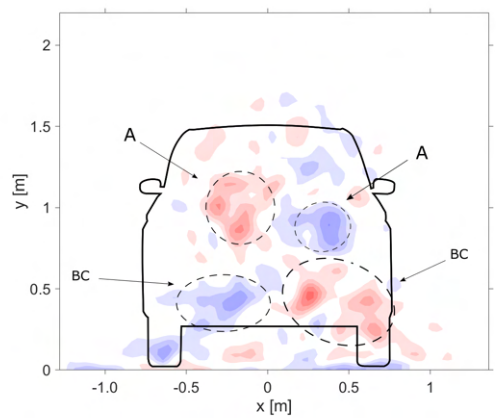

(d) 3m in the wake

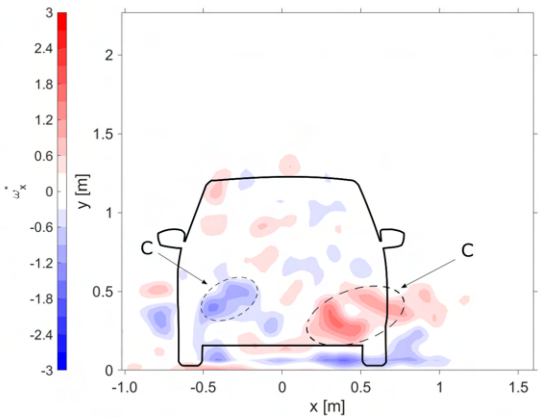

(e) 5m in the wake

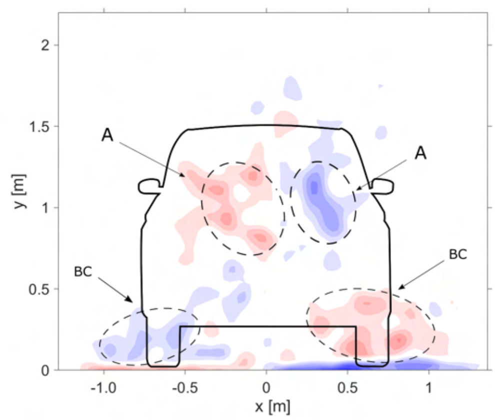

(f) 5m in the wake

Figure 6.7: Streamwise vorticity comparison between the Up and Tiguan at 2, 3 and 5 meter

6.1.3 Pressure field comparison

In addition to the out-of-plane velocity, in-plane velocity vectors and vorticity, the pressure field is also used to analyse and discuss the main flow features in the wake of the Up and the Tiguan. The pressure coefficient is plotted for the Up in Figure 6.8 on the left at distances 0.25, 0.50, 0.75, and 1 meter. For the Tiguan, the same distances are plotted on the right in this Figure. The pressure fields at 1.50, 2, 3 and 5 are shown in 6.9, again with the Up on the left and Tiguan on the right.

In general, it can be seen that the pressure is lowest inside the wake and gradually increases, which is attributed to pressure losses occurring in the wake of the car. Consequently, the pressure recovers to the environmental pressure at the edge of the wake. Moreover, in general it should be noted that the lowest pressure coefficient is about -0.085 for the Up and -0.095 for the Tiguan, whereas the velocity deficit is up to -1.2 times the freestream velocity. This means that it can be expected that the velocity, hence momentum deficit is the main contributor to the drag force, whereas the pressure has much less influence. This finding is in line with the reasoning behind the drag calculations established in Chapter 3.

The pressure coefficient plot at 0.25 meter of the Up, Figure 6.8a, shows that the minimum pressure regions are located at x = 0.7 meter, x = -0.7 meter and y = 0.6 meter. This is in correspondence with the location of the C vortices defined in the vorticity field at this distance, shown in Figure 6.5a. The minimum cp value found at this distance is -0.064. Most of the wake corresponds to a pressure coefficient between -0.01 and -0.02, where two separate large regions of cp between -0.02 and -0.03 are shown in yellow. The lowest pressure value is found at 0.50 meter in Figure 6.8c, where the right C vortex is characterised by cp = -0.08. Further downstream, at 0.75 and 1 meter in 6.8e and 6.8g, the area of lower pressure reflected in the green and light blue colour first grows and shapes in a upside down U-shape.
In Figure 6.9a, the pressure field shows two clear low pressure regions, representing the left and right C vortex, which have moved towards the centre from the left and right side of the car. In the pressure field at 2 meter, shown in 6.9c, the pressure contour has shrunk from y = 1.5 meter to y = 1.25 meter. The right vortex is again characterised by small circle of low pressure, at x = 0.45 meter and y = 0.45. Interestingly enough, the left vortex core is not visualised in this plot. This is also seen in the pressure field at 3 meter, where the right vortex has grown in size and lost part of its strength, and the left vortex is slightly visualised by the green area around x = -0.5 meter and y = 0.3 meter. At 5 meter, two relatively low pressure regions remain, showing the weakened C vortex pair.

Lastly, it should be noted that due to the large offset that occurred at several runs for the Up, the pressure field had to be laterally corrected. Therefore, the contour of the pressure field is partly cut, which is for nearly all pressure fields the case on the left side. This means that the Neumann boundary conditions used for the calculation of the pressure are not justified, as the change in pressure normal to the left and right boundary is not equal to 0. Therefore, the pressure fields may contain some errors but for this project, where the main focus lies on the identification of the general large wake structures, this is assumed to be negligible.

The pressure fields for the Tiguan are visualised in Figure 6.8 on the right. At 0.25 meter, the pressure field is quite similar to the Up, where two main longitudinally stretched lower pressure regions are found with a cp of approximately -0.045, and in the middle a higher pressure region. At 0.50 meter, two larger low pressure regions are identified at x = -0.5 and x = 0.5, for y = 1. As shown in the vorticity plot, Figure 6.6a, at this distance the two upper vortices start to form and their strength increases. This is more evidently visible at 0.75 meter and 1 meter. At 0.75 meter, the vortex cores of the upper two counter-rotating vortices are identified by two low pressure regions, where the cp is -0.075 at the centre of the right vortex and -0.084 for the left vortex. The pressure becomes even lower in those regions at a distance of x = 1 meter, where the left vortex can be identified by a low pressure region where the cp becomes - 0.096 and the right vortex can be identified by a low pressure region where the cp becomes -0.085. Moreover, only the upper region of vorticity is can be related to a low pressure region, whereas the vorticity below 0.6 meter does not create low pressure regions.
Further downstream, the pressure starts recovering and the cp value increases again. However, the region of lower pressure starts expanding downward in vertical direction, where the two lower vortices start to form, which is also visualised in the vorticity plots at 1.50 meter and 2 meter in Figure 6.6h and Figure 6.7b. At 3 meter, 3 lower pressure regions can be distinguished, which represent the upper left and right vortices, as well as the lower right vortex. The lower left vortex is not identified, which may be caused by the rather large increase in steps for the colours. Also for the vorticity plots, the lower right vortex shows to be somewhat stronger than the left. At 5 meter, these 3 vortices are well defined as well, where the lower left vortex is also somewhat apparent.

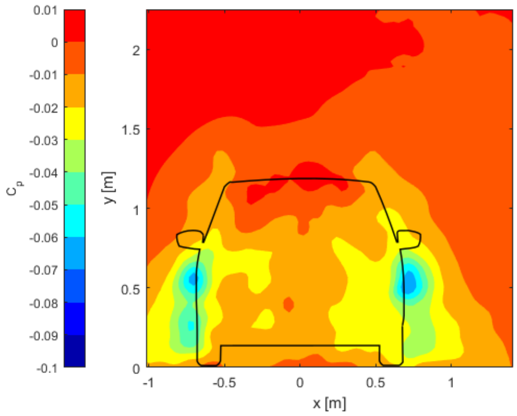

(a) 0.25m

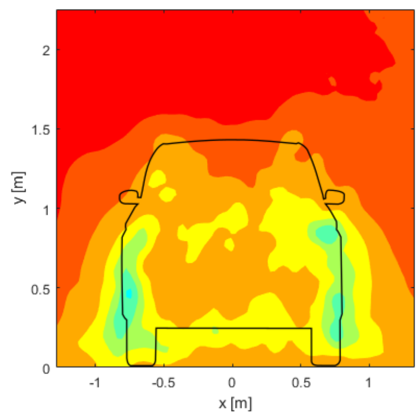

(b) 0.25m

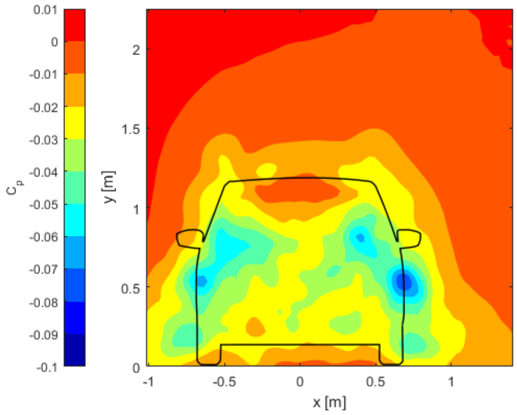

(c) 0.50m

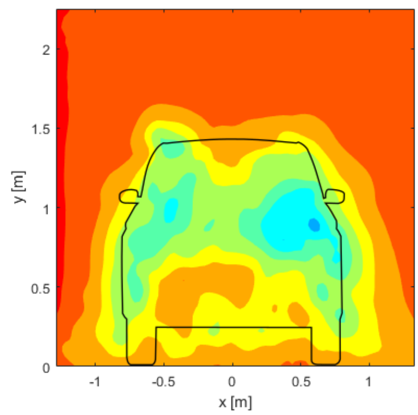

(d) 0.50m

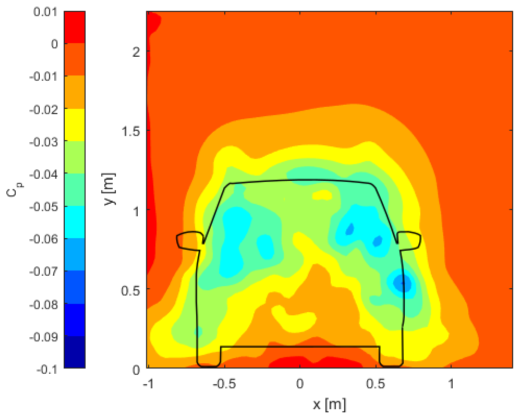

(e) 0.75m

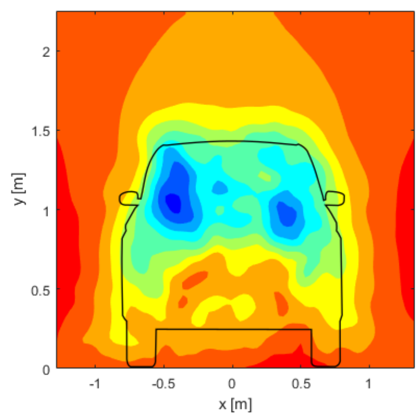

(f) 0.75m

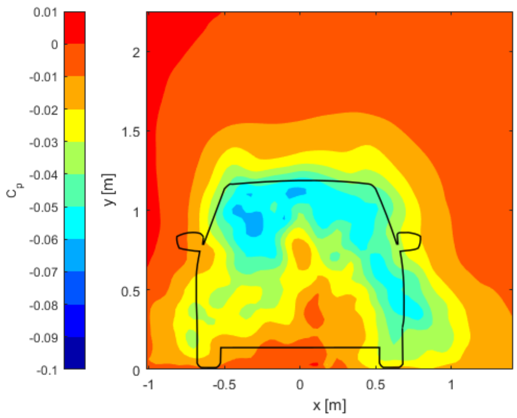

(g) 1m

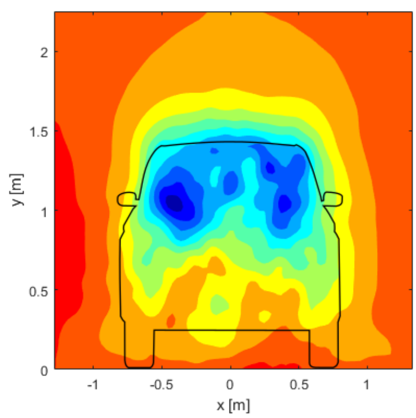

(h) 1m

Figure 6.8: Streamwise pressure field comparison between Up (left) and Tiguan (right)

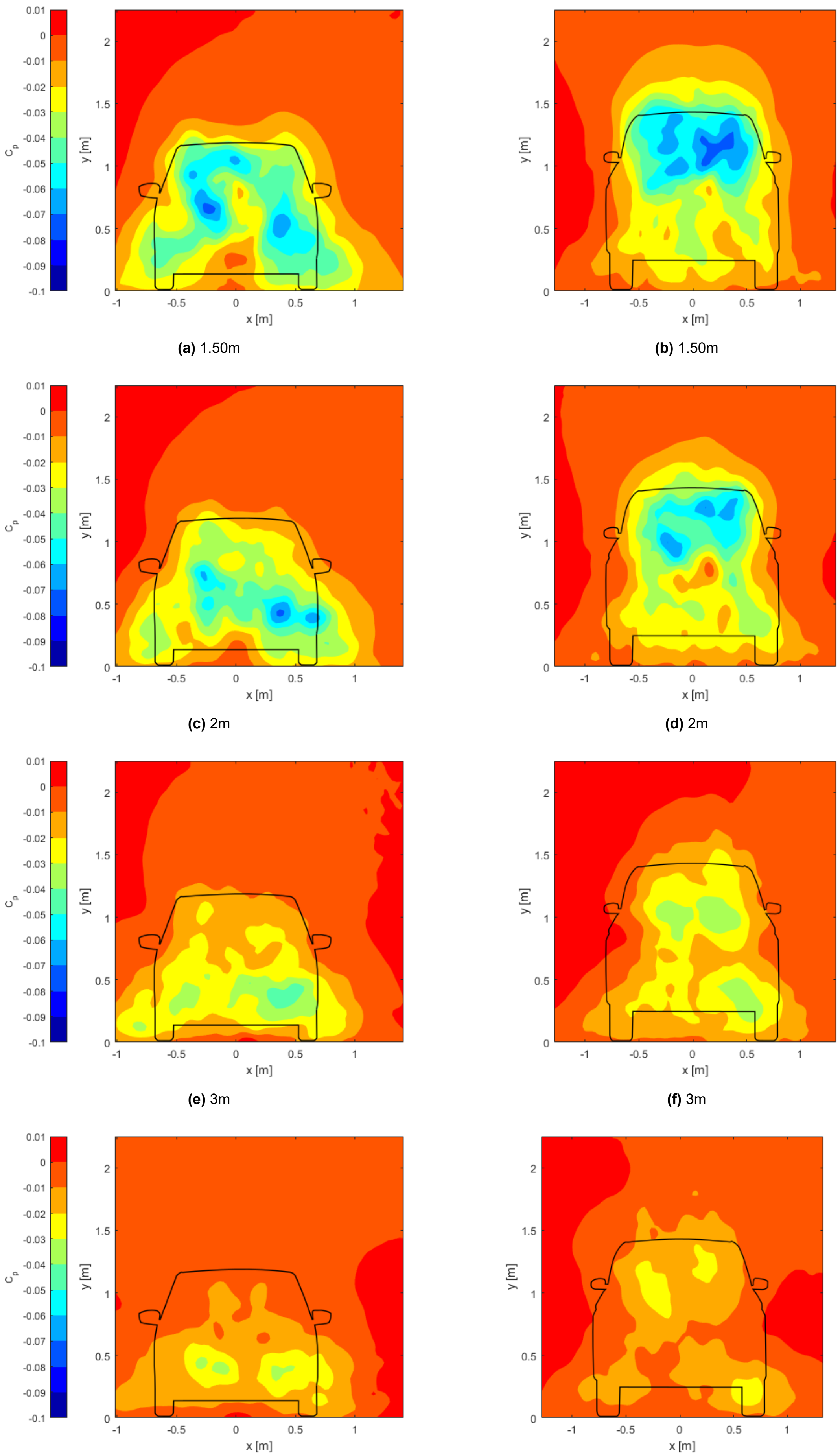

(a) 1.50m **(b)** 1.50m

(c) 2m **(d)** 2m

(e) 3m **(f)** 3m

(g) 5m **(h)** 5m

Figure 6.9: Streamwise far wake pressure field comparison between Up (left) and Tiguan (right)

For an additional quantitative comparison between the pressure in the wake of the Up and Tiguan, line plots are created in which the pressure coefficient values are plotted along the lateral direction of the car, at y = 0.5 and 1 meter. These values were chosen since the lowest pressure values for the Up are measured at the former height, whereas the lowest pressure values for the Tiguan are measured at the latter height. The plots are shown in Figure 6.10.
First of all, the general trend of lower pressure for the Up at y = 0.5 meter and for the Tiguan at y = 1.0 meter is well represented. The Up has a lower pressure compared to the Tiguan at all distances behind the car at a height of 0.5 meter, whereas the Tiguan has a lower pressure at a height of 1 meter. Moreover, it is interesting to see that the lower pressure regions for both cars are located around the same lateral direction. Since the Tiguan is wider than the Up, it may be expected that the low pressure peaks would be more outward for the Tiguan, but it appears that they are quite similar for both cars. It should be noted that the difference in width is only 21 cm, hence it can be argued whether this Ring of Fire project is capable of giving an accurate representation of such small differences. Nonetheless, the low pressure peaks do correlate well with the previously shown vortices, especially of the A and C vortex pairs, meaning that low pressure peaks in the near wake of a car can be used as an indicator where one may expect the vortex cores to be located.

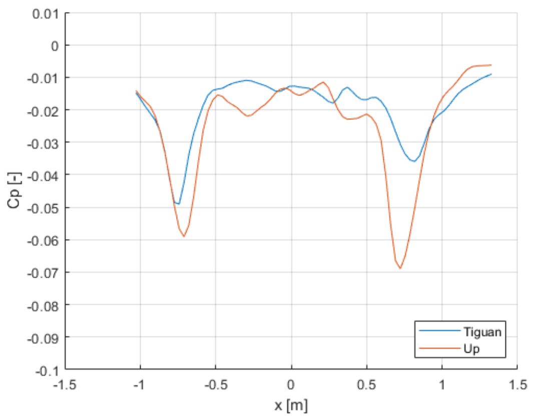

(a) 0.25m in the wake, y = 0.5m

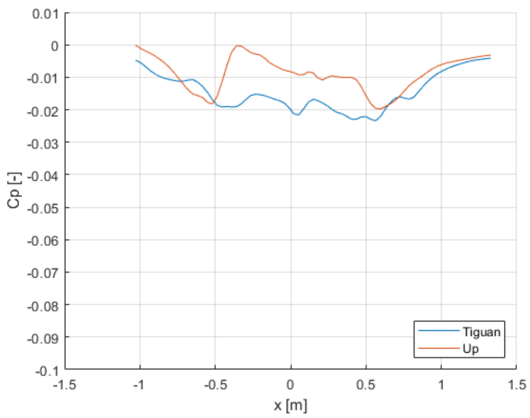

(b) 0.25m in the wake, y = 1m

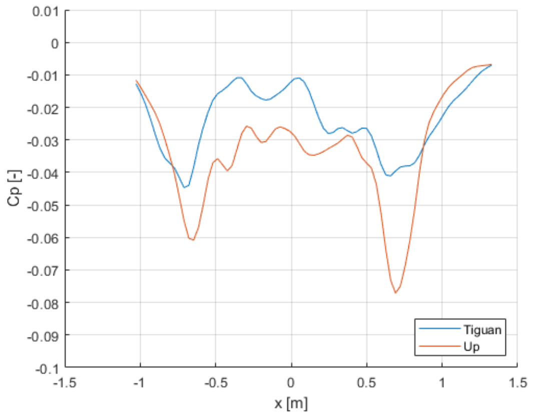

(c) 0.5m in the wake, y = 0.5m

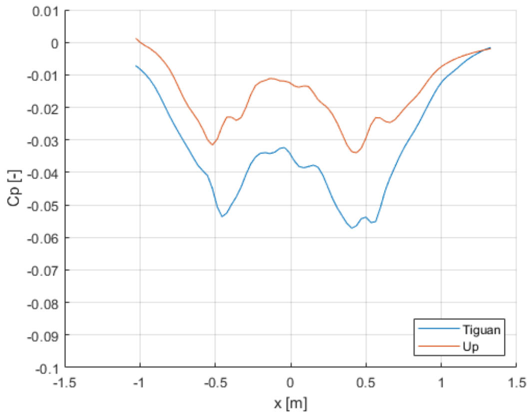

(d) 0.5m in the wake, y = 1m

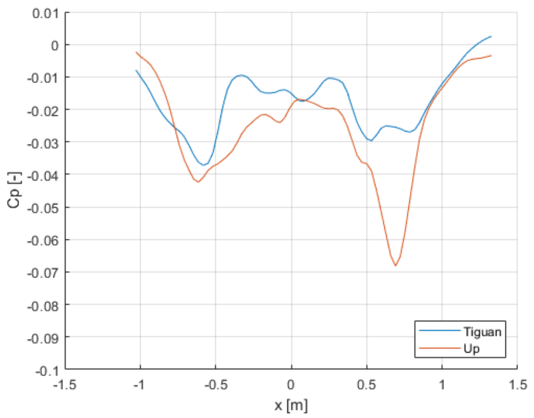

(e) 0.75m in the wake, y = 0.5m

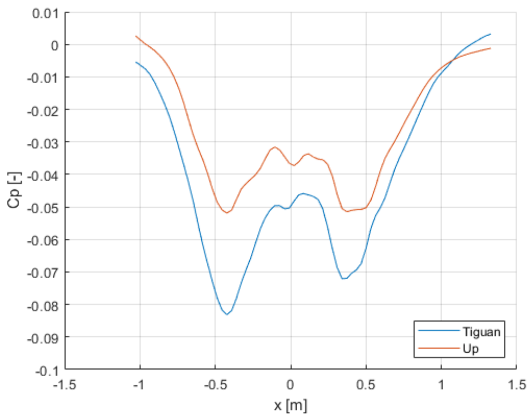

(f) 0.75m in the wake, y = 1m

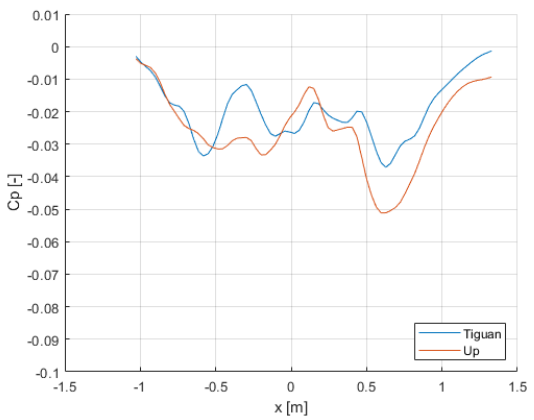

(g) 1m in the wake, y = 0.5m

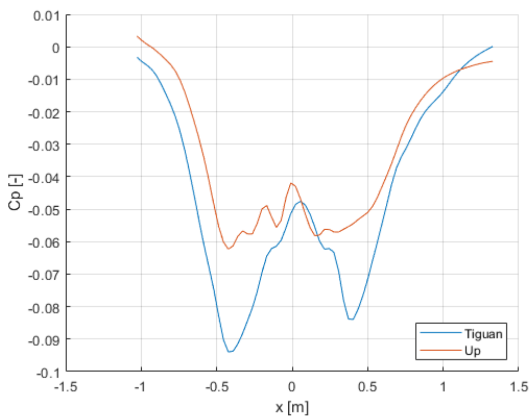

(h) 1m in the wake, y = 1m

Figure 6.10: Quantitative visualisation of pressure distribution in lateral direction at y = 0.5 and 1 meter

6.1.4 Turbulence field comparison

The last flow field variable that is analysed is the turbulence in the out-of-plane velocity component. During standard wind tunnel tests, the turbulence can be measured by taking a plane at a specified distance behind the object and measuring the change in flow over time at that location. However, for the Ring of Fire project, every measurement only provides one instantaneous flow field at a certain distances. Therefore, to measure the turbulence, the standard deviation is taken of the instantaneous out-of-plane velocity component at specified distances in the wake. Moreover, the standard deviation has been calculated using the non-dimensional velocities, to provide a proper comparison in line with the previously discussed non-dimensional flow quantities.

The fluctuations in the wake of the Up and Tiguan, in the form of the non-dimensional standard deviation are shown in Figure 6.11 and Figure 6.12. The highest fluctuations are visible at 0.25 meter in the wake, where the non-dimensional standard deviation reaches a value of 0.37 for the Up and 0.36 for the Tiguan. Fluctuations therefore reach values up to 37% of the car velocity for the Up and 36% of the Tiguan. The freestream turbulence values are smaller than 0.05, resulting in a turbulence intensity in the freestream of approximately 5%.

The fluctuations inside the wake decrease in magnitude further downstream. The general size of the fluctuation contour appears to be larger than the averaged wake contour of the Up and Tiguan. It should be noted however that the colour scheme is slightly coarser for the expression of the turbulence compared to the averaged velocity. Moreover, due to the slight inaccuracy in the lateral repositioning procedure of the instantaneous measurements, the fluctuations may be broader in width than it is the case in reality.

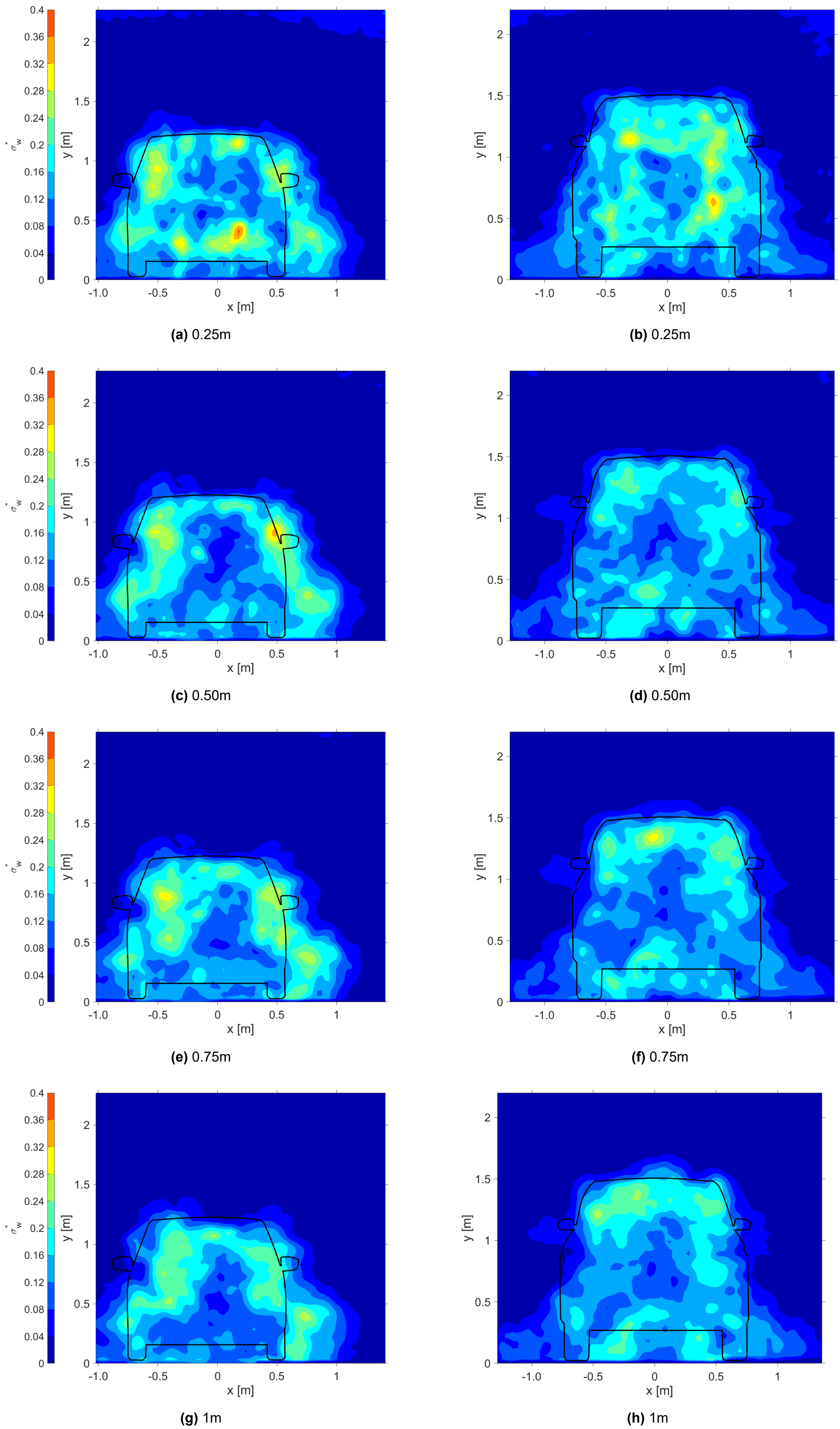

Figure 6.11: Streamwise near wake turbulence field topology comparison between Up (left) and Tiguan (right)

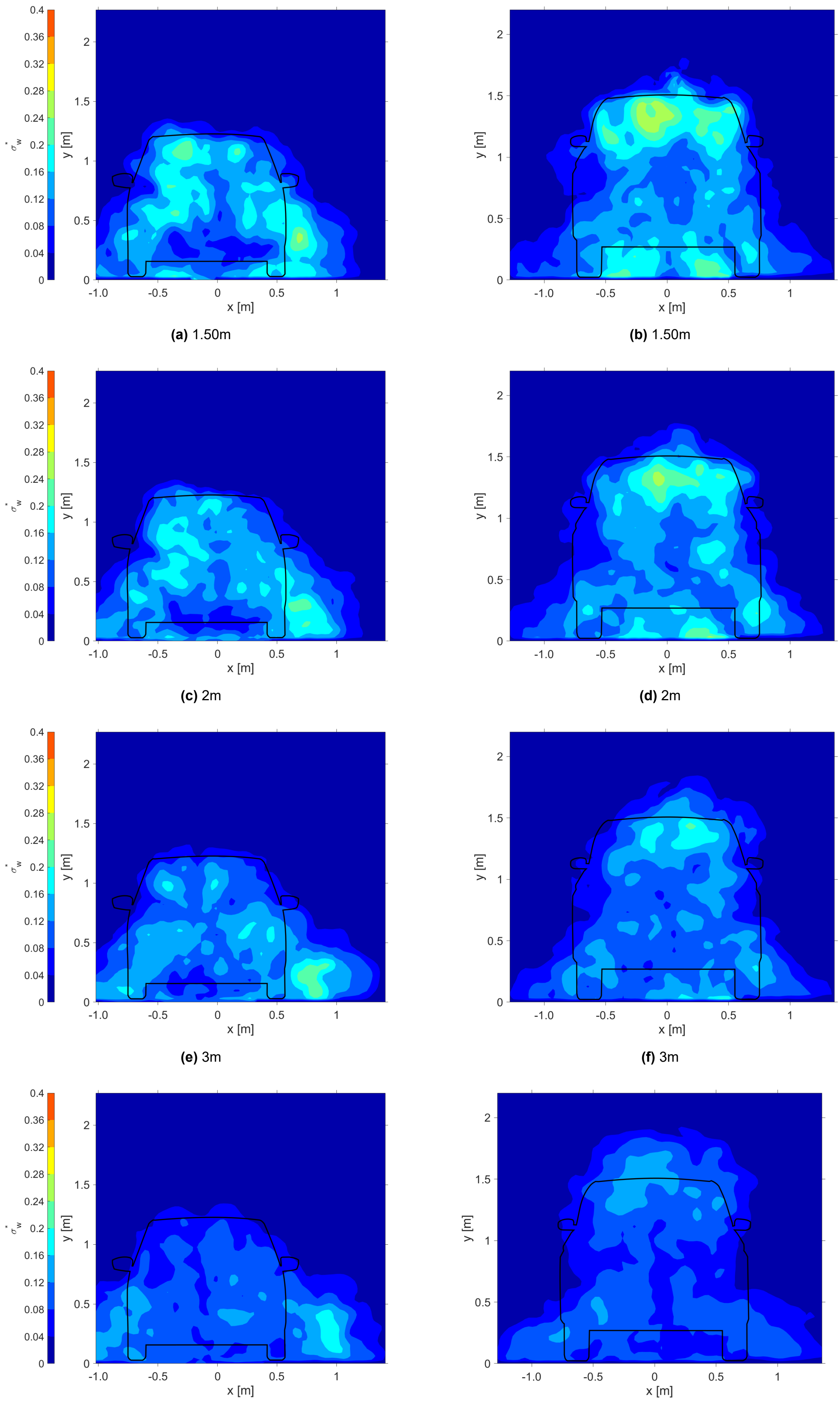

(a) 1.50m **(b)** 1.50m

(c) 2m **(d)** 2m

(e) 3m **(f)** 3m

(g) 5m **(h)** 5m

Figure 6.12: Streamwise far wake turbulence field topology comparison between Up (left) and Tiguan (right)

6.1.5 Comparison between Tiguan radiator front open and closed

Next to the comparison between the Tiguan front closed configuration and the Up, a comparison between the two different Tiguan configurations, one with the front of the radiator closed and one with the front of the radiator open, is made. This comparison is made to analyse whether the Ring of Fire at this stage of development is capable of showing small differences in flow topology due to a slight model modification. The comparison between the two Tiguan configurations is shown in Figure 6.13. On the left, the Tiguan front closed is shown and on the right the Tiguan front open is shown. Only one distance in the wake is chosen (2 meter) since additional figures did not show more insights in flow topology differences and to prevent superfluous data being displayed, only one distance in the wake is chosen.

As discussed in the introduction of this chapter, the number of runs of the Tiguan open configuration is very limited, being about a quarter of the runs used for the Tiguan closed configuration. Therefore, one can see that the averaged flow fields still show quite some instantaneous characteristics, instead of the smoother flow field characteristics shown for the Tiguan front closed, shown in Figure 6.13a and Figure 6.13b. This is also quantitatively shown through the plots of the turbulence, shown in Figure 6.13e and Figure 6.13f. The turbulence in the Tiguan open configuration (up to 35% of the car velocity) is much higher than the turbulence in the Tiguan closed configuration (up to 20% of the car velocity) and the regions of with high turbulence are much larger. One cause for this could be the much lower number of runs, increasing the standard deviation from the mean. Another cause for this could be that it was noticed that during the measurements with the Tiguan front open, especially on the 16th of September, a higher wind velocity occurred, causing a larger variance in spread of the wake contour.
Lastly, the vorticity plot for the Tiguan closed shows a clear distinction between the four main vortices behind the car, whereas the Tiguan front open shows many, likely uncorrelated vortices in the wake, without a clear pattern. The Tiguan open configuration shows stronger vortices than the Tiguan closed configuration, which can possibly also be traced back to the higher in-plane velocities as apparent from the velocity fields, leading to larger in-plane velocity tensors.

Therefore, it is most probable that due to an insufficient number of good runs and environmental fluctuations, in this Ring of Fire project a distinction between two slightly different configurations cannot be established.

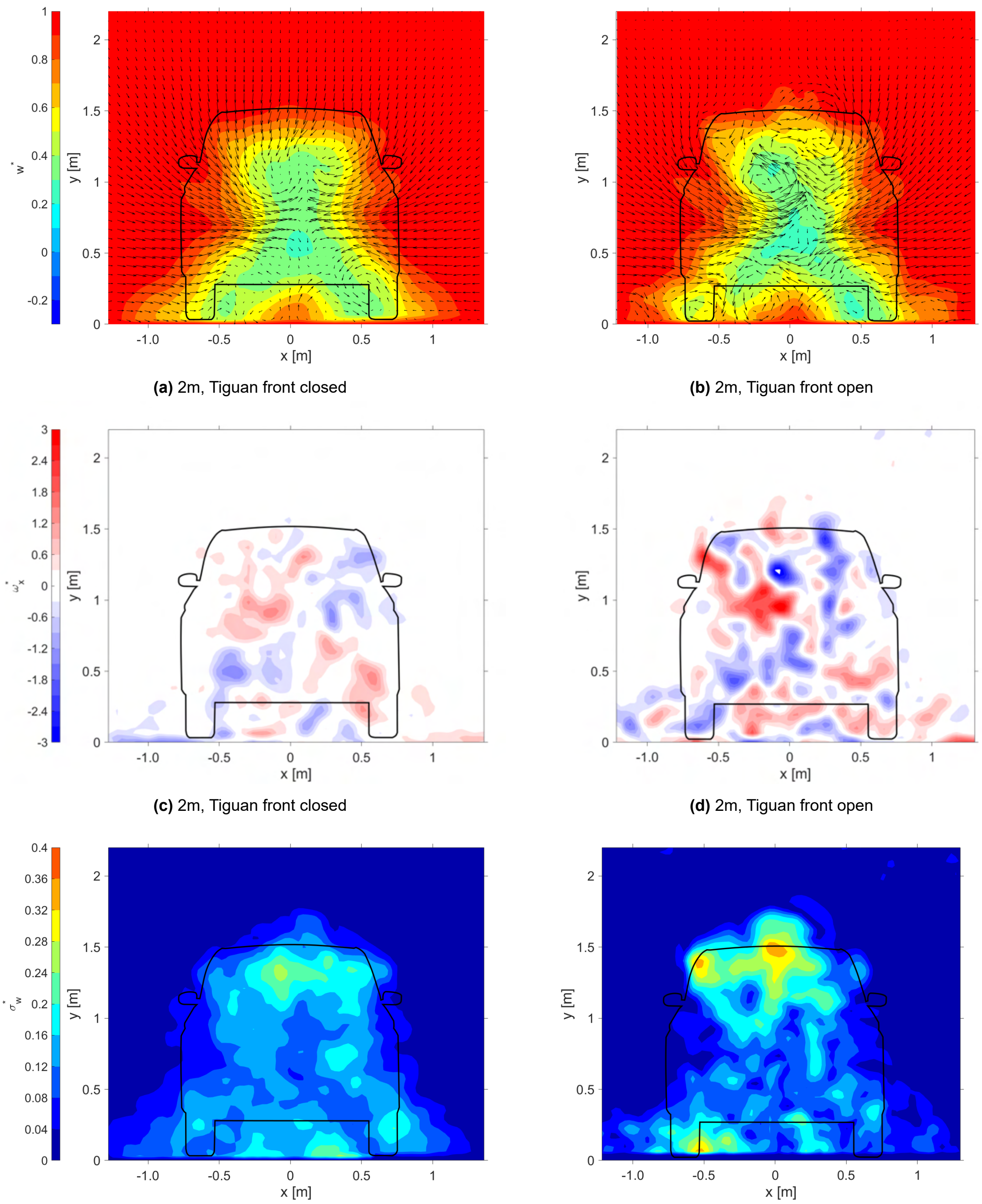

(a) 2m, Tiguan front closed

(b) 2m, Tiguan front open

(c) 2m, Tiguan front closed

(d) 2m, Tiguan front open

(e) 2m, Tiguan front closed

(f) 2m, Tiguan front open

Figure 6.13: Comparison of the velocity, vorticity and turbulence field between the two Tiguan configurations

6.1.6 Flow field comparison to literature

From the analysis of the streamwise vorticity evolution, it is evident that the cars create a different wake structure. This is very interesting, since both cars, to the best of the authors knowledge, are part of the estate-type, or square back type cars. According to researches conducted by Ahmed, 1981, Ahmed et al., 1984 and Huang and Sheu, 2015, this type of car has an upward movement of the flow in the wake, resulting in two counter-rotating vortex pairs. The Tiguan does show similar wake behaviour, as shown in Figure 6.6 and Figure 6.7 on the right. Ahmed, 1981 visualised the XZ plane for both the estate and notchback in his research, which is the ZY plane for this project. This shows a clear upwash in the wake for the estate model, whereas the notchback model shows a clear downwash. The image is repeated in Figure 6.14a for ease of comparison, where it can be seen that the Up follows a notchback wake behaviour, whereas the Tiguan follows an estate wake behaviour. The images for the Up and Tiguan at 2 meter are equal to a location of z/L = 0.56 and z/L = 0.44, or x/L = 0.56 and x/L = 0.44 in the coordinate system of Figure 6.14a.

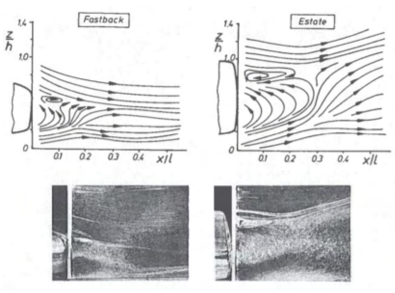

(a) Streamline of the near wake for the Ahmed body Ahmed, 1981

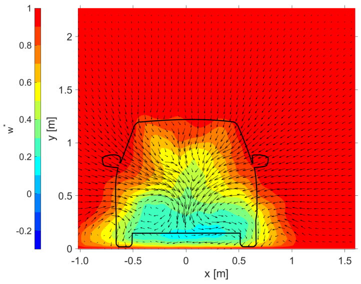

(b) 2m in the wake, Up

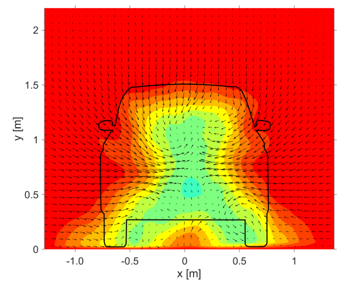

(c) 2m in the wake, Tiguan

A CFD simulation was performed by Huang and Sheu, 2015 for the Mitsubishi Freeca, which is an estate type car with dimensions 4.3 meter in length, 1.7 meter in width and 1.8 meter in height. For the purpose of this thesis, this car is a sufficiently comparable car to the Tiguan. In Figure 6.15a, the core of the main vortices are shown, which are comparable to the vortices found in the wake of the Tiguan. In the near wake at 0.25 meter, it can be seen that the same distinction between the A, B and C vortices was found with the Ring of Fire measurements, with additional D vortices, shown in 6.15b. At 1.50 meter, the B and C vortices have merged, resulting in two counter-rotating vortex pairs in the wake, shown in 6.15c. These show that for both estate type cars, the A vortices cause an upwash and keep their center at a constant height, whereas the C and B vortices merge and create a counter-rotating vortex pair which induce a downwash in at lower height.

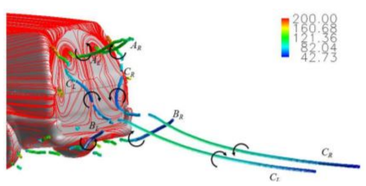

(a) Vortex cores represented by lines for the estate car Mitsubishi Freeca Huang and Sheu, 2015

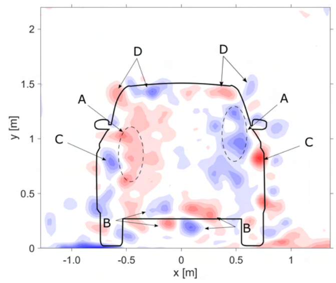

(b) Vorticity of Tiguan at 1.50 meter

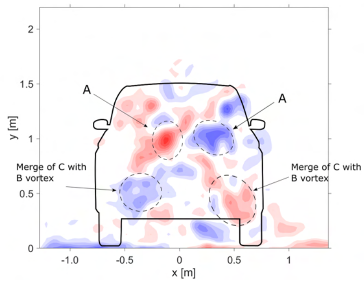

(c) Vorticity of Tiguan at 1.50 meter

Figure 6.15: Result comparison between Mitsubishi Freeca Huang and Sheu, 2015 and Volkswagen Tiguan

Avadiar et al., 2018 and S. Wang et al., 2019 conducted researches towards the estate DrivAer model. The vorticity results of Avadiar et al., 2018 at x/H = 0.5 and 1 are shown in Figure 6.16a and Figure 6.16c. Compared to the Ring of Fire coordinate system, these should be compared to the 0.75 meter (z/H = 0.46) and 1.5 meter flow fields (z/H = 0.92), shown again in Figure 6.16b. From these Figures, one can conclude that the Ring of Fire is able to capture the large vortex pair structure which dominate the vorticity plot at 0.75 meter. However, the D vortex is very weak at 0.75 meter and the B vortex is also not shown. At 1.50 meter, the A vortex and the merging of the C with the B vortex is well visualised through the Ring of Fire compared to the results from Avadiar et al., 2018.

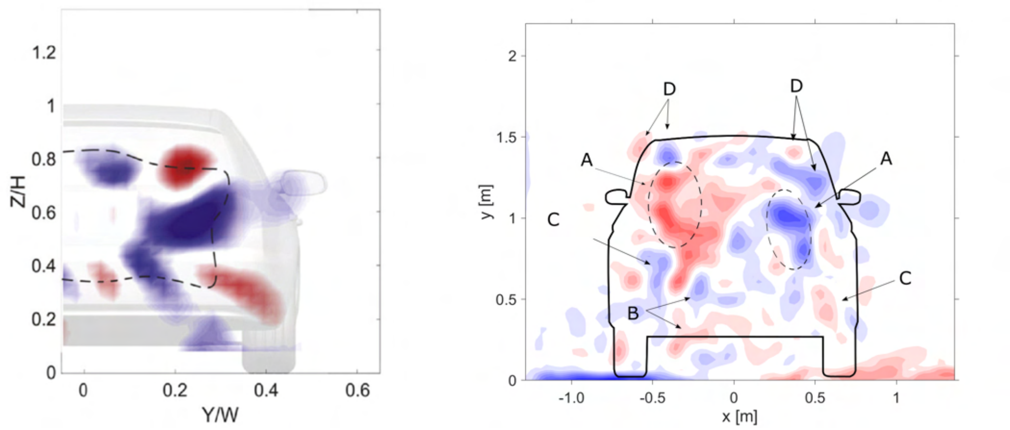

(a) Avadiar et al., 2018 vorticity at x/H = 0.5 **(b)** Vorticity Tiguan 0.75m, or z/H = 0.5

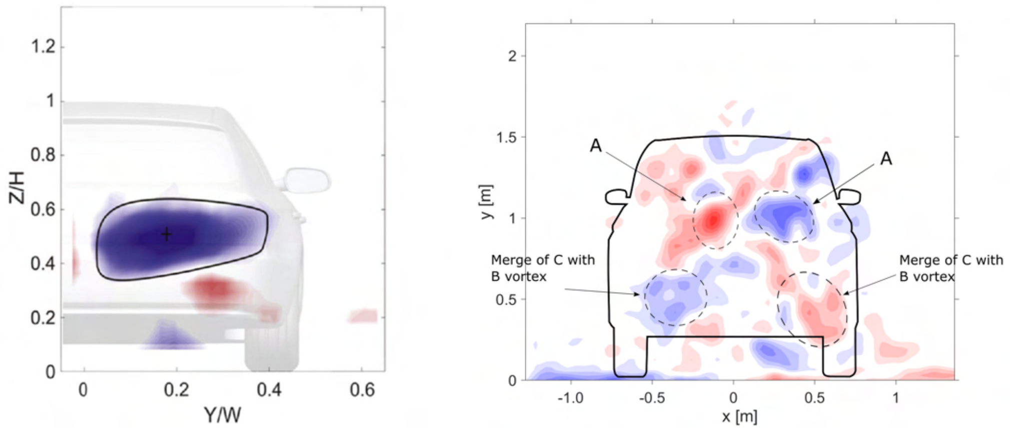

(c) Avadiar et al., 2018 vorticity at x/H = 1 **(d)** Vorticity Tiguan 1.50, or z/H = 1

Figure 6.16: Comparison between results from Avadiar et al., 2018 and the Ring of Fire

S. Wang et al., 2019 used a moving ground plane to investigate the flow topology in the wind tunnel. The results at x/H = 0.5 and x/H = 1 are shown in Figure 6.17 and compared to the Ring of Fire results at the same locations. The focus of this research was on the large A vortex pair, which is therefore also highlighted in Figure 6.17b and Figure 6.17d, showing the vorticity field with vectors of the Ring of Fire measurements. The Ring of Fire vorticity is made non-dimensional according to Equation 6.2, whereas S. Wang et al., 2019 created non-dimensional vorticity with respect to the maximum vorticity value at the x/H = 0.5 plane. The center of the large A vortices at about 0.6 y/H found in the research from S. Wang et al., 2019 corresponds to a center at about y = 1.1 or 0.65 y/H for the Tiguan, indicated with the light green plus sign. The lateral position of the two vortex cores from S. Wang et al., 2019 is about -0.2 y/H and 0.2 y/H for the left and right vortex, respectively. The Ring of Fire results show a core location of the left vortex at -0.3 meter and 0.3 meter, or x/H = -0.18 and x/H = 0.18, respectively. Moreover, the topology and size of the vortices are comparable as well, both with a width and height of about 0.3 y/H.

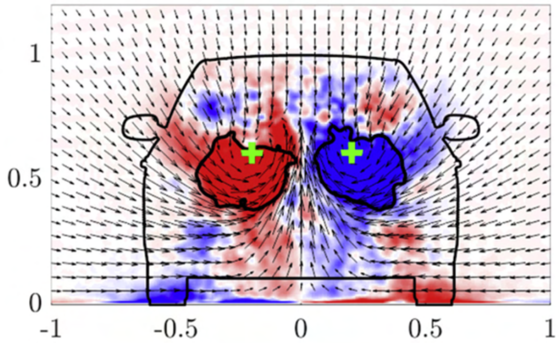

(a) S. Wang et al., 2019 vorticity at x/H = 0.5

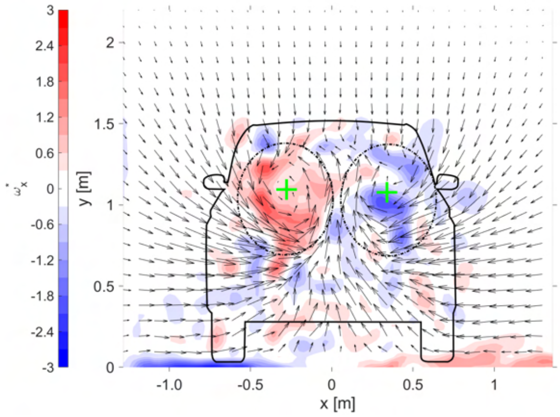

(b) Vorticity Tiguan at 0.75 meter, or z/H = 0.5

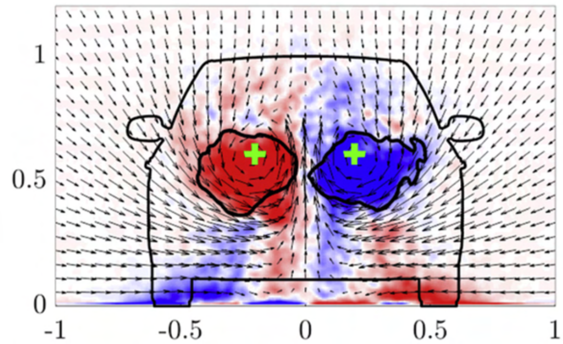

(c) S. Wang et al., 2019 vorticity at x/H = 1

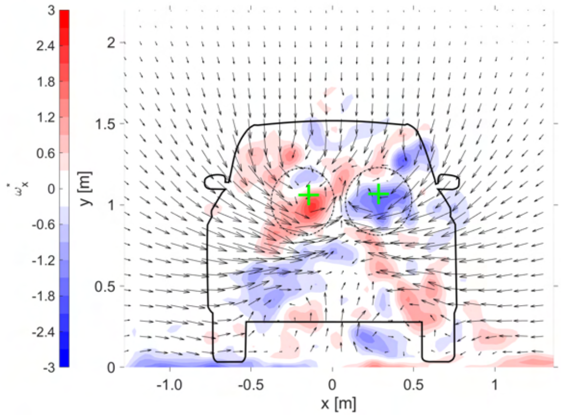

(d) Vorticity Tiguan at 1.50 meter, or z/H = 1

Figure 6.17: Comparison between results from S. Wang et al., 2019 and the Ring of Fire

On the contrary, the Up shows a more similar wake structure to the fastback or notchback, where the wake is characterised by a downwash and hence resulting in two large counter-rotating vortex pairs. This has been shown in research to be the flow structure in the wake of a 25° slant angle Ahmed body, as investigated by S.Becker et al., 2002 where the result is shown in Figure 6.18a. In his research, Laser Doppler Anemometry was employed to generate velocity fields at several distances behind the model, of which one was located at 500 mm behind the model. With a model length of 1000 mm, this was at a location of 0.5 z/L. To compare this field with the Up, the in-plane velocity vector field closest to 0.5 z/L was used, which is at 2 meter, or 0.56 z/L. This vector field is shown in Figure 6.18b. Comparing the results, both the Ahmed body and the Up show comparable in-plane vectors, clearly showing one pair of large vortices with their centers located around z = 150 mm for the Ahmed body and y = 0.4 meter for the Up. This corresponds to a location of 0.15 z/L for the Ahmed and 0.11 y/L for the Up. The lateral location of the cores of this vortex pair are located at y = -120 mm and y = 120 mm, or -0.12 y/L and 0.12 y/L for the Ahmed and x = -0.35 m and x = 0.35 m, or -0.10 x/L and 0.10 x/L for the Up.

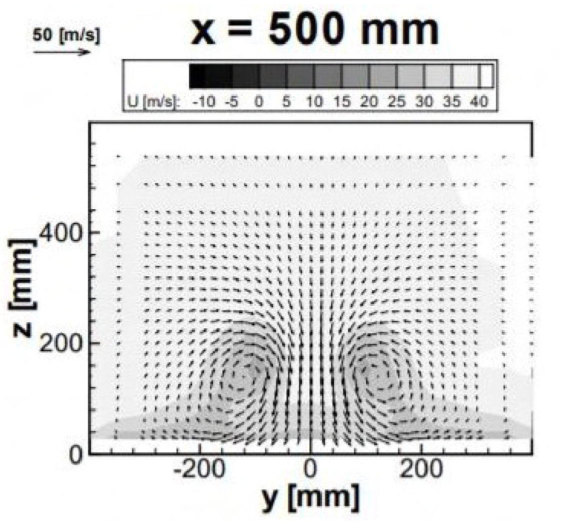

(a) Vector field for the Ahmed body at 500mm, equal to z/L = 0.5

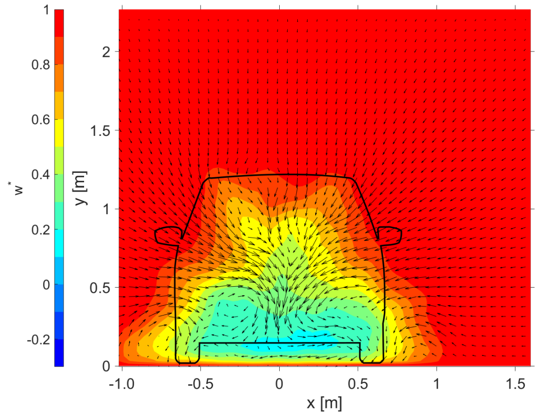

(b) Vector field for the Up at 2 meter, or z/L = 0.56

Figure 6.18: In-plane velocity vector comparison between Ahmed body and Up

Strachan et al., 2004 conducted a numerical simulation together with Laser Doppler Anemometry to test the capabilities of CFD in the visualisation of the vortex structures in the wake of an Ahmed body with 25° slant angle. The results are shown in Figure 6.19a. This vector field was taken at a distance z/L = 1. To compare this to the results of this project, the velocity field at 3.5 meter is taken, which is equal to z/L = 0.97. This field is shown in Figure 6.19b.

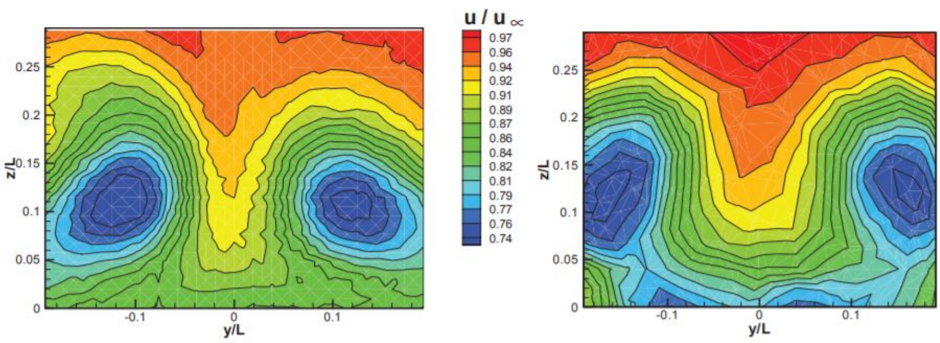

(a) LDA (left) and CFD (right) results from Strachan et al., 2004

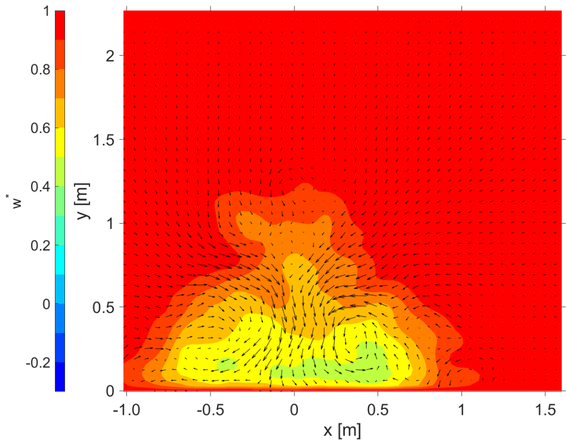

(b) Vector field for the Up at 3.50 meter, z/L = 0.97

Figure 6.19: Result comparison of Strachan et al., 2004 with Ring of Fire

For the CFD, the vortex cores are located at z/L = 0.12 and y/L = 0.15. For the LDA, these are located at z/L = 0.1 and y/L = 0.12, or y/L = 0.1 and x/L = 0.12 in the Ring of Fire reference system. The vortex cores from the Ring of Fire results are located at y/L = 0.09, x/L = 0.10 and x/L = -0.12. The height is therefore very similar (0.1 compared to 0.09), as well as the x/L (0.10 for the right and -0.12 for the left, versus $\pm$ 0.12). From this comparison to the literature, it can be concluded that the Up behaves like a fastback, similar to an Ahmed body with a slant angle of 25°.

Lastly, a vortex pair is considered which has not been discussed yet. Strachan et al., 2007, Krajnovic and Davidson, 2005b and X. W. Wang et al., 2013 report newly found lower vortices, which have not been found in other literature which they ascribe to a non-moving ground and no ground clearance used underneath the model. Strachan et al., 2004 and Krajnovic and Davidson, 2005b reported that these vortices dissipate at approximately 0.35 z/H or 0.144 z/L, both resulting in about 0.50 meter for the Up and 0.64 for the Tiguan. X. W. Wang et al., 2013 showed their results for x/Z = 0.23, or 0.35 meter behind the Up and 0.38 behind the Tiguan. In Figure 6.20a, Figure 6.20b and Figure 6.20c, the result of X. W. Wang et al., 2013, Up and Tiguan are shown, respectively.

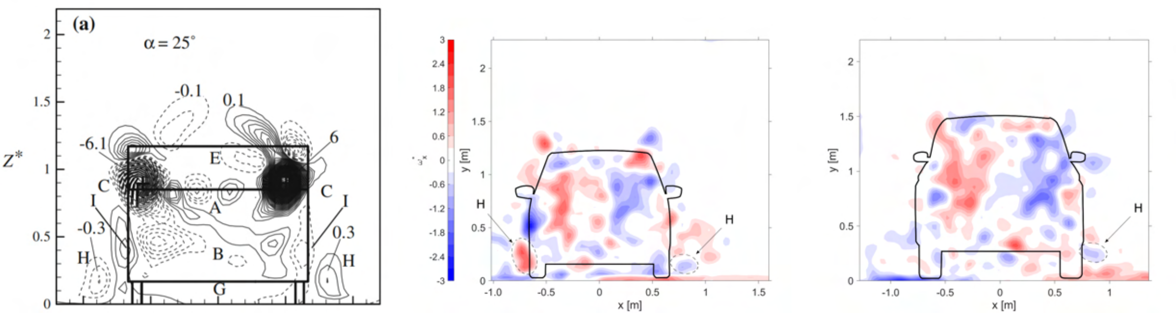

(a) H-vortex found by X. W. Wang et al., 2013 **(b)** H vortex analysis Up **(c)** H vortex analysis Tiguan

Figure 6.20: H-vortex comparison of X. W. Wang et al., 2013 with Ring of Fire

For the Up it appears that on the lower left a similar vortex is found to the H-vortices, which also appears to be quite strong. On the right of the car, a very weak vortex structure can be identified at the location where the H-vortex is supposed to be. This one is however much weaker than the left vortex. It could be the case that due to the relatively high turbulence outdoor and the wind, the lateral position of the instantaneous vortices shifts too much and therefore the average does not show the vortex.

6.2 Drag results

In this section, the conservation of momentum approach, discussed in Chapter 3, is implemented in this project to calculate the area drag coefficient. Moreover, an attempt is made to analyse the uncertainty for the application of the Ring of Fire for the automotive industry through the use of a 95% confidence interval. To distinguish between the two car models and two configurations for the Tiguan, the statistical significance is estimated through a one-way analysis of variance (ANOVA) Bewick et al., 2004. This function determines whether the data from different configurations or models have a common mean. Lastly, an analysis is performed in an effort to correlate the difference or similarity in drag coefficient with the flow field.

6.2.1 Drag area comparison

To calculate the drag area, a velocity field before and after the passage of the car is required. For the upstream velocity field, 100 images were used to create an averaged upstream velocity field, following the suggestions of previous Ring of Fire experiments Spoelstra, 2017, de Martino Norante, 2018, Spoelstra, 2017, Mahalingesh, 2020. Using an averaged upstream plane rather than an instantaneous one reduces the standard deviation of the drag measurements, as reported by de Martino Norante, 2018. For the downstream planes, the velocity fields shown in this Chapter have been used, at 1, 1.5, 2, 2.5, 3, 3.5, 4 and 5 meter. The reasoning behind this choice will be discussed below. For the downstream planes, the drag has been computed using the instantaneous velocity fields. If these are averaged, then the Reynolds stresses would not be accounted for, which leads to unrealistic drag values.

The CdA plots for the Tiguan front closed, Tiguan front open and Up are shown in Figure 6.21. Since the area drag coefficient can be calculated for every wake velocity field, the variation of the drag can be plotted versus the distance in the wake. The grey lines represent the individual runs, which amount to a total of 36 runs for the Tiguan front closed, 9 runs for the Tiguan front open and 22 runs for the Up. The red line represents the average at each distance, where the uncertainty bars show the 95% confidence interval of the mean value. This means that there is a 95% probability that the mean value of the data lies within the uncertainty bars shown for each mean value. The 95% confidence interval was calculated using Equation 6.5:

$$U = k\frac{\sigma}{\sqrt{N}} \tag{6.5}$$

Where U is the uncertainty, $k = 2$ for a 95% interval, σ is the standard deviation from the mean and N is the total number of samples.

The following general remarks should be made about the drag calculations. First of all, the CdA is highly underestimated up to 1.5 meter in the wake for all three configurations. According to Terra et al., 2017, the pressure term in the expression of the drag for a control volume cannot be neglected up to 5 characteristic lengths behind a sphere. For a sphere, the characteristic length is the width and in previous Ring of Fire experiments, the torso width of a cyclists was used. Hence, using the width of the car to be in line with previous research, the pressure would still be relevant up to approximately 8 meter and 9 meter in the wake of the Up and Tiguan, respectively. To the best of the author's knowledge, no publicly available research indicates up to which distance in the wake of the car pressure effects should still be accounted for or at which distance these effects can be neglected. Thus, pressure effects have been included in the drag calculations. However, as becomes apparent from the plots, the pressure in the near wake of a passenger car driving at a velocity of 120 km/h cannot be accurately represented by the 2D Pressure Poisson equation, which was used to estimate the pressure, as explained in Section 3.2.3. The out-of-plane component of the three dimensional, highly turbulent near wake of the car cannot be computed with the stereoscopic PIV set-up, therefore resulting in an inaccurate representation of the pressure.

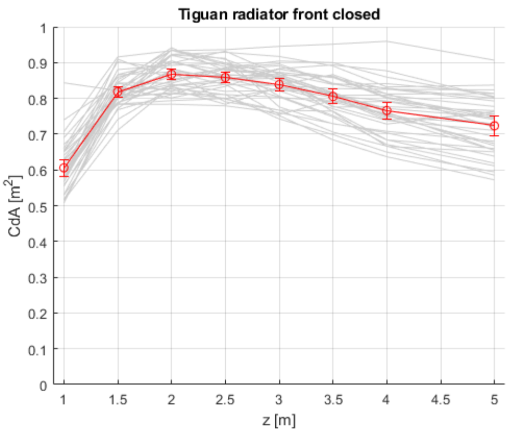

(a) CdA of Tiguan with the front closed

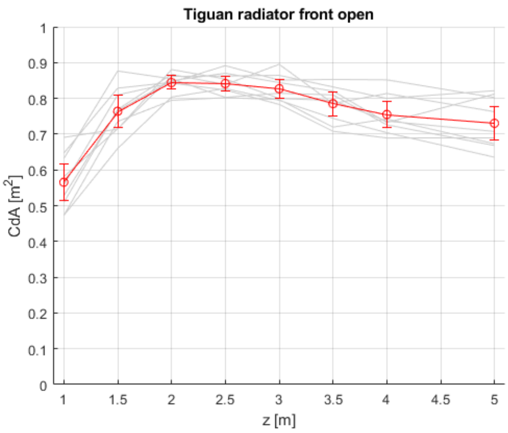

(b) CdA of Tiguan with the front open

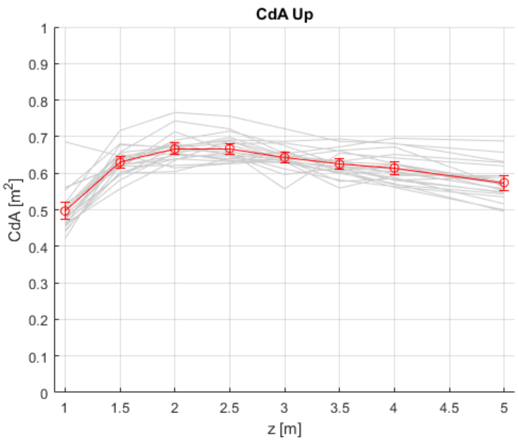

(c) CdA of Up

Figure 6.21: The CdA values for the Tiguan front closed, Tiguan front open and the Up

Between 1.5 and 3 meter for the Tiguan front closed and Up, and between 2 and 3 meter for the Tiguan front open, the mean value of the CdA shows a somewhat constant value. Further down in the wake, after 3 meter, all three configurations show a decrease in mean value and it can be seen that the individual runs start to increase their respective deviation from the mean value. A possible reason for this could be that the wake starts to leave the field of view for distances larger than 3 meter, which is the case for the Up. Nonetheless, this does not explain the decrease in CdA for the Tiguan configurations, since their wake structures remain captured inside the field of view up to several meters further downstream. Therefore, the following argumentation is given why the CdA shows a near constant decrease. The large scale structures identified in the near wake of the cars, diffuse into smaller scales at increasing distances in the wake. Since the interrogation window size is the same for every vector field, the PIV algorithm is not capable of identifying these small scale structures, leading to an underestimation of the drag. At increasing distance behind the car, the size of these structures keeps decreasing, therefore increasing the underestimation of the drag. It is interesting however, that previous Ring of Fire projects for cyclists were capable of determining the drag with a more or less constant value even up to 10 meter in the wake Hirsch, 2018 de Martino Norante, 2018. It could be the case that due to a higher turbulence in the wake of the car (up to 37%) compared to previous experiments (25% for de Martino Norante, 2018) and the highly three dimensional flow at 120 km/h the interrogation window size should decrease to account for the larger difference between the largest and smallest structures.

Following this reasoning, an analysis for the drag values is performed on the values at 2, 2.5 and 3 meter in the wake. At lower values, the momentum term is apparently highly underestimating the drag, hinting at the fact that the pressure could be the dominant term within 1.5 meter behind the cars. However, as the out-of-plane velocity gradient is very large (the value rapidly decays in the first few meters, from 130% of the car velocity at 0.5 meter to less than 40% of the car velocity, hence from 41 m/s to 13 m/s), the pressure estimation approach in this work does not suffice. After 3 meter, the wake diffuses too much and the uncertainty of the mean increases.

The final CdA value is 0.8375 for the Tiguan open, 0.8548 for the Tiguan closed and 0.6591 for the Up, with a 95% confidence interval of 0.0155, 0.0216 and 0.0150, respectively. These values have been determined by averaging their respective values at 2, 2.5 and 3 meter. Comparing this to previous Ring o Fire experiments, the latest research by Mahalingesh, 2020 reported an uncertainty of 2.4%, whereas de Martino Norante, 2018 reported an uncertainty of ± 2.7-5.3%, Spoelstra, 2017 reported an uncertainty of ±5% and Hirsch, 2018 reduced this uncertainty in his project to ± 2.1-2.3%. In this project, the uncertainty was between ±1.8-2.6%, where the lower limit was achieved for the Tiguan front closed configuration and the upper limit for the Tiguan front open configuration. Most likely this discrepancy can be ascribed to the much higher number of runs for the front closed configuration, 38 versus 9. The Up, with 22 runs, had an uncertainty of ±2.3%, which is in line with this reasoning.

	Up	Tiguan radiator front closed	Tiguan radiator front open
CdA	0.6591	0.8548	0.8375
95% CI	±2.3%	±1.8%	±2.6%

For a more thorough analysis of the drag calculation and to gain more insight in the sources of drag, a comparison is made between the contribution of the momentum and the pressure. The contribution of the momentum term in percentage of the total drag is shown in Figure 6.22a, whereas the contribution of the pressure term in percentage of the total drag is shown in Figure 6.22b.

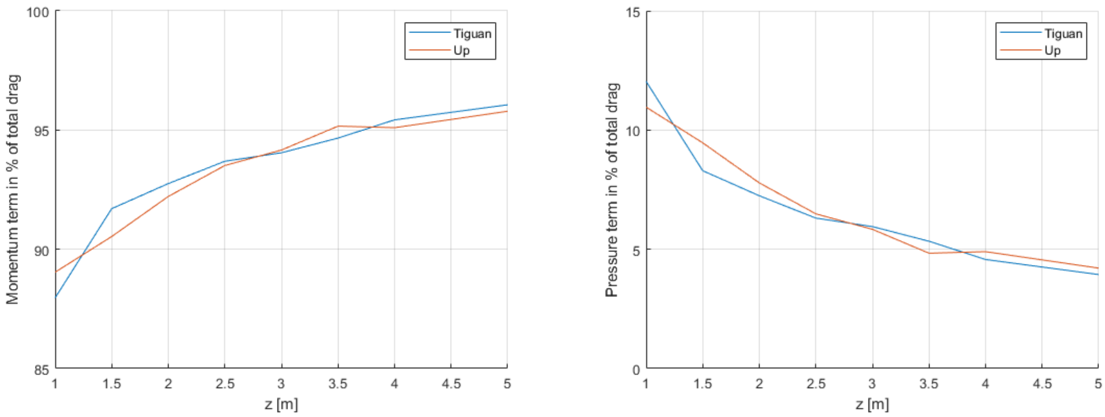

(a) CdA of Tiguan with the front closed

(b) CdA of Tiguan with the front closed

Figure 6.22: The contribution of the momentum and pressure term to the drag, in %

The momentum term has a contribution of 88% and 89% at 1 meter and 96% at 5 meter of the total drag in the wake for the Tiguan and Up, respectively. Consequently, the pressure term has a contribution of 12% and 11% at 1 meter and 4% at 5 meter for the Tiguan and Up, respectively. Hence, it can be concluded that the pressure term within 5 meters behind the car cannot be neglected, as 4% is still significant. Moreover, it should be noted that it is very likely that the pressure is underestimated, due to the neglected out-of-plane velocity tensor. Since stereoscopic PIV is not capable of determining this tensor, for a more accurate representation of the pressure a tomographic setup could be more applicable. Additionally, it should be noted that the momentum and drag contribution is more or less equal for the Tiguan and for the Up, which strengthens the argumentation that there is most likely a systematic error in the approach in the calculation of the drag.

6.2.2 Statistical significance

To assess whether the drag values at 2, 2.5 and 3 meter are of statistical significance, a one-way analysis of variance is conducted Bewick et al., 2004. This is done to analyse whether the difference in mean values and the deviation of individual runs with respect to the mean for the different configurations (Tiguan open, Tiguan closed and Up) are significant or not. In a one-way analysis of variance, a significance value is calculated, called the F-statistic, which is the ratio of mean-squares. Additionally, the test-statistic value is computed and the probability that the F-statistic is larger than this test-statistic determines whether the difference in mean value is statistically significant. This probability, called p-value, is compared to a commonly used threshold value in statistics of 0.05. If $p>0.05$, the difference is the mean is not statistically significant. If $p<0.05$, the difference in the mean is statistically significant and it can be concluded that the two means are indeed different.

The boxplots from the analysis are shown in Figure 6.23. Figure 6.23a, Figure 6.23b and Figure 6.23c show the boxplots for the comparison in Tiguan configuration, where in each plot the Tiguan closed is shown on the left and the Tiguan open on the right. Figure 6.23d, Figure 6.23e and Figure 6.23f show the boxplots for the comparison between Tiguan closed and the Up, with the Tiguan closed on the left and the Up on the right. The red line shows the median value, the upper limit of the blue boxplot is the 25th percentile and the lower limit is the 75th percentile. The whiskers show the most deviated values, excluding the outliers. These are represented by the red crosses.

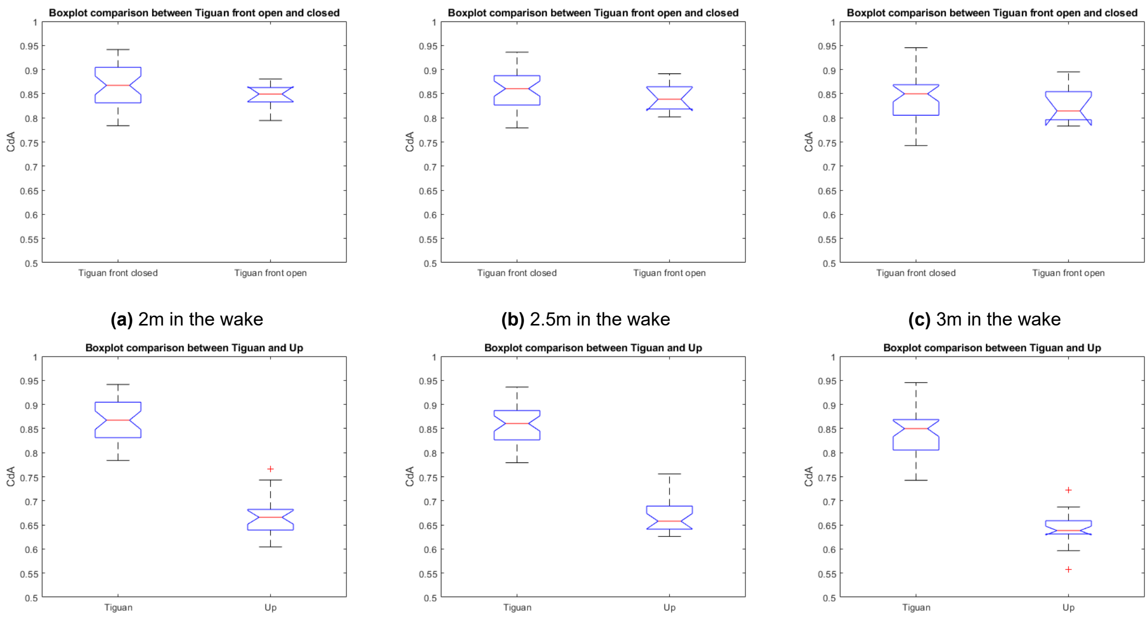

(a) 2m in the wake **(b)** 2.5m in the wake **(c)** 3m in the wake

(d) 2m in the wake **(e)** 2.5m in the wake **(f)** 3m in the wake

Figure 6.23: Results of the one-way analysis of variance

From these plots, it can be seen that between the two Tiguan configurations, the median values are approximately 0.02 apart from each other, with the Tiguan open showing the lower median value. Moreover, the whiskers show that the range of used values is much larger for the Tiguan closed than for the Tiguan open, most likely due to the many more runs conducted with the Tiguan closed. Moreover, the complete boxplot of the Tiguan open is for all three distances entirely within the range of the Tiguan closed. The comparison between the Tiguan closed and Up shows that the medians differ about 0.2 in CdA, where there are also no overlapping results.

The p-values for the Tiguan comparison are 0.162, 0.2713 and 0.5151, at 2, 2.5 and 3 meter, respectively. Since these values are all much higher than the significance level of 0.05, it can be concluded that the mean values of the two Tiguan configurations are not statistically different. This means that during this Ring of Fire measurement campaign, the difference in drag between the Tiguan

front closed and Tiguan front open could not be measured.
The p-values for the comparison between the Tiguan and Up are $8 \cdot 10^{-24}$, $4 \cdot 10^{-24}$, $6 \cdot 10^{-23}$. These values are all much lower than the significance level of 0.05, and therefore the difference in the mean values is very significant and the Ring of Fire is capable of measuring the difference between these two cars.

6.2.3 Comparison to Volkswagen wind tunnel results

The drag area coefficient of the Volkswagen Tiguan and Up has been measured inside the wind tunnel. This resulted in a CdA of 0.85 for the Tiguan front open and a CdA of 0.84 for the Tiguan front closed. For the Up, a value of 0.66 was measured. As shown in Figure 6.21, these results are quite accurately represented by the Ring of Fire measurements, at a distance of 2-3 meter in the wake. The uncertainty of this ensemble averaged CdA value has been discussed in Subsection 6.2.1, whereas the statistical significance of these values has been discussed in Subsection 6.2.2. The CdA has been measured in line with the wind tunnel measured CdA. However, the CdA values for the Tiguan open and Tiguan closed are reversed compared to the wind tunnel measurements. In the aforementioned statistical significance discussion, it was shown that from the instantaneous drag measurements there is no statistical significant difference between the mean value of the drag for the closed configuration compared to the open configuration. Therefore, there is no clear distinction between one configuration and the other and the difference obtained is not statistically founded. Still, an attempt is made to explain the curious reverse of drag values. Only 11 runs could be used for the drag analysis of the open configuration, whereas 36 runs could be used for the drag analysis of the open configuration. Therefore, erroneous results have a larger result on the open configuration value than for the closed configuration, which can also be seen from the box plots where the variation of the open configuration is completely captured by the variation of the closed configuration.

	Ring of Fire	Volkswagen wind tunnel	Relative difference
CdA Up	0.6591	0.6605	-0.2%
CdA Tiguan radiator front closed	0.8548	0.8361	+2.23%
CdA Tiguan radiator front open	0.8375	0.8501	-0.015%

6.3 Relate flow fields to drag coefficient

The Ring of Fire measurement system is capable of providing an accurate representation of the flow field as well as calculating the drag by implementing the control volume approach. Using this fact, an attempt can be made to correlate the drag force to the flow field. In this section, an attempt is made to correlate the drag values for the Up and Tiguan, following from a wind tunnel measurement and the Ring of Fire, to the flow topology.
For the purpose of this discussion, the Tiguan front closed configuration is compared to the Up. The Tiguan in this experiment had a frontal area of 2.52 m^2, where the Up had a frontal area of 2.02 m^2. For the Ring of Fire drag coefficients, a value of 0.339 for the Tiguan and 0.326 for the Up was found. The wind tunnel measurements conducted at Volkswagen resulted in a drag coefficient of 0.332 for the Tiguan and 0.327 for the Up. This means that there is a difference of only 0.005 between the two car models.

As discussed in Chapter 4, the size of the Tiguan is larger than the Up in all direction, and additionally the length is relatively larger as well. From the results shown in this Chapter, the wake of the Tiguan consists of 4 main vortices. One pair of counter rotating vortices which induce an upwash in the wake and prevent it from shrinking in vertical direction. One weaker pair of counter-rotating vortices, in opposite direction of the upper pair of counter-rotating vortices, induce a weak downwash in the lower part of the flow and induce a slight lateral expansion of the wake. On the contrary, the Up has 2 strong counter rotating vortices, which induce a strong downwash and thereby reduce the height of the wake, which results in a lateral expansion of the wake due to the outward velocity vector near the ground.

Although difference in wake structure, there is no clear difference in vortex strength and out-of-plane velocity for both cars. Moreover, their decay in streamwise direction is also quite similar, both weakening and recovering to freestream conditions comparatively. A more thorough investigation should be conducted as to why the drag coefficients are so similar between those two different car models, but due to a lack of literature available and to the best of the author's knowledge, no further explanation can be provided in addition to the aforementioned analysis.

Chapter 7

Conclusion and recommendations

In this section, the conclusions of this thesis work are laid out and recommendations for future research are provided.

7.1 Conclusion

The objective of this thesis was to implement the Ring of Fire system for full-scale cars and assess its feasibility in visualizing the flow topology between different cars and configurations in the wake. Moreover, the drag for these cars and configurations is calculated through the control volume approach. To assess the flow topology, a comparison between the Tiguan with the front radiator closed and the Up is made, as well as a comparison between the Tiguan with the front radiator closed and open. The absolute drag values and their uncertainty are compared between the different models and configurations, and additionally are compared to wind tunnel test results.

The Ring of Fire experiment was conducted on-site and outdoor at the Volkswagen proving ground in Wolfsburg, Germany. The Volkswagen Tiguan and Up were tested at a velocity of 120 km/h. The testing of the Tiguan consisted of measurements with the front radiator open and closed. Due to wind, the first days of testing lead to extensive loss of seeding. This was resolved by placing tarps at the entrance and exit of the tunnel. Two lasers were used as well as 4 seeding rakes, to ensure sufficient light intensity and seeding density in the field of view of 3x3 meter. Nonetheless, it remained a challenge to generate and contain sufficient seeding inside the measurement domain, therefore severely limiting the number of runs that could be used for processing and data analysis. In the end, 36 good quality runs were acquired for the Tiguan with the radiator front closed, 22 for the Up and 9 for the Tiguan with the radiator front open.

The analysis of the stream wise evolution of the wake topology behind the Up and Tiguan shows that the out-of-plane velocity is comparable for both cars at specified distances in the wake. Moreover, the maximum speed in the wake is approximately 130% of the car velocity for both models. On the contrary, some clear discrepancies are found. Where the first meter shows a clear upwash for both car models, after this distance the Up shows a clear downwash whereas the upwash in the wake of the Tiguan remains. This leads to a different wake topology further downstream, where for the Up the A-pillar vortices weaken and the C-pillar vortices form two counter-rotating vortices, creating this downwash. Moreover, due to the downwash the wake shrinks in vertical direction and expands in horizontal direction. In contrast to the topology in the wake of the Up, the A-pillar vortices in the wake of the Tiguan do not weaken and the C-pillar vortices likely merge with the B-vortices, coming from underneath the car. This results in four large scale vortices in the wake of the Tiguan, where the upper pair induces a strong upwash and therefore prevents the wake from losing height. Moreover, the lower vortex pair counter-rotates with respect to the upper pair, leading to a 'mushroom' kind of shape in the far wake, where the lower part laterally extends in a triangular shape.

Next to the in-plane velocity, out-of-plane velocity and vorticity, the an attempt is made to assess the turbulence and pressure in the wake. The turbulence for the Tiguan and Up are comparable, extending up to 36% and 37% of the car velocity for the Tiguan and Up, respectively. The pressure was reconstructed using the 2D Pressure Poisson equation, since the out-of-plane velocity gradient cannot be captured with stereoscopic PIV. Plotting this pressure shows that the low pressure regions correspond well with the vortex cores.

The drag values obtained from the control volume approach identified at 2, 2.5 and 3 meter in the wake. Up to two meter, a steep increase in drag is observed, which is most likely due to an underestimation of the pressure. For the pressure reconstruction, the out-of-plane gradient is neglected, but due to the high out-of-plane motion in the wake of the car it may be concluded that this assumption is not valid for cars. Moreover, after 3 meter, the wake has likely diffused too much, meaning that the interrogation window size becomes too large to identify the smaller scale flow structures and therefore underestimating the drag. Moreover, for some data, especially for the Up, the wake starts moving outside the measurement domain after 5-6 meter. Therefore, the choice was made to limit the results and discussion of this project up to this distance.

The final drag values were ensemble averaged, leading to a final drag area of 0.8548 m^2 for the Tiguan closed, 0.8375 m^2 for the Tiguan open and 0.6591 m^2 for the Up. The uncertainty of the mean was quantified at a 95% confidence interval and resulted in $\pm$1.8%, $\pm$2.3% and $\pm$2.6% for the Tiguan closed, Tiguan open and Up configuration, respectively. This is in line with the uncertainties found in a previously conducted outdoor Ring of Fire research by Mahalingesh, 2020. A slight improvement is most likely the consequence of a larger number of runs, which is also in line with the findings in this project. Using a one-way analysis of variance, it can be concluded that during this project, no statistical significant difference between the drag of the Tiguan front closed and open configuration is established. Nonetheless, the difference between the Up and Tiguan was significant, meaning that the Ring of Fire is able to measure the difference between different car models.

7.2 Recommendations

Based on this Ring of Fire project, recommendations for future research towards the further implementation of the Ring of Fire for cars can be made. One of the biggest drawbacks of the current campaign was the difficulty to keep sufficient seeding inside the measurement domain. Using a tarp as a curtain at the exit of the tunnel already showed big improvements, but for even better seeding it is recommended to also use a tarp at the entrance. However, this would increase the minimum number of people required to do measurements from three to five, since two are needed for each curtain. Moreover, one could think of creating a longer tunnel, to further reduce the influence of cross wind in the tunnel.

Another drawback was that the seeding rakes did not function optimally due to the temperature outside. This was lower than the designed operating temperature, reducing the efficiency of the seeding rakes. This was largely resolved by directing the seeding tubes through a small heated container, but for future research conducted outdoors this should be kept in mind during the design process of the setup.

In this project, it became clear that the 2D Poisson equation for the pressure calculations does not provide an accurate representation of the pressure within 2 meters behind the car. Therefore, it is suggested to consider a tomographic setup where pressure measurements can be conducted in three dimensions, thereby including the out-of-plane velocity gradient. However, this would increase the difficulty and complexity of the measurements, so this should only be considered when accurate drag calculations are desired within 2 meters behind the car.

For the drag after 3 meters in the wake, the main conclusion drawn in the report was that the wake diffuses too smaller scales than the interrogation window used in this project is able to resolve. Since the interrogation window size is based on the in-plane velocity, a smaller in-plane velocity can reduce the size of the interrogation window. Therefore, future research for the implementation of the Ring of Fire for automotive aerodynamics could look into adaptive interrogation windows, where the interrogation window decreases with increasing distance in the wake.

The last recommendation is that the Ring of Fire has the potential to be very useful with respect to measurements conducted for drafting cars or for car aerodynamics during cornering. This is with the currently available techniques not possible, whereas there is potential for the Ring of Fire to fill this gap.

References

A. I. Heft, N. A. A., T. Indinger. (2011). Investigation of unsteady flow structures in the wake of a realistic generic car model. *29th AIAA Applied Aerodynamics Conference*. https://doi.org/doi:10.4271/840300

Adrian, R., & Westerweel, J. (2011). *Particle image velocimetry*. Cambridge University Press.

Ahmed, S. (1981). Wake structure of typical automobile shapes. *Journal of fluids engineering*, *103*(162-169).

Ahmed, S., Ramm, G., & Faltin, G. (1984). Some salient features of the time-averaged ground vehicle wake. *SAE Technical Paper 840300*. https://doi.org/doi:10.4271/840300

Anderson, J. (2017). *Fundamentals of aerodynamics* (6th international ed.). McGraw Hill Education.

Ashton, N., & Revell, A. (2015). Comparison of rans and des methods for the drivaer automotive body. *SAE Technical Paper 2015-01-1538*. https://doi.org/doi:10.4271/2015-01-1538

Avadiar, T., Thompson, M., Sheridan, J., & Burton, D. (2018). Characterisation of the wake of the drivaer estate vehicle. *Journal of Wind Engineering and Industrial Aerodynamics*, *177*, 242–259. https://doi.org/https://doi.org/10.1016/j.jweia.2018.04.013

Bewick, V., Cheek, L., & Ball, J. (2004). Statistics review 9: One-way analysis of variance. *Crit care*, *8*(130). https://doi.org/https://doi-org.tudelft.idm.oclc.org/10.1186/cc2836

Bosbach, J., Kühn, M., & Wagner, C. (2008). Large scale particle image velocimetry with helium filled soap bubbles. *Experimental Fluids*, *46*(539–547). https://doi.org/DOI10.1007/s00348-008-0579-0

Buckley, F. T. (1995). Abcd - an improved coast down test and analysis method. *JOURNAL OF PASSENGER CARS: Part 1*, *104*(6). https://doi.org/https://www.jstor.org/stable/44612276

de Martino Norante, L. (2018). *Dvances and assessment of the ring of fire concept for on-site cycling aerodynamics* (Master's thesis). Delft University of Technology. the Netherlands.

Duncan, B. D., Sengupta, R., Mallick, S., Shock, R., & Sims-Williams, D. (2002). Numerical simulation and spectral analysis of pressure fluctuations in vehicle aerodynamic noise generation. *Journal of passenger car: mechanical systems journal*, *111*(6). https://doi.org/https://www.jstor.org/stable/44719260

Duncan, B. D., & Sims-Williams, D. B. (2002). Numerical simulation and spectral analysis of pressure fluctuations in vehicle aerodynamic noise generation. *Journal of passenger car: mechanical systems journal*, *111*(6). https://doi.org/https://www.jstor.org/stable/44719260

Elsinga, G., Scarano, F., Wieneke, B., & BW, V. O. (2006b). Tomographic particle image velocimetry. *Experimental Fluids*, *41*(933-947).

Good, G. M. L., Howell, J. P., Passmore, M. A., & Cogotti, A. (1998). A comparison of on-road aerodynamic drag measurements with wind tunnel data from pininfarina and mira. *SAE Paper*, *980394*. https://doi.org/http://dx.doi.org/10.4271/980394

Hirsch, M. (2018). *Accuracy assessment of the ring of fire system for on-site aerodynamic drag measurements* (Master's thesis). Delft University of Technology. the Netherlands.

Howell, J., Sherwin, C., Passmore, M., & Good, G. L. (2002). Aerodynamic drag of a compact suv as measured on-road and in the wind tunnel. *SAE Technical paper 2002-01-0529*.

Huang, P. G.-Y., & Sheu, T. W.-H. (2015). Vortical flow structure in the wake of an estate car. *Commun. Comput. Phys.* https://doi.org/doi:10.4208/cicp.271114.250515s

Jeong, J., & Hussain, F. (1995). On the identification of a vortex. *J. Fluid Mech.*, *332*, 339–363.

Jux, C., Sciacchitano, A., Schneiders, J., & Scarano, F. (2018). Robotic volumetric piv of a full-scale cyclist. *Experiments in Fluids*, *59*. https://doi.org/10.1007/s00348-018-2524-1

Kat, R., & Ganapathisubramani, B. (2013). Pressure from particle image velocimetry for convective flows: A taylor's hypothesis approach. *Measurement Science and Technology*, *24*, 024002. https://doi.org/10.1088/0957-0233/24/2/024002

Krajnovic, S., & Davidson, L. (2005a). Flow around a simplified car, part 1: Large eddy simulation. *Journal of Fluids Engineering*, *127*(907-918). https://doi.org/DOI:10.1115/1.1989371

Krajnovic, S., & Davidson, L. (2005b). Flow around a simplified car, part 2: Understanding the flow. *Journal of Fluids Engineering*, *127*(919-928). https://doi.org/DOI:10.1115/1.1989372

Kühn, M., Ehrenfried, K., Bosbach, J., & Wagner, C. (2011). Large-scale tomographic particle image velocimetry using helium-filled soap bubbles. *Experiments in fluids*, *50*(929–948). https://doi.org/DOI10.1007/s00348-010-0947-4

Kurtulus, D., Scarano, F., & David, L. (2007). Unsteady aerodynamic forces estimation on a square cylinder by tr-piv. *Experiments in Fluids*, *42*, 185–196. https://doi.org/10.1007/s00348-006-0228-4

Liu, J., Zhang, Z., Wang, Y., Li, M., & Xu, S. (2021). Experimental study on the three-dimensional wake structure of the drivaer standard model. *The Visualisation Society of Japan 2021*, *24*(443-460). https://doi.org/https://doi.org/10.1007/s12650-020-00714-2

Mahalingesh, N. (2020). *On-site drafting aerodynamics of cyclists using the ring of fire* (Master's thesis). Delft University of Technology. the Netherlands.

Mohebbian, A., & Rival, D. (2012). Assessment of the derivative-moment transformation method for unsteady-load estimation. *Experiments in Fluids*, *53*. https://doi.org/10.1007/s00348-012-1290-8

Passmore, M., & Good, G. M. L. (1994). A detailed drag study using the coastdown method. *SAE paper 940420*.

Passmore, M. A., Spencer, A., Wood, D., & Jowsey, L. (2010). The application of particle image velocimetry in automotive aerodynamics. *SAE Technical Paper 2010-01-0120*.

Prasad, A. (2000). Stereoscopic particle image velocimetry. *Experiments in Fluids*, *29*(103–116). https://doi.org/https://doi-org.tudelft.idm.oclc.org/10.1007/s003480000143

Raffel, M., Willert, C. E., Scarano, F., Kähler, C. J., Wereley, S. T., & Kompenhans, J. (2018). *Particle image velocimetry: A practical guide* (Third edition). Springer.

Rodriguez, R., Murzyn, F., Mehel, A., & Larrarte, F. (2017). Experimental study of the wake flow behind three road vehicle models. *23eme Congrès Français de Mécanique*, *Lille*(13 pages).

S.Becker, Lienhart, H., & Stoots, C. (2002). Flow and turbulence structures in the wake of a simplified car model (ahmed model). *Lehrstuhl für Strömungsmechanik (LSTM)*. https://doi.org/DOI: 10.1007/978-3-540-45466-3_39

Scarano, F. (2012). Tomographic piv: Principles and practice. *Measurement Science and Technology*, *24*, 012001. https://doi.org/10.1088/0957-0233/24/1/012001

Scarano, F., Ghaemi, S., Caridi, G. C. A., Bosbach, J., Dierksheide, U., & Sciacchitano, A. (2015). On the use of helium□filled soap bubbles for large□scale tomographic piv in wind tunnel experiments. *Experimental Fluids*, *6*(42). https://doi.org/DOI10.1007/s00348-015-1909-7

Sciacchitano, A., Caridi, G. C. A., & Scarano, F. (2015). A quantitative flow visualization technique for on-site sport aerodynamics optimization. *Procedia Engineering*, *112*(412–417). https://doi.org/doi: 10.1016/j.proeng.2015.07.217

Sciacchitano, A., Scarano, F., & Wieneke, B. (2012). Multi-frame pyramid correlation for time-resolved piv. *Experiments in Fluids*, *53*. https://doi.org/10.1007/s00348-012-1345-x

Sellappan, P., McNally, J., & Alvi, F. S. (2018). Time-averaged three-dimensional flow topology in the wake of a simplified car model using volumetric piv. *Experiments in fluids*, *59*(8). https://doi.org/DOI:10.1007/s00348-018-2581-5

Spoelstra, A. (2017). *Aerodynamics of transiting objects via large scale piv, the ring of fire concept* (Master's thesis). Delft University of Technology. the Netherlands.

Spoelstra, A., Hirsch, M., Sciacchitano, A., & Scarano, F. (2020). Uncertainty assessment of the ring of fire concept for on-site aerodynamic drag evaluation. *Measurement science and technology*, *32*(044004). https://doi.org/https://doi.org/10.1088/1361-6501/abb50d

Spoelstra, A., Norante, L., Terra, W., Sciacchitano, A., & Scarano, F. (2019). On-site cycling drag analysis with the ring of fire. *Experiments in Fluids*, *60*, 90. https://doi.org/10.1007/s00348-019-2737-y

Strachan, R. K., Knowles, K., & Lawson, N. J. (2004). A cfd and experimental study of an ahmed reference mode. *SAE technical paper series*, *01*(0442).

Strachan, R. K., Knowles, K., & Lawson, N. J. (2007). The vortex structure behind an ahmed reference model in the presence of a moving ground plane. *Experiments in fluids*, *42*(659–669). https://doi.org/DOI:10.1007/s00348-007-0270-x

Strangfeld, C., Wieser, D., Schmidt, H.-J., Woszidlo, R., Nayeri, C., & Paschereit, C. (2013). Experimental study of baseline flow characteristics for the realistic car model drivaer. *SAE Technical Paper 2013-01-1251*. https://doi.org/doi:10.4271/2013-01-1251

Terra, W., Sciacchitano, A., & Scarano, F. (2017). Aerodynamic drag of a transiting sphere by large-scale tomographic-piv. *Experimental Fluids*, *58*(83). https://doi.org/DOI10.1007/s00348-017-2331-0

Terra, W., Sciacchitano, A., Scarano, F., & Oudheusden, B. W. V. (2018). Drag resolution of a piv wake rake for transiting models. *Experimental Fluids*, *59*(120). https://doi.org/https://doi.org/10.1007/s00348-018-2570-8 van Oudheusden, B. W. (2013). PIV-based pressure measurement. *Measurement Science and Technology*, *24*(3), 032001. https://doi.org/10.1088/0957-0233/24/3/032001

Venning, J., Jacono, D. L., Burton, D., Thompson, M. C., & Sheridan, J. (2017). The nature of the vortical structures in the near wake of the ahmed body. *Journal of Automobile Engineering*, *231*(1239-1244). https://doi.org/https://doi.dox.org/10.1177/0954407017690683

Walston, W. H. J., Buckley, F. T., & Marks, C. (1976a). Analysis of coast-down data to assess the aerodynamic drag reduction on full-scale tractor-trailer trucks in windy environments. *SAE Transactions*, *85*(3).

Walston, W. H. J., Buckley, F. T., & Marks, C. (1976b). Test procedures for the evaluation of aerodynamic drag on full-scale vehicles in windy environments. *SAE Transactions*, *85*(1).

Walter, J. A., Pruess, D. J., & Romberg, G. F. (2001). Coastdown wind tunnel drag correlation and uncertainty analysis. *SAE Transactions*, *110*(6). https://doi.org/https://www.jstor.org/stable/44730921

Wang, S., Avadiar, T., Thompson, M. C., & Burton, D. (2019). Effect of moving ground on the aerodynamics of a generic automotive model: The drivaer-estate. *Journal of Wind Engineering and Industrial Aerodynamics*, *195*, 104000. https://doi.org/https://doi.org/10.1016/j.jweia.2019.104000

Wang, X. W., Zhou, Y., Pin, Y. F., & Chan, T. L. (2013). Turbulent near wake of an ahmed vehicle model. *Experimental Fluids*, *54*(1490). https://doi.org/DOI10.1007/s00348-013-1490-x

Westerweel, J. (1993). *Digital particle image velocimetry: Theory and application* (Doctoral dissertation). Delft University of Technology. the Netherlands.

Wieneke, B. (2005). Stereo-piv using self-calibration on particle images. *Experiments in Fluids*, *39*(267–280). https://doi.org/doi:10.1007/s00348-005-0962-z

Willert, C. (1997). Stereoscopic digital particle image velocimetry for application in wind tunnel flows. *Measurement Science and Technology*, *8*(1465-1479). https://doi.org/doi:10.1088/0957-0233/8/12/010

Wu, J.-Z., Pan, Z.-L., & Lu, X.-Y. (2005). Unsteady fluid-dynamic force solely in terms of control-surface integral. *Physics of Fluids - PHYS FLUIDS*, *17*. https://doi.org/10.1063/1.2055528

Appendix A

Run overview

A complete overview of the conducted runs during the measurement campaign is shown in this appendix. It should be noted that due to insufficient seeding in the measurement domain, most runs had to be excluded from the analysis, as explained in Chapter 5.

Date	Number of runs	Car	Good runs
01-09-2021	9	Up	0
02-09-2021	12	Up	0
03-09-2021	14	Up	11
07-09-2021	15	Up	0
08-09-2021	12	Tiguan radiator front open	0
09-09-2021	20	Tiguan radiator front open	0
13-09-2021	13	Tiguan radiator front open	5
14-09-2021	5	Tiguan radiator front open	5
	20	Tiguan radiator front closed	15
16-09-2021	13	Tiguan radiator front closed	13
20-09-2021	9	Tiguan radiator front closed	8
21-09-2021	10	Up	10

Appendix B

Anova function

For the statistical analysis in Chapter 6, the Matlab function Anova1 is used. This function determines whether the mean values of different groups of data are the same. One-way anova uses the simple version of the linear model, shown in Equation B.1:

$$y_{ij} = \alpha_j + \epsilon_{ij} \tag{B.1}$$

Where y is the observation, α is the mean of that observation and ϵ is the error, assumed to be independent and normally distributed. In this project, y_{i1} refers to the measurements of the Up and y_{i2} of the Tiguan. α_1 is the mean value of the Up measurements and α_2 is the mean value of the Tiguan measurements. ϵ_{i1} and ϵ_{i2} are the random errors for the Up and Tiguan, respectively. A matrix is constructed in Matlab where the columns represent the two configurations, and the rows the instantaneous drag values. It is therefore assumed that each value in the columns can be represented by a constant value α plus a random error ϵ. Anova provides a way in which it can be determine whether these constants are the same.